TRANSPARENCY, SECRECY, AND PROFILING USING MUTUAL SCATTERING IN COMPLEX MEDIA

ALFREDO RATES

TRANSPARENCY, SECRECY, AND PROFILING USING MUTUAL SCATTERING IN COMPLEX MEDIA

Alfredo Rates Soriano

TRANSPARENCY, SECRECY, AND PROFILING USING MUTUAL SCATTERING IN COMPLEX MEDIA

DISSERTATION

to obtain
the degree of doctor at the University of Twente,
on the authority of the rector magnificus,
prof.dr.ir. A. Veldkamp,
on account of the decision of the Doctorate Board,
to be publicly defended
on Tuesday the 10th of October 2023 at 14.45

by

Alfredo Rates Soriano

born on the 2nd of February 1995
in Santiago, Chile.

This dissertation has been approved by:

Promotors:
prof.dr. W.L. Vos
prof.dr. A. Lagendijk

Cover: Cover inspired by classic book covers. The symbols at the corners represent the random walk made by light in a scattering medium, while the square grids on the sides represent the segments of light modulation. On the back, three symbols appear representing the three projects of the thesis: mutual scattering to control transparency (top), physical unclonable functions (bottom left), and wavefront modulation to characterize objects (bottom right). Concept by Alfredo Rates and design by Paula García Miranda (pdgarciamiranda@gmail.com).
Printed by: Gildeprint, Enschede, The Netherlands
ISBN: 978-90-365-5849-5
ISBN: 978-90-365-5850-1 (digital)
DOI: 10.3990/1.9789036558501
This thesis is also available on http://www.nano-cops.com.

GRADUATION COMMITTEE:

Chair/Secretary	prof.dr. J.L. Herek (Universiteit Twente)
Promotors	prof.dr. W.L. Vos (Universiteit Twente)
	prof.dr. A. Lagendijk (Universiteit Twente)
Committee Members	prof.dr. M. Fink (ESPCI Paris) prof.dr. A.P. Mosk (Universiteit Utrecht) dr.ing. F. Zijp (ASML Veldhoven) prof.dr.ir. W.G. van der Wiel (Universiteit Twente) prof.dr.ir. I. M. Vellekoop (Universiteit Twente)

This work was financially supported by the NWO-TTW program "Free-form Scattering Optics", Project No. P15-36.

It was carried out at the
Complex Photonic Systems (COPS) chair,
Faculty of Science and Technology
and MESA+ Institute for Nanotechnology,
University of Twente, P.O. Box 217,
7500 AE Enschede, The Netherlands.

To my mother, who was always looking up to the stars,
and invited me to do the same.

Quien sabe, en una de esas... se escribe solo.

Contents

Chapter 1

Introduction

The research presented in this thesis aims to modulate the incident light into a scattering media to both control and study the light transport inside it inspired by questions from industry. In particular, we study a new phenomenon called mutual scattering, an interference process that modulates the extinction of light. Mutual scattering is always present when multiple light waves are incident into a finite scattering sample, but it was discovered only recently. Mutual scattering has potential applications in optical characterization, transparency modulation, and beyond. We commonly refer to mutual scattering as "wavefront shaping 2.0", as it is the next step in wavefront modulation. This thesis presents the first experimental observation of mutual scattering. In addition, we also use the wavefront shaping technique to study how the macroscopic shape of a sample affects light scattering inside it, since the device shape represents a new frontier in mesoscopic physics, inspired by industry. Furthermore, we propose an optical wireless communication based on speckle patterns to increase secrecy, and we test it using speckle correlation and unsupervised classification algorithms. In this introductory chapter, we present a motivation for the overall work of this thesis, a short theoretical framework, and an introduction to the novel concept of mutual scattering.

1.1 Why light scattering?

Light is an undoubtedly essential phenomenon from many points of view; it is a fundamental property of the universe, it is a crucial element for the existence of life and it is highly relevant in our current society for its perception and use[1]. Light has always captivated the curiosity of humanity and it has been the subject of extensive study throughout history, where many different approaches have been employed and new applications were discovered.

The applications of light can be observed on a daily basis (see Fig. 1.1). Starting with its role in illumination, ubiquitous worldwide, the advent of artificial illumination has had a revolutionary impact on humanity. Even prior to the invention of the light bulb, fire served as the primary means of artificial illumination. Throughout ancient times, firelight was not only used to see in dark spaces but also served purposes such as signaling and providing protection.

Nowadays, light serves as a tool for imaging our surrounding world at vastly different scales in the fields of microscopy and astronomy. Since the invention of the microscope by the Dutch physicist Antoni van Leeuwenhoek in the 17th century [1], the field of microscopy has relied heavily on the use of microscopes to visualize small objects, playing a significant role in our days in medicine and nanofabrication. On large scales, telescopes utilize light to capture images of large objects in the vast expanse of space [2]. Light also plays a crucial role in telecommunication, with optical fibers serving as the primary medium for long-distance digital data transport [3]. Expanding beyond the *optical* wavelength and considering the electromagnetic spectrum as a whole, we witness a more comprehensive range of applications that significantly influence our everyday lives [4]. Remarkably, such a small country like the Netherlands has amazingly large and influential high-tech industries (*e.g.*, ASML, Signify, Demcon, and Lumileds) that use advanced optics. The application questions have stimulated the research program "Free form scattering optics (FFSO)" that raised challenges and questions addressed in this thesis.

The study of light follows the same reasoning as other fields in physics. When studying any physical phenomenon, it is quite attractive to isolate this phenomenon and study it individually. The reductionist hypothesis — which states that all phenomena can be reduced and described by the same set of fundamental laws — is broadly accepted in physics. The reductionist approach is used, for example, in particle physics, where we try to understand the whole universe from its fundamental properties. This approach is often applied to the study of light as well. Nevertheless, we must always remember that each level of complexity brings entirely new properties. It is not recommended to describe highly complex systems using only "fundamental" laws. In turn, new, *emerging* laws appear. As P.W. Anderson writes, "We can see how the whole becomes not only more than but very **different** from the sum of its part" [5]. The study of light is no exception to this. The emerging physics of light interacting and traveling through complex media, composed of many microscopic inhomogeneities, is described by

[1] The ability to perceive light is almost taken for granted in our daily lives, which consequently makes it increasingly challenging for those who lack it.

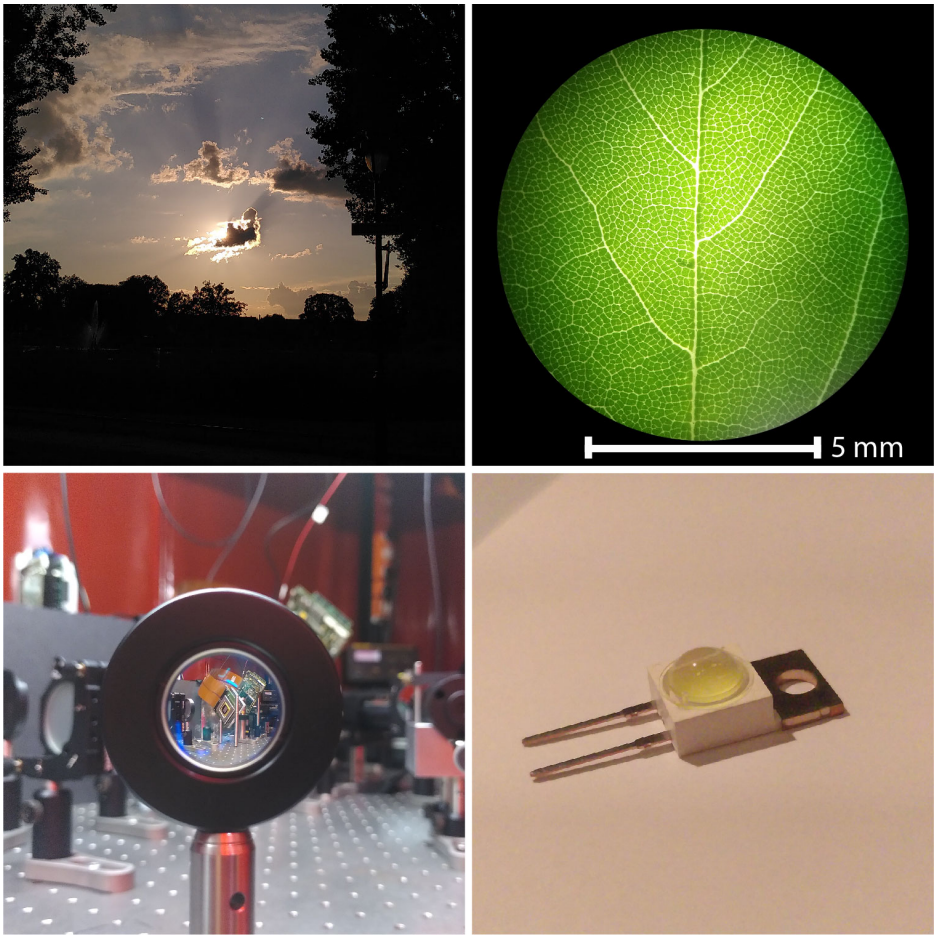

Figure 1.1: Photograph showing examples of light interacting with our surroundings. The top left picture shows the light scattered by clouds in the sky. The top right shows an optical microscope picture of a leaf. The bottom left shows the focusing effect of a lens. Finally, the bottom right shows an LED, in which we identify the phosphor as the yellowish blob on top of the chip, which scatters the emitted light for an even illumination.

emerging physical laws, which are much closer to our macroscopic view of the world, and thus closer to many impactful applications.

An important phenomenon that emerges while studying light — and particularly crucial for the content of this thesis — is **interference**. When two waves of any kind combine, they interfere, forming a combined wave with either a smaller or larger amplitude. The amplitude of the resulting wave depends on the relative *phase* between the two initial waves. If the two waves are in phase (the crests and troughs of both waves match in space and time), they interfere *constructively*, generating a wave with a larger amplitude. Conversely, if the waves are out of phase (the crests of one wave are aligned with the troughs of the other), they interfere *destructively*, generating a wave with a smaller amplitude, or even causing the amplitude to become zero, thus annihilating both waves.

A famous experiment that involves light interference is **Young's double-slit experiment**. This experiment simply consists of directing a light wave onto a screen with only two closely spaced slits, and a final measurement plane further away (see Fig. 1.2). Since light behaves as a wave, two *spherical* waves are generated from the slits that act as two secondary sources. When we observe the measurement plane, we see *fringes* of intensity, *i.e.*, bright and dark lines. The bright lines are formed when the two spherical waves constructively interfere, while the dark lines are formed when the two spherical waves destructively interfere. In this experiment, the two waves are either in phase or out of phase, depending on the distance between the slits and the measurement plane. We can draw a parallel between the double-slit experiment and our mutual scattering experiments in Fig. 1.2, with the addition that between the sources and the measurement plane, we place a finite object and measure the interferences formed by the waves transmitted through the object. However, we do not measure just any type of object; our focus lies on *complex media*.

Complex media are composed of many microscopic homogeneities, called *scatterers*. When light travels through complex media, it gets *scattered*; by interacting with the scatterers, the light takes many different paths, which create interferences. When the light is reflected from or transmitted through the medium and imaged on a screen, the interferences generate a random intensity pattern called the speckle pattern, and the initial information of the wavefront gets scrambled. Light scattering is observed on a daily basis, and it is the reason why we see vaguely or not at all through a foggy window.

Historically, light scattering has been considered noise or aberration, and it is therefore typically minimized [6, 7]. However, in recent times, light scattering has gained significance as an effective means to investigate and manipulate light within complex media [8, 9]. Although the information is scrambled, it is certainly not destroyed, and by studying the random interferences that result in the speckle pattern, we understand how light interacts with the media. When we understand light scattering we access more — and *different* — information that is not accessible in a scatter-less system.

In this thesis, we study light scattering using modulation techniques. The principal result of this thesis is the measurement, understanding, and use of the **mutual scattering effect**. Mutual scattering is a recently-discovered effect

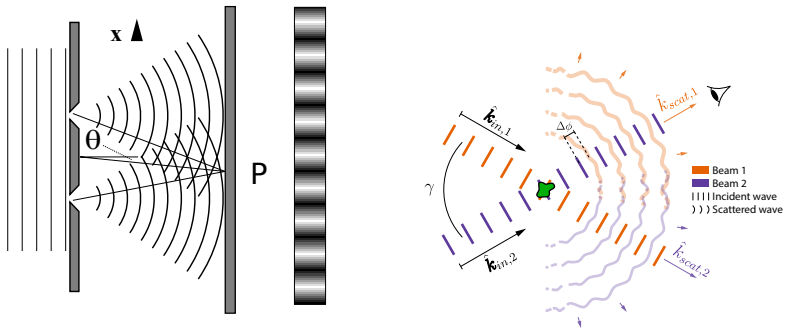

Figure 1.2: Schematic of Young's double-slit and mutual scattering experiments. In the double-slit experiment (left), a wave is incident into a plane with two slits and we measure the interferences at the detector plane. In the mutual scattering experiments (right), two incident waves cross in a complex object and we measure the interferences formed by the waves in transmission. The diagram for the double-slit experiment was retrieved from wikipedia.org on July 2023, credits to Francesco Franco, CC BY-SA 3.0 `https://creativecommons.org/licenses/by-sa/3.0`, via Wikimedia Commons.

that is present in *any* finite-size material when illuminated by more than one light wave. Mutual scattering is an interference phenomenon that modulates the transparency of the object, and the amplitude of the modulation is not minor: it goes from making the material *fully transparent* to *twice as opaque*.

1.2 General concepts

1.2.1 Relevant length scales

Light scattering has been studied for many years in the group of Complex Photonic Systems (COPS) [10]. In the present section, we give a short theoretical framework for the topics covered by this thesis and we refer the readers to previous COPS Ph.D. theses where these concepts are described in depth, and where this section is based on [11–18].

When light passes through an object, the interaction between light and the object depends on the optical properties of the object. The object can be absorbing and thus transform the electromagnetic energy of the light into other types of energy or can be scattered and thus refract, reflect, or disperse the incident light. When the light is transmitted through the object, any diminishment of the energy of the light with respect to the initial energy is called *extinction*[2]. Light extinction can be due to absorption, scattering, or both.

A complex material is composed of inhomogeneities — or *scatterers* — which interact with light in various ways. *Single scattering* is the phenomenon when one scattering event occurs with one scatterer[3], whereas *multiple scattering* is

[2]We do not consider non-linearities in this description and this thesis in general.
[3]All possible multiple interactions with one scatterer are described by the complete t-matrix,

when the light interacts multiple times, suffering many changes in its direction inside the material [20–24]. We define the *scattering mean free path* ℓ_{sc} as the average distance between scattering events within a complex material. Thus, for multiple scattering to occur, the material must have a thickness L larger than the scattering mean free path $L > \ell_{\text{sc}}$. The material can also absorb light. To describe absorption, we define the *absorption mean free path* ℓ_{abs} as the average distance light travels to have a decay to $1/e$. As mentioned, light extinction is a combination of scattering and absorption. Hence, we define the *extinction mean free path* ℓ_{ext} as a combination of the scattering and absorption mean free path, namely,

$$\ell_{\text{ext}} \equiv \left(\frac{1}{\ell_{\text{scat}}} + \frac{1}{\ell_{\text{abs}}} \right)^{-1}. \tag{1.1}$$

After many scattering events, the incident light gets *scrambled* inside the material. In particular, the information on the incident direction is lost. We define the *transport mean free path* ℓ_{tr} as the average distance when this happens. If the object has a thickness larger than the transport mean free path $L > \ell_{\text{tr}}$, then the object is *opaque*.

The only macroscopic characteristic we have discussed so far is the thickness of the object. This has an implicit assumption about the *shape* of the object because historically the shape considered is almost always a **slab**: a perfectly flat and infinitely wide object with finite thickness. The thickness of an object loses relevance when the object is free-form or finite, which is the common case for industrial applications. A surface is considered to be free-form when it has no axis of rotational invariance [25]. Over the last decade, free-form optics have been used in the development of versatile, miniature, and efficient devices that appear in daily life [26, 27].

1.2.2 Transmission matrix in light scattering

The interferences present in light scattering combine linearly in the fields. As such, it is possible to describe it with linear equations. In particular, it is possible to describe the transmission of light through any scattering object with a transmission matrix $\boldsymbol{T}$, which relates the incoming and outgoing electromagnetic fields [28–30],

$$\vec{E}_{\text{out}} = \boldsymbol{T}\vec{E}_{\text{in}}, \tag{1.2}$$

were $\vec{E}_{\text{in}}$ and $\vec{E}_{\text{out}}$ are the incoming and outgoing electromagnetic fields, respectively. We assume that the complexity of the object is so large that it can be described with random matrix theory (RMT) [31–33]. To get more information about the sample, we decompose $\boldsymbol{T}$ using singular value decomposition (SVD) [14, 15], as

$$\boldsymbol{T} = \boldsymbol{U}\boldsymbol{\Sigma}\boldsymbol{V}, \tag{1.3}$$

see [19, 20]

were $\boldsymbol{U}$ and $\boldsymbol{V}$ are random unitary matrices and $\boldsymbol{\Sigma}$ a diagonal matrix. From Eq. 1.3, we relate the elements of $\boldsymbol{\Sigma}$ to the eigenmodes of the sample, *i.e.*, the *transmission channels*. $\boldsymbol{U}$ and $\boldsymbol{V}$ are interpreted as *mapping* matrices. $\boldsymbol{U}$ represents the mapping between the incident modes (in our case, free-space plane waves) and the transmission channels, while $\boldsymbol{V}$ represents the mapping between the transmission channels and the outgoing modes (typically again modes in free-space). The concepts of transmission channels, incident mode, and outgoing mode are abstract, and depending on the physical system, they refer to waveguide modes, plane waves, or spatial position. However, because of the RMT description, the statistical properties of the mapping matrices $\boldsymbol{U}$ and $\boldsymbol{V}$ are invariant to any unitary transformation. Changing the definition of the channel (*e.g.*, from waveguide mode to position on the sample surface) means applying a unitary transformation to the mapping matrices $\boldsymbol{U}$ and $\boldsymbol{V}$. Because $\boldsymbol{U}$ and $\boldsymbol{V}$ are invariant to such transformation, their ensembled properties are independent of the physical definition of a channel [14].

The open and closed channels are a fascinating discovery of the transmission matrix approach. One would expect that if a scattering object is composed of many transmission channels, light transmission is evenly spread across the different transmission channels, but this is not the case. Instead, most transmission channels have a near 0 transmission, while just a few channels have nearly full transmission [34–37]. We call the first type of channel the closed channels and the second type the open channels. Even more, as most of the transmitted light is through a few transmission channels, there is a reduction of the degrees of freedom of the system, which gives rise to *correlations* between the different transmission channels [20, 38]. One of the consequences of these correlations is the *memory effect*. When light is transmitted or reflected in a scattering media, it generates a speckle pattern. If the properties of the incident light are changed within a certain range, called *memory range*, the speckle pattern is still nearly the same. The memory effect has been studied by changing the angle of the incident beam, its position on the sample, and its wavelength [39–42].

1.2.3 Wavefront shaping

Because light scattering is a linear process, it is also deterministic: if a scattering sample is static (*i.e.*, its transmission matrix is invariant of time), then it is in principle possible to predict the resulting pattern for any incident wavefront. This holds for any scattering sample, even highly opaque ones such as a piece of paper or a layer of paint. If it is theoretically possible to predict the resulting wavefront, is it possible then to *control* it?

The wavefront shaping (WFS) technique invented by Vellekoop and Mosk at COPS is based on precisely this concept: to optimize the transmission of light through a scattering sample to generate a target wavefront [43, 44] (See Fig. 1.3). For that, we modulate the incident wavefront by spatially dividing it into *segments*. These segments are considered to be our incident modes. Thus, if we set a *target transmitted wavefront*, we can adjust the incident modes by changing their amplitude and phase such that the transmitted wavefront is similar to the

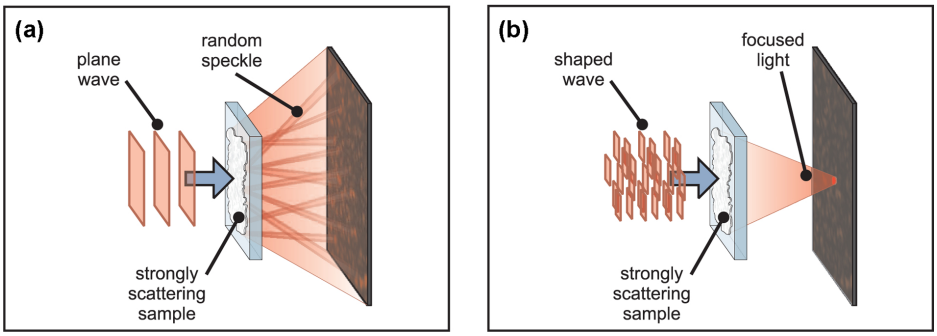

Figure 1.3: Cartoon illustrating the working principle of wavefront shaping. (a) At the left, A plane wave is incident into a scattering sample. The light couples to many transmission channels, interfering with each other, resulting in a random speckle pattern in transmission. (b) At the right, a shaped wave is incident into the sample. The shape of the wave matches the transmission channels resulting in the target wavefront, where all the transmitted light is concentrated in a focusing spot. Reprinted with permission from [43] ©The Optical Society.

target one after being multiplied by the transmission matrix.

One of the early experiments with WFS was to turn any scattering sample into a lens. In this case, the *target transmitted wavefront* has a delta function where we concentrate all the intensity into one spot, *i.e.*, we focus the light. To obtain the highest transmission, WFS aims to couple all the light into the open channels of the sample [45]. An essential concept for this application is the enhancement of intensity η, representing the increase in intensity at the target spot after optimization, and defined as

$$\eta \equiv \frac{I_{\text{opt}}}{\langle I_0 \rangle}, \tag{1.4}$$

where I_{opt} is the intensity at the target position after wavefront optimization and $\langle I_0 \rangle$ is the ensemble average intensity at the target position before optimization [46]. The intensity enhancement has a theoretical limit strictly related to the number of degrees of freedom of the system. For a case of phase-only wavefront modulation — which is the case we are concerned with — this limit is given by

$$\eta_0 = \frac{\pi}{4}(N_{\text{s}} - 1) + 1, \tag{1.5}$$

where N_{s} is the total number of segments in the modulated wavefront. This limit suggests that if we keep increasing the number of segments, it is possible to reach infinite enhancement. In reality, this is not the case. The maximum enhancement is limited by the number of transmission channels of the sample, and the trend of intensity enhancement saturates once the number of segments reaches the number of channels of the sample.

To implement the wavefront shaping technique, we need a closed loop, since wavefront shaping is in simple terms a "question-and-answer" game. That is, we

need to adjust the input to the system with the information from the output of the system. In this case, the input is the phase of each segment, and the output is the intensity at the target spot or the transmitted wavefront for the general case. Because it is a linear system, the optimization process does not affect the final result as long as the sample is stationary. The simplest optimization method is called the *sequential method*, where we vary the phase of each segment from 0 to 2π and select the phase that maximizes the intensity. Then, we move to the next segment and repeat the same procedure for each segment. An attractive application of WFS is in biological imaging, a field in which the samples are far from static. For those applications, improvement in the optimization speed is highly desired. Therefore, various new optimization methods have been proposed, such as genetic algorithms [47, 48] or machine learning-based algorithms [49, 50].

1.3 The impact of light scattering in industry

The applications of light in our daily lives are not only designed and considered in fundamental research. Plenty of new insights and designs that directly affect applications come from the industry. Industrial applications range from illumination to microscopy, from telecommunications to nanofabrication.

In many industrial applications, light scattering is unavoidable. In some applications, such as metrology, light scattering is minimized, while other applications, such as illumination, consider light scattering as part of the design. Understanding the fundamental physics that rules the system at hand is crucial to optimizing light scattering correctly. However, many applications pertain to what we refer to as the *industrial regime* of light scattering [18]. In the industrial regime, the thickness of the designed sample L is on the order of the transport mean free path $L \approx \ell_{\mathrm{tr}}$. This regime is an intermediate between the *thin* and the *thick* limits. In the thin limit, the thickness is much smaller than the transport mean free path $\mathrm{L} \ll \ell_{\mathrm{tr}}$. If the thickness is much larger than the wavelength $\mathrm{L} \gg \lambda$, geometrical optics accurately describes the behavior of light through the sample. If, instead, the thickness has a comparable magnitude to the wavelength, then the light is weakly scattered and light transport is well described by the first-order Born approximation [51, 52].

Conversely, in the thick limit, the thickness is much larger than the transport mean free path $\mathrm{L} \gg \ell_{\mathrm{tr}}$ and smaller than the absorption mean free path $\mathrm{L} \ll \ell_{\mathrm{abs}}$. In this limit, the sample is opaque and typically appears white (like foal, paint, or biological tissue). If the interference is negligible, the transport is well described by radiative transfer [53]. When interferences are relevant, one takes recourse to the advanced methods from mesoscopic physics such as random matrix theory [20].

Because the industrial regime is in between the two described limits, neither of the approaches is enough to fully describe the light scattering in the sample. The lack of fundamental descriptions in current industrial applications has led to designs based on educated guesses, which limits progress and applications.

The limitations of current approaches in the industrial regime are even more prominent when the sample is *free form*, *i.e.*, the shape of the sample is not a

simple geometrical shape such as a sphere, cylinder, or slab, or its surfaces are not perfectly flat [54]. It is currently not feasible to describe light scattering in applications such as coatings, diffusers, or suspensions with free-form optics. The presence of microscopically structured materials in macroscopic free forms implies a vast difference in scale to which conventional geometrical optical models cannot be applied [26, 55]. Hence, current industry solutions invoke shortcuts, including untested assumptions. Today's lack of knowledge on free-shape scattering optics hampers fast, efficient, and systematic design progress as well as the development of new optical architectures [56].

When the light source is temporally coherent, the light transport inside a scattering sample is ruled by interference [19, 57]. Because of light interference, the *phase information* is crucial in the industrial regime, and approaches such as geometrical optics or diffusion disregard this information. A clear example of the impact of light interference is the speckle pattern, a random pattern generated by the interference of multiple scattered light waves with different phases and directions. A speckle pattern is visible to the naked eye as the grainy pattern when shining a laser beam on a wall. In industrial environments particularly for illumination distribution, speckle is usually considered a nuisance, since speckle spots correspond to light beams that emanate in random directions from the medium. Hence speckle spoils a homogeneous illumination intensity desired for specific applications. Speckle is also considered a nuisance when it precludes standard imaging methods, thus making it hard or impossible to view metrology markers hidden on a wafer.

A speckle that is well known in the industry is **surface speckle**. This speckle is commonly seen with glass diffusers, and it is described as adding a random phase mask to the wavefront. Nevertheless, this is not the type of speckle commonly studied in light scattering experiments, as a surface scattering sample *has no mean free path*. In turn, the most common speckle is **volume speckle**. This is the speckle formed by paint, paper, foam, or biological tissue, and it is described using random matrix theory (RMT) [31–33]. Volume speckle differs from surface speckle because it has intricate correlations, famously known as C_0, C_1, C_2, and C_3 correlations [20, 58, 59].

Light modulation has proven to be an effective way to control both surface and volume speckle, and light scattering in general. Techniques such as wavefront shaping are based on optimizing the interference of scattered waves to engineer a desired speckle pattern. One can also exploit known speckle properties to devise algorithms that correct for speckle, or that put speckle to favorable use. Furthermore, speckle reveals complex properties of the scattering sample, such as the distribution of scatterers inside the sample, the scatterers structure's dimension, the roughness of the surface, or even the dynamics of the scatterers inside the sample [60]. Beyond speckle, an attractive application of light modulation is on diffused light to have a directional illumination with a diffused light source. Modulating light is, as we described, a promising approach to controlling and studying light in the industrial regime.

1.4 Mutual scattering

1.4.1 Brief history of mutual scattering

The wavefront shaping (WFS) technique — described earlier in this chapter — was presented to the scientific community in 2007 by Vellekoop and Mosk [43] at the Complex Photonic Systems (COPS) chair. Ever since, WFS has been used worldwide as a well-known technique for studying light transport through scattering media [61, 62], for high-resolution imaging [63–65], and for data scrambling and retrieving [66, 67]. In particular, WFS is a popular technique used at COPS, with many results related to this technique, both in theory and experiment.

The current theory for WFS relies on approximating the scattering media by waveguides, to invoke random matrix theory as a description [28, 68]. This technique has yielded exciting results and predictions but is far from complete. In the late 2010s, Lagendijk *et al.* attempted to describe WFS from exact calculations. For this, they described the focusing incident beam into the sample as multiple incident plane waves with a range of incident angles, and they described the sample as a set of single scatterers. Lagendijk *et al.* used the *optical theorem* to check the energy balance of the calculation. The original optical theorem states that in a system without absorption (elastic scattering), the power S_{ext} subtracted from the incident wave due to the sample — *i.e.*, the light extinction — has to be equal to the power S_{scat} of all scattered waves integrated over solid angle Ω, namely

$$S_{\text{ext}} = S_{\text{scat}}, \tag{1.6}$$

$$4\pi\omega \,\mathrm{Im} f(\frac{\omega}{c}\hat{k}_{\text{in}}, \frac{\omega}{c}\hat{k}_{\text{in}}) = \frac{\omega^2}{c}\int_{\Omega} \mathrm{d}\hat{k}_{\text{out}} |f(\frac{\omega}{c}\hat{k}_{\text{out}}, \frac{\omega}{c}\hat{k}_{\text{in}})|^2, \tag{1.7}$$

where ω/c is the magnitude of the wavevector, and $f(\frac{\omega}{c}\hat{k}_{\text{out}}, \frac{\omega}{c}\hat{k}_{\text{in}})$ the scattering amplitude. The scattering amplitude denotes the scattering strength from incoming direction $\hat{k}_{\text{in}}$ to outgoing direction $\hat{k}_{\text{out}}$.

Surprisingly, when applying the optical theorem for each incident wave, Lagendijk *et al.* found that the original optical theorem yields a **violation of the energy conservation**. Puzzled by this result, they investigated further and realized that the original optical theorem does not hold for multiple incident waves, as these waves will interfere with each other, modulating the light extinction of the system. What makes this effect interesting for applications is that, by modulating the total light extinction of the system, it is possible to make the sample more opaque (increase extinction) or more transparent (reduce extinction, see Fig. 1.4), and it is present for both scattering and absorbing materials. Lagendijk *et al.* published in 2020 these findings with an extended optical theorem and called this extinction modulation the mutual extinction and transparency effect [69]. The name of the effect was later changed to **mutual scattering**.

In 2021, Rates *et al.* made the first experimental observation of the mutual scattering effect on a silicon bar and a human hair using two incident waves [70]. This is described in Chapter 3. Ever since, mutual scattering has been of great

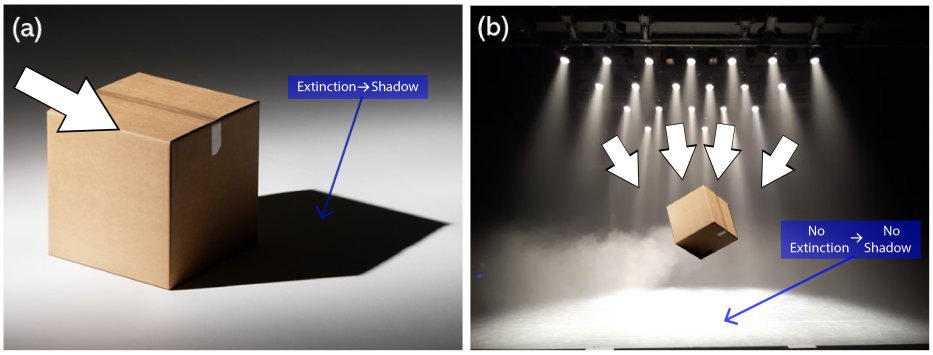

Figure 1.4: Cartoon illustrating the principle of light extinction modulation. (a) If one incident wave (white arrow) is present in the sample, it generates a *shadow*. This shadow is related to the light extinction in the system. (b) Mutual scattering modulates the extinction by using multiple incident waves (multiple white arrows). We effectively control the object's shadow when increasing or decreasing the extinction.

interest to COPS. Truong *et al.* showed in 2022 how mutual scattering is capable of sensing the position of a single scatterer inside an object filled with identical scatterers [71], and Rates studied how mutual scattering may be used to characterize any object (Chapter 4) and compared how optimizing light extinction using mutual scattering differs from optimizing intensity using wavefront shaping (Chapter 5).

It is believed that mutual scattering has a wide range of applications, both to control and study light scattering and absorption in complex media. Furthermore, mutual scattering is regarded as the evolutionary progression of wavefront shaping and we therefore colloquially refer to it as "WFS 2.0". As we show in this thesis, by measuring light extinction we get more information than just measuring intensity, and light extinction optimization also offers more control than intensity-only modulation.

1.4.2 Light extinction of a single wave

When an incident light wave ψ_{in} with direction $\hat{k}_{\text{in}}$ passes through a scattering object[4], the wave ψ is partitioned into two waves, an unperturbed part (the incident part ψ_{in}) and a perturbed part (the scattered part ψ_{scat})[19],

$$\psi = \psi_{\text{in}} + \psi_{\text{scat}}. \tag{1.8}$$

The incident part has the same properties (*i.e.*, a plane wave) as if the wave never encountered the scattering object. In contrast, the scattered part is a spherical wave, and its amplitude depends on the scattering properties of the object ruled by the *scattering amplitude* $f(\frac{\omega}{c}\hat{k}_{\text{out}}, \frac{\omega}{c}\hat{k}_{\text{in}})$. In the far field, we express both

[4]We will limit ourselves to scalar and plane waves for didactic simplicity. For full vector EM waves, see, *e.g.* Refs. [72, 73].

waves as

$$\psi_{\text{in}} = A \exp\left(i\hat{k}_{\text{in}} \cdot \mathbf{r} - i\omega t + i\phi\right), \tag{1.9}$$

$$\psi_{\text{scat}} = \frac{A}{r} f\left(\frac{\omega}{c}\mathbf{r}, \frac{\omega}{c}\hat{k}_{\text{in}}\right) \exp\left(i\frac{\omega}{c}r - i\omega t + i\phi\right), \tag{1.10}$$

where $r = |\mathbf{r}|$ is the distance from the scattering object, t is time, and A and ϕ are the amplitude and phase of the incident wave, respectively.

The scattering amplitude f is a function intrinsic to the scattering object. Similar to a transmission matrix, the scattering amplitude gives the relation between an incoming wave at any incoming angle and a scattered wave at any outgoing angle. This function encapsulates both the scattering and absorption properties of the object.

When we place a detector in the far field, we measure the current J of the waves, expressed as

$$J = \text{Re}\left[(\partial_t \psi)^* \boldsymbol{\nabla} \psi\right], \tag{1.11}$$

where the asterisk * denotes a complex conjugate. To simplify the notation of the following derivation, we define the operators $\star$ and $\star\star$ as

$$x \star y \equiv \text{Re}\left[(\partial_t x)^* \boldsymbol{\nabla} y\right], \tag{1.12}$$

$$x \star\star y \equiv x \star y + y \star x. \tag{1.13}$$

We interpret the operation $x \star y$ as the interference of the waves at the detector. As we have two waves, ψ_{in} and ψ_{scat}, the current J is expressed as

$$J = \psi_{\text{in}} \star \psi_{\text{in}} + \psi_{\text{scat}} \star \psi_{\text{scat}} + \psi_{\text{in}} \star\star \psi_{\text{scat}}, \tag{1.14}$$

where the first term is the detected current due to the incident wave, the second term is the current due to the scattering wave, and the third term is an interference between the incident wave and the scattered wave.

The third term of Eq. 1.14 is called the *extinction* term. Light extinction is any diminishment of the incident light, either because of absorption or scattering. In the absence of gain, this third component naturally has the opposite sign of the other two components, balancing energy conservation.

1.4.3 Light extinction of two waves

If we have multiple N incident light waves, the system gets more complicated. In the case of $N = 2$ incident waves illustrated in Fig. 1.5, each wave is partitioned into two waves, leading to a total of 4 waves,

$$\psi = \psi_{\text{in},1} + \psi_{\text{in},2} + \psi_{\text{scat},1} + \psi_{\text{scat},2}. \tag{1.15}$$

Now when measuring the current J, we have a total of 10 terms,

$$\begin{aligned} J = {} & \psi_{\text{in},1} \star \psi_{\text{in},1} + \psi_{\text{scat},1} \star \psi_{\text{scat},1} + \psi_{\text{in},1} \star\star \psi_{\text{scat},1} \\ & + \psi_{\text{in},2} \star \psi_{\text{in},2} + \psi_{\text{scat},2} \star \psi_{\text{scat},2} + \psi_{\text{in},2} \star\star \psi_{\text{scat},2} \\ & + \psi_{\text{in},1} \star\star \psi_{\text{in},2} + \psi_{\text{scat},1} \star\star \psi_{\text{scat},2} \\ & + \psi_{\text{in},1} \star\star \psi_{\text{scat},2} + \psi_{\text{in},2} \star\star \psi_{\text{scat},1} \end{aligned} \tag{1.16}$$

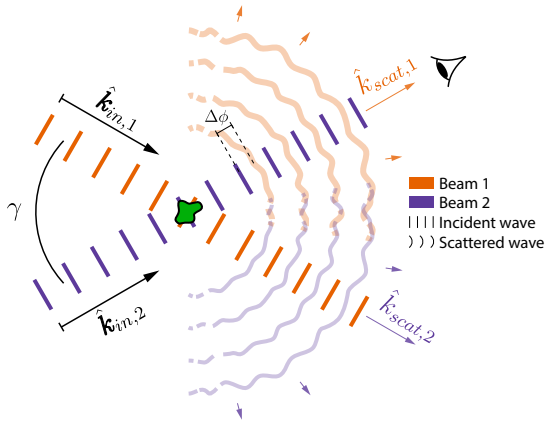

Figure 1.5: Schematic of two-wave mutual scattering: $N = 2$ beams with wavevectors $\hat{k}_{\mathrm{in},1}$ and $\hat{k}_{\mathrm{in},2}$ and mutual angle γ are incident onto a scattering sample. The scattered waves are shown as curved wobbly wavefronts to emphasize that they are present at all outgoing directions (with wavevectors $\hat{k}_{\mathrm{scat},1}$ and $\hat{k}_{\mathrm{scat},2}$). When $\hat{k}_{\mathrm{scat},1} = \hat{k}_{\mathrm{in},2}$ and $\hat{k}_{\mathrm{scat},2} = \hat{k}_{\mathrm{in},1}$, the scattered wave interfere with the incoming coherent beam. $\Delta\phi$ refers to the phase difference between two incoming waves. The arrow colors distinguish the scattered waves and do not represent different wavelengths. This figure is also shown in Chapter 4.

In Eq. 1.16, we recognize the same terms as in Eq. 1.14 for both incident waves. Besides the first six known individual terms concerning each wave, there are also *cross terms*. The 7^{th} term shows the interference between the two incident waves, the 8^{th} term shows the interference between the two scattered waves, and the 9^{th} and 10^{th} terms show a cross-interference between the incident part of one wave and the scattered part of the other. These last cross-interferences have the same description as the light extinction of a single wave. Furthermore, the cross-extinction term adds to the original extinction either constructively or destructively, effectively modulating the light extinction. This is the essence of *mutual scattering*; modulation of the light extinction in a multi-beam system.

Specifically, the current component of the mutual scattering is equal to

$$\begin{aligned} J_{\mathrm{MS}} = &- \frac{2\omega}{r^2} A_1 A_2 \mathrm{Im}\left(f(\frac{\omega}{c}\hat{k}_{\mathrm{in},2}, \frac{\omega}{c}\hat{k}_{\mathrm{in},1}) e^{i(\phi_2 - \phi_1)} \right) \delta\left\{ 1 - \cos\left(\mathbf{r}, \hat{k}_{\mathrm{in},1}\right) \right\} \\ &- \frac{2\omega}{r^2} A_1 A_2 \mathrm{Im}\left(f(\frac{\omega}{c}\hat{k}_{\mathrm{in},1}, \frac{\omega}{c}\hat{k}_{\mathrm{in},2}) e^{i(\phi_1 - \phi_2)} \right) \delta\left\{ 1 - \cos\left(\mathbf{r}, \hat{k}_{\mathrm{in},2}\right) \right\}, \end{aligned} \quad (1.17)$$

where A_1, A_2 and ϕ_1, ϕ_2 are the amplitudes and phases of waves ψ_1 and ψ_2, respectively. Since $\delta\{\}$ is the Dirac delta function, it is apparent that the extinction component is only present in the direction of the incident waves. From Eq. 1.17, we see that by adjusting the phase ϕ_1, ϕ_2 of the incident waves and their relative angle — expressed as the difference between $\hat{k}_{\mathrm{in},1}$ and $\hat{k}_{\mathrm{in},2}$ — we are able to control the light extinction.

1.4.4 Mutual scattering as wavefront shaping 2.0

This section is focused on an experiment with two incident beams, which is similar to a WFS experiment using only 2 segments (we extend this to N beams in Chapter 5). With this, we are already able to draw some comparisons between mutual scattering and WFS. We illustrate the basic comparison between mutual scattering and WFS in Fig. 1.6.

In WFS, the sample is usually assumed to be an opaque slab on a waveguide. This means that when measuring in transmission, *the incoming wave is not present* and it is not possible to measure light extinction as described here. Looking at Eq. 1.16, while mutual scattering focuses on the 9^{th} and 10^{th} terms, WFS focuses on the 2^{nd}, 5^{th}, and 7^{th} terms, which only include the scattered waves. These are not extracted from the measurements, but they are assumed to be the only ones in the system. When WFS is applied to a finite or non-opaque sample, the incoming wave is present, and not only the scattered terms are optimized but all terms are considered together[5]. Specifically, the current component of the scattered waves is equal to

$$\begin{aligned} J_{\text{Scat}} =& \frac{2\omega^2}{r^2 c} A_1^2 |f(\frac{\omega}{c}\mathbf{r}, \frac{\omega}{c}\hat{k}_{\text{in},1})| + \frac{2\omega^2}{r^2 c} A_2^2 |f(\frac{\omega}{c}\mathbf{r}, \frac{\omega}{c}\hat{k}_{\text{in},2})| \\ &+ \frac{2\omega^2}{r^2 c} A_1 A_2 \text{Re}\left(f(\frac{\omega}{c}\mathbf{r}, \frac{\omega}{c}\hat{k}_{\text{in},1}) f^*(\frac{\omega}{c}\mathbf{r}, \frac{\omega}{c}\hat{k}_{\text{in},2}) e^{i(\phi_1 - \phi_2)} \right), \end{aligned} \tag{1.18}$$

were c is the speed of light and $\mathbf{r}$ is the direction of the measurement. The third term of Eq. 1.18 is similar to Eq. 1.16. Nevertheless, the values of the scattering amplitude in both directions are coupled and the extraction is not as straightforward. If we increase the number of segments to N, all the N values of the scattering amplitude in all the directions will be intertwined in the same term. The scattered power spreads to all the outgoing angles, and compared to J_{MS}, J_{Scat} has an extra ω/c component, which makes its signal to have a much smaller amplitude in a particular direction.

WFS relies on having scattered light. But in a fully absorbing sample, no light is scattered, and thus nothing is measured and WFS is not applicable, while mutual scattering is still valid. Considering all this, we observe that measuring light extinction is more versatile, gives more information, and is more sensitive than measuring light intensity. It is for these reasons that we see mutual scattering as the natural progression of WFS, and we thus refer to it as WFS 2.0.

1.4.5 Measurement procedure

As shown in the previous section, the mutual scattering current (Eq. 1.17) is only a part of the total current measured by a simple detector. In order to extract the mutual scattering component from measurements of the current J, we need to devise a measurement procedure with ancillary measurements, which

[5] We show in Chapter 5 how using WFS with a fine sample optimized mainly the incoming waves rather than the scattered waves.

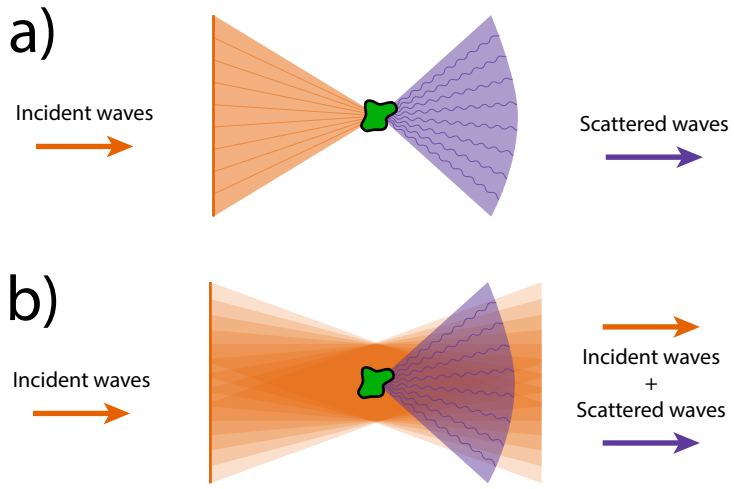

Figure 1.6: Illustration showcasing the difference between wavefront shaping and mutual scattering. (a) In wavefront shaping, the light is focused on the opaque object, which is much larger than the focus point. Thus, in transmission only the scattered waves are present. (b) In mutual scattering, the incident beams cross in the opaque object with a beam waist larger than the size of the object. Thus, both the scattered waves and the incident waves are present in transmission.

we describe in the present section. To relate the measurement procedure with equation Eq. 1.16, we re-write it on Eq. 1.19 with highlighting boxes[6]:

$$
\begin{aligned}
J = &\psi_{\text{in},1} \star \psi_{\text{in},1} + \psi_{\text{scat},1} \star \psi_{\text{scat},1} + \psi_{\text{in},1} \star\star \psi_{\text{scat},1} \\
&+\psi_{\text{in},2} \star \psi_{\text{in},2} + \psi_{\text{scat},2} \star \psi_{\text{scat},2} + \psi_{\text{in},2} \star\star \psi_{\text{scat},2} \\
&+\psi_{\text{in},1} \star\star \psi_{\text{in},2} + \psi_{\text{scat},1} \star\star \psi_{\text{scat},2} \\
&+\psi_{\text{in},1} \star\star \psi_{\text{scat},2} + \psi_{\text{in},2} \star\star \psi_{\text{scat},1}
\end{aligned}
\tag{1.19}
$$

As detailed before, components 1, 2, and 3 are also present when only wave ψ_1 is incident in the sample, while components 4, 5, and 6 are also present when only wave ψ_2 is incident in the sample. Thus, by measuring those two cases (only ψ_1 incident in the sample and then only ψ_2 incident in the sample), we can subtract the first six components. This is highlighted with the green (1^{st} line) and red (2^{nd} line) boxes, respectively. To isolate the 7^{th} component of Eq. 1.19, we note that if we move the sample, there are no scattered waves, and thus only components 1, 4, and 7 are present. This is highlighted with the gray vertical box. If we also subtract this measurement (both waves present but no sample), we subtract the 1^{st} and 4^{th} components twice. To add them back, we notice that only the incident part is present by measuring a single wave without the sample. Thus, we add those two measurements (only wave ψ_1 without sample and then

[6] I apologize for color-blind readers as the color classification may not be clear. Still, the text is aimed to be informative enough to follow.

only wave ψ_2 without sample). This is highlighted with the cyan box for ψ_1 and the orange box for ψ_2. By denoting each measurement as a current J, we can express the experimental procedure to record the mutual scattering current J_{MS} as:

$$J_{\mathrm{MS}} = J - J_1 - J_2 - (J_{\mathrm{NS}} - J_{1,\mathrm{NS}} - J_{2,\mathrm{NS}}) \tag{1.20}$$

were each subscript describes the experiment; J is the current when both incident beams are present, and the sample is placed in the experiment, J_{NS} is the current when both incident beams are present, and no sample is placed in the experiment, J_i is the current when only $\psi_{\mathrm{in},i}$ is present, and the sample is placed in the experiment, and $J_{i,\mathrm{NS}}$ is the current when only $\psi_{\mathrm{in},i}$ is present, and no sample is placed in the experiment. It should be noted that although we express the measurements as current J here, a detector measures the *integral of the current over the detector area*, called the flux F.

With the proposed procedure, we almost completely isolate the mutual scattering current J_{MS}. Nevertheless, there is one component, the cross-interference between the two scattered waves, that is not possible to separate. This is because the scattered wave is only present when the incident wave is also present, and as we measure in the direction of the incident wave, the scattered wave cannot be isolated. Still, as the scattered wave is a spherical wave and the incident wave is a plane wave, we reasonably expect the scattered wave to have a much smaller amplitude (of the order of 10^{-2} or less) than the incident wave in the far field at the detector position. Furthermore, an interference between two scattered waves, both with small amplitude, yields an even much smaller amplitude when compared to an interference between an incident wave and a scattered wave. Thus, for our case, we assume this cross-interference between scattered waves to have a negligible impact on our measurements. It remains to be tested whether this assumption holds for our experiments.

In the theoretical framework we just described, our measurement procedure may be simplified even further by noticing that, as the incident waves are plane waves, they are proportional to a delta function in their incident direction, as shown in Eq. 1.17. Thus, if we measure in the direction of only one of the incident waves, the second incident wave does not affect the current. Still, we must be careful about this assumption while doing experiments because our incident waves are not plane waves but Gaussian collimated beams with a finite divergence. Thus, the two incident waves may still overlap at the detector area, especially for small angles.

1.5 Outline of the thesis

In this thesis, we study and apply light modulation to different scenarios. This thesis can be separated into three projects. The first and foremost project is related to the mutual scattering effect, a newly discovered effect of which the first experimental measurement is presented in this thesis. Chapters 3, 4, and 5 are related to this topic. The second project concerns wavefront shaping, a

modulation technique based on optimizing light intensity. This project is presented in Chapter 6. Finally, the third project concerns speckle correlations and how they can be used for encryption applications. In particular, we extend previous encryption methods using a scattering layer to a system where we used *two* scattering layers to increase secrecy. Chapter 7 is related to this topic.

In Chapter 2, we present details of the experimental techniques used in this thesis that in other forms of publications, such as research papers, are omitted for brevity. The extensive description is explicitly meant for other experimentalists to duplicate and reproduce our experiments. In particular, we focus on ongoing experiments and protocols to measure the mutual scattering effect.

In Chapter 3, we present the first observations of mutual scattering. We use two incident light beams to control the transparency and the opacity of a single human hair and a silicon bar.

In Chapter 4, we extend the observations of mutual scattering to measure the phase information. We use this new information to characterize different samples, and we believe this applies to an extensive range of materials. In particular, we measure mutual scattering on a single human hair, a polystyrene sphere, zinc oxide, and pultruded carbon.

Chapter 5 presents the first results of using mutual scattering to optimize light extinction in a specific direction. To this end, we extend the mutual scattering experiments from 2 to as many as $N = 64$ incident light beams. We compare mutual scattering with wavefront shaping, where mutual scattering optimizes *light extinction* and wavefront shaping optimizes *intensity*.

In Chapter 6, we apply the wavefront shaping technique to a flexible freeform sample made of titanium oxide particles suspended in silicone. We use the wavefront shaping technique to enhance the intensity in a focal point at the back of the sample, and we compare the performance of wavefront shaping for different freeforms, changing the curvature of the sample and the illumination radii.

In Chapter 7, we study the speckle correlation in a system with multiple scattering layers. We send a binary message through two scattering layers and measure the speckle pattern generated between the two layers. We study whether there is a relation between the message sent and the intermediate speckle. As a result, we propose a communication link using our scheme for encryption based on our findings.

Finally, Chapter 8 summarizes the results of this thesis and provides an outlook to improve current experiments and possible future experiments related to them.

Chapter 2

Methods

We present a detailed account of the experimental procedure and techniques employed for measuring mutual scattering. We describe aspects often overlooked in abridged descriptions of experimental setups typical of scientific papers. We commence by outlining the modulation devices and techniques utilized, after which we discuss the correction of aberrations arising from these devices. Subsequently, we elaborate on the data collection and analysis procedure. Finally, we address the limitations of the current experimental setup and propose potential improvements.

2.1 Setting a digital micromirror device

2.1.1 Motivation for experimental design

To detect mutual scattering, we need to measure the light extinction. Mutual scattering is present when multiple beams illuminate a finite sample, and its magnitude depends on the relative angle and phase between the incoming beams. In our experiment, we start by measuring light extinction when $N = 2$ beams are incident in the sample before increasing the number of beams.

In the first experiments on mutual scattering (see Chapter 3), we used mechanical stages to translate and rotate a mirror to control the angle of the incident beam, and a liquid crystal phase retarder to control the phase (see Fig. 3.2). However, the mechanical devices lack the precision and stability we need to predict and measure the phase information of the mutual scattering effect. For that reason, we upgraded the setup, but the road towards the new setup was not without obstacles, as described in de Mots' report [74]. Initially, we tested using a rotating arm to keep the distance between the source and the sample constant, placing an optical fiber on the rotating arm. Unfortunately, due to the movement of the rotating arm, the phase of the beam coming from the fiber fluctuates significantly when changing the angle. Finally, the setup was upgraded to use an active **wavefront modulator**. The incident wave $\boldsymbol{\Psi}$ is considered to propagate in the lateral $z-$direction, hence the wavefront $\boldsymbol{\Psi(x, y)}$ is taken to depend on the transversal (x, y) coordinate as

$$\boldsymbol{\Psi(x, y)} = \boldsymbol{A}(x, y)\, \exp^{-i(\omega t + \phi(x,y))}, \tag{2.1}$$

with ω the reduced frequency of the beam, t time, and (x, y) the transversal coordinates.

The active device controls the amplitude $\boldsymbol{A}(x, y)$ and phase $\phi(x, y)$ of the incident wavefront $\boldsymbol{\Psi(x, y)}$. Fig. 2.1 shows an example of the modulated phase $\phi(x, y)$. To control the angle and phase of $N = 2$ incident waves using a single active device, we place a focusing lens in front of the device and we only activate two sub-areas $\mathcal{A}_1$ and $\mathcal{A}_2$. In our realization, these areas are centroids at (x_1, y_2) and (x_2, y_2), with radii r_1 and r_2. To change the angle, the position of $\mathcal{A}_1$ is fixed and we change the position of $\mathcal{A}_2$. This change in position is converted into a change of angle because of the focusing lens (see Fig. 2.1).

The requirements presented above need to be addressed when choosing the modulation device. Because we need to activate the sub-areas of the active device, we need both amplitude and phase modulation. Besides, the modulation of the phase needs to be reliable and precise, and because of the number of measurements needed, high speed is desired. In the following sections, we examine the modulator device, aberration corrections, the measurement and analysis procedure, and possible improvements.

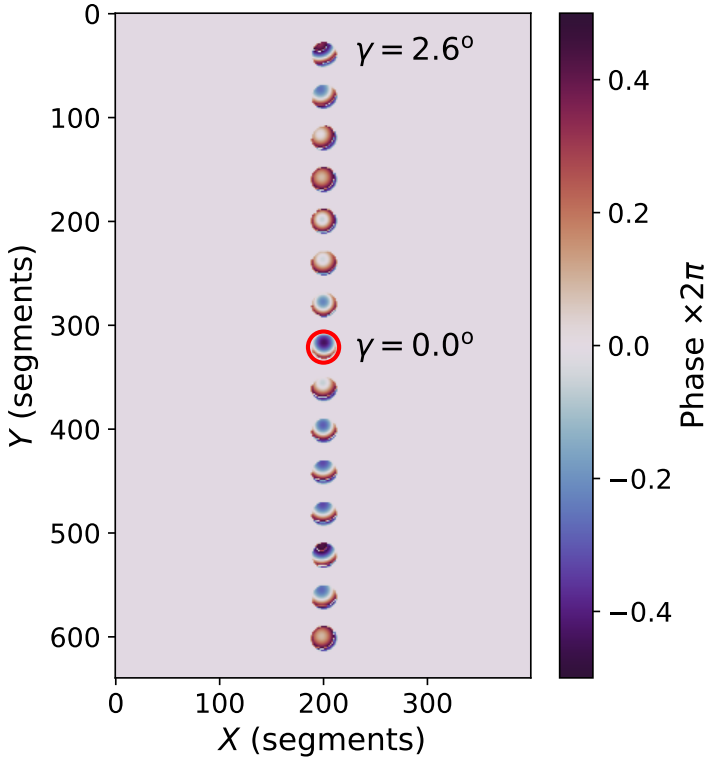

Figure 2.1: Spatial phase patterns $\phi(x, y)$ on the spatial modulation device to realize different incident light beams. The red circle highlights the central area, which is always activated. The different circles at different y correspond to different incident beams ranging from $\gamma = -2.6^\circ$ to $\gamma = +2.6^\circ$. All pixels outside the circles have phase *and amplitude* 0. The color bar gives a circular scale (the color at 1 is the same as the color at -1) to account for the periodicity of the phase. This figure is also shown in Chapter 4.

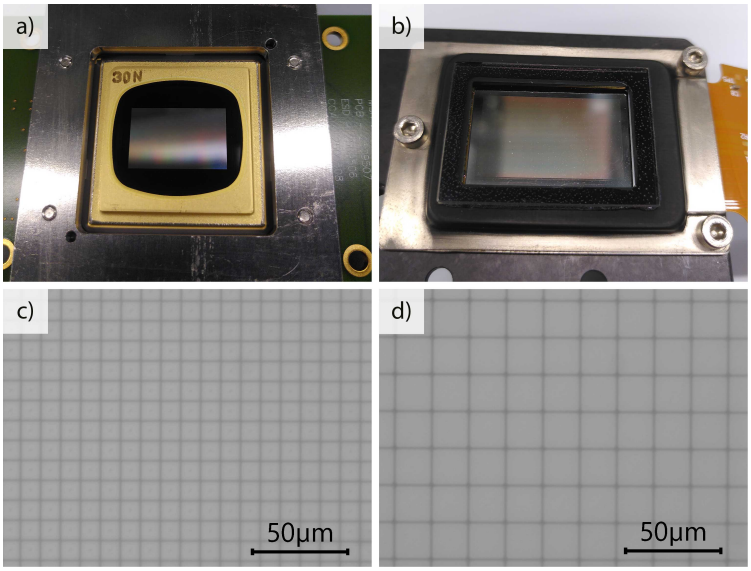

Figure 2.2: Macroscope picture of a) a DMD and b) an SLM, along with microscope pictures of the pixels of c) the DMD and d) the SLM.

2.1.2 Modulation devices

In wavefront shaping — and wavefront modulation in general — an active device is required to modulate amplitude $\boldsymbol{A}(x, y)$ and phase $\phi(x, y)$ (see Eq. 2.1). Spatial light modulators (SLMs) and digital micromirror devices (DMDs) are two commonly used modulation devices with advantages and disadvantages. Table 2.1 compares some relevant characteristics of state-of-the-art SLMs and DMDs.

An SLM is a liquid crystal-based device, also called liquid crystal on silicon (LCOS) (Fig 2.2). An SLM has a grid of micro mirrors on top of a silicon complementary metal oxide semiconductor (CMOS) back layer, covered with a liquid crystal layer (*e.g.*, twisted nematics). The incident light travels through the liquid crystal layer before and after reflecting in the micromirrors. By inducing a voltage with the CMOS back layer, we control the local refractive index of the liquid crystal layer, and thus we induce a phase change in the reflected light [75]. Because the change in refractive index is from a rotation and re-arranging of the liquid crystal molecules, the phase modulation is relatively slow, with a response time of a few milliseconds [76, 77].

A DMD is a mechanical device that consists of a grid of micro-mirrors where each mirror functions as a pixel [78] (Fig 2.2). These mirrors are fabricated on top of mechanical actuators that can change the mirror's orientation or tilt, affecting the light's angle of reflection. The mirrors have three states: ON, OFF, and IDLE. In practice, the IDLE state is not used, and the DMD is considered a binary modulation device, with a response time in the range of tens of microseconds.

For the experiments described in this thesis, we aim to control both the amplitude $\boldsymbol{A}(x, y)$ and phase $\phi(x, y)$ of the wavefront. For this purpose, we choose a DMD for our modulation. The characteristics of the DMD promise a fast and stable phase control with the possibility of amplitude modulation. However, as previously mentioned, the DMD is a binary modulation device. Therefore, we need to use a holographic technique to convert this binary amplitude modulation to a phase and amplitude modulation.

	SLM	**DMD**
Brand	*HOLOEYE*	*VIALUX*
Model	PLUTO 2.1-VIS-130	VX4100
Screen area	1920×1080	1920×1080
Pixel width	8.0μm	10.8μm
Bit depth	8 bit	1 bit
Refresh rate	180 Hz	10.75 kHz
Response time	≈ 3 ms	≈ 13 μs
Wavelength range	500-670 nm	400-700 nm
Controller	Through HDMI cable	Included FPGA
Estimated price	18 000 €	11 900 €

Table 2.1: Relevant characteristics of state-of-the-art SLM and DMD devices. This information was accessed in the first half of 2023.

2.1.3 Holographic techniques

There are two popular holographic techniques to convert from binary amplitude modulation to phase modulation: the Lee holography technique [79, 80], and the superpixel method [81]. The Lee holography technique was developed in the 1970s by Lee as a computer-generated hologram [82] and adapted by Campbell, *et al.* as a phase modulation method [83]. However, it was not until 2012 that Conkey, *et al.* applied this technique to wavefront modulation [80]. This technique is based on using a spatial amplitude pattern in the DMD with a carrier spatial frequency ν_0 and a spatial phase $\phi(x, y)$

$$f(x, y) = \frac{1}{2}\left[1 + \cos\left(2\pi(x - y)\nu_0 - \phi(x, y)\right)\right], \tag{2.2}$$

with (x, y) the 2D coordinates of the spatial signal. In the Fourier plane, this pattern generates three distinct orders of diffraction, which we call the -1, 0, and +1 diffraction order. The hologram is off-axis diagonally with the carrier frequency selected to minimize crosstalk among diffraction orders by providing a large enough separation between them. It has been demonstrated [80] that by filtering only the +1 diffraction order, the resulting field has the phase $\phi(x, y)$, *i.e.*, we transform the spatial phase into a field phase. This field is the one expressed in Eq. 2.1.

Soon after the Lee holography was adapted in the wavefront shaping community, Goorden, *et al.* developed the Superpixel method [81]. This holography

technique uses a spatial filter in the Fourier plane and a spatial pattern to convert binary modulation into phase modulation. However, instead of using a spatial amplitude pattern with a carrier frequency, *the DMD itself is tilted* such that there is a phase gradient along the surface of the DMD. As the name suggests, this method uses *superpixels*. The idea is to take a collection of $n \times n$ pixels as a superpixel. Because the filter in the Fourier plane blurs the pattern, the superpixel has a resulting phase equal to the sum of the phases of each pixel inside it. Thus, to control the phase of a superpixel, we can turn ON or OFF certain pixels inside it such that the total sum is the phase we desire. This technique is substantially more power efficient and permits a better resolution of the phase modulation. Nevertheless, the DMD's alignment and the filter's position in the Fourier plane are highly specific and depend on the number of pixels per superpixel and the wavelength used.

For our experiments, we decided to implement the Lee holography technique. The main reason for this decision is that the position and tilt of the DMD in the Superpixel method depend on the wavelength of the source. In the setup built for mutual scattering experiments, one of the possible future projects involves sweeping the wavelength of the source. Thus, we want to minimize changes in the setup because of changes in wavelength.

We only need binary modulation of the amplitude to select the active areas $\mathcal{A}_1$ and $\mathcal{A}_2$, so we do not need more amplitude modulation than the readily available binary modulation of a DMD. Nevertheless, the DMD permits better amplitude modulation. For this, we need only to follow the same principle as in the superpixel method and take a collection of pixels $m \times m$. Depending on how many pixels are ON or OFF, we modulate the resulting amplitude of the superpixel.

2.1.4 Aberrations

A DMD is a mechanical device, which makes it reliable. Besides, commercially available DMDs include user-friendly software and libraries. For many applications, the binary modulation is sufficient, and no further correction is needed. For instance, commercially available screen projectors (or beamers) are widely used daily. Unfortunately, this is not the case in our experiments.

In the experiments presented in Chapter 4, we use two active sub-areas of the DMD to generate two incoming light beams, and a focusing lens to cross the beams at a certain angle, placing the sample at the focal point, *i.e.*, the crossing point. Any aberration or misalignment on the incoming wavefront nullifies the option of a perfect focus, and thus we cannot approximate the incoming beams as plane waves. This was the case for the first months of the experiments. The aberrations were so strong that, when changing the angle between the two beams, they did not cross at the sample.

After many modifications and improvements to the experiment, we realized that the source of the aberrations was the DMD itself. Fortunately, this issue is well documented by Popoff [84]. The aberrations are believed to be imperfections of the individual mirrors, particularly the flatness of the surface. The effect of

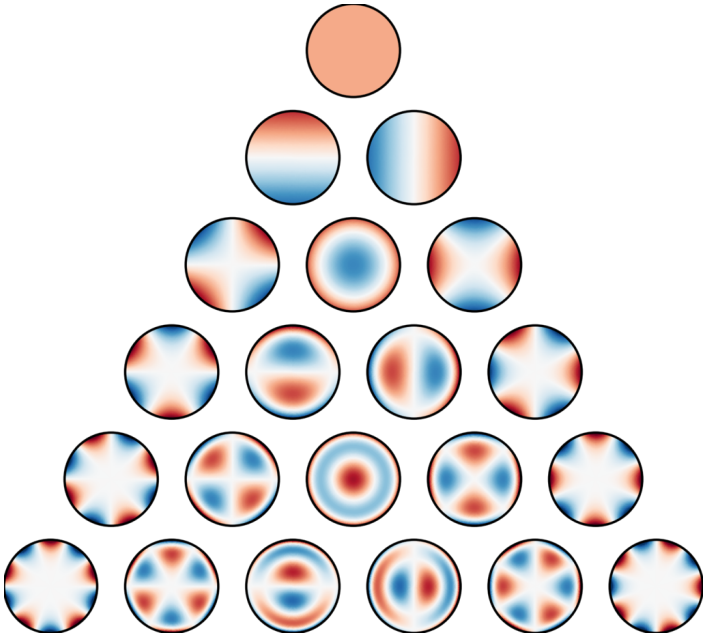

Figure 2.3: The first 21 Zernike polynomials were calculated using the Orthopy Python library [89], ordered vertically by radial degree and horizontally by azimuthal degree. Figure retrieved from wikipedia.org on May 2023, credits to user Nschloe, CC BY-SA 4.0 `https://creativecommons.org/licenses/by-sa/4.0`, via Wikimedia Commons.

every single mirror adds up, resulting in a non-negligible effect.

The solution presented in Ref. [84] is to use a particular phase pattern on the DMD to counteract the aberrations. Wavefront aberrations have been widely studied in the past [85], and the most common aberrations are described using *Zernike polynomials* [86, 87].

Zernike introduced Zernike polynomials in the 1930s [88] as a basis to describe any wavefront. Similar to Fourier analysis, we can decompose a wavefront in Zernike polynomials given a large enough number of components. In Fig. 2.3, we show a simulation of the first Zernike polynomials. What sets the Zernike polynomials apart from other representations is that each coefficient is related to a type of aberration, such as spherical aberrations, coma, astigmatism, and more. The specificity of the coefficients eases the interpretation of aberrations measurements.

In the original solution to correct the aberrations of the DMD presented by Popoff, the coefficients of the Zernike polynomials are optimized iteratively so that the intensity at the focal point is maximized. Although this yields good results, we realized that the point spread function (PSF) at the focus is not optimal, even though the intensity is maximized at the center. For our experiments, we decided to simulate the PSF beforehand and maximize the *image correlation* between the simulated PSF and the one obtained in our experiments instead of

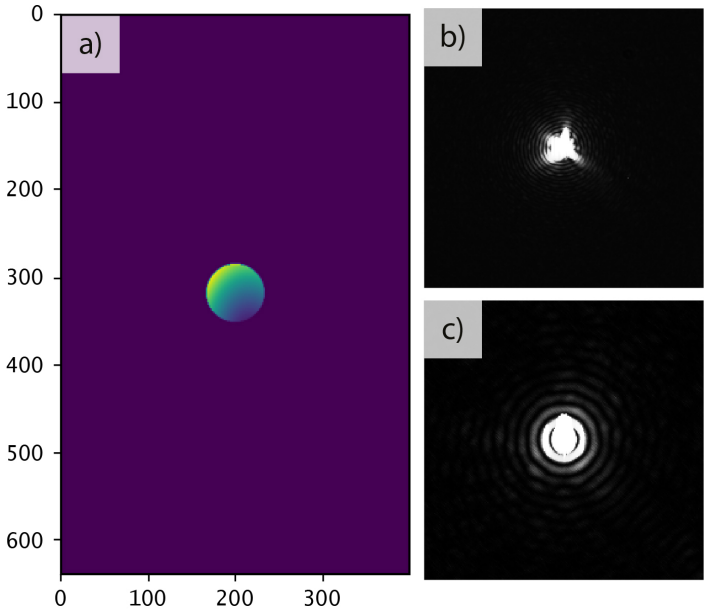

Figure 2.4: Example of a PSF optimization using Zernike polynomials. a) the optimized phase mask of a circular active area, b) PSF before optimization, and c) PSF after optimization. The CCD pictures are highly saturated to showcase the circular fringes around the focus. It should be noted that these pictures were not used in the optimization itself. The resolution between active areas may differ.

maximizing the intensity at a certain point. This method provides us with the correction we seek, as shown in the example in Fig. 2.4.

2.2 Data analysis for mutual scattering measurements

2.2.1 Flux measurements

In Chapter 1.4, we provide an explanation of the theoretical background and the experimental procedure for measuring the mutual scattering effect. Although we explain how to obtain the extinction modulation from flux F measurements using ancillary measurements, some practical details still need to be included for conducting real experiments. In particular, a recurrent obstacle is that, when measuring angle dependency, the position of the detector needs to change.

To overcome this obstacle in our first experiments, which we present in Chapter 3, we changed the angle of only one of the two incoming beams and measured the mutual scattering of the static beam. We use a charged couple device (CCD) camera as a detector, placing it far (> 1m) from the crossing point where the sample is positioned. This arrangement ensured that the second beam would not

hit the detector area even for small angles, and we only measured the stationary beam. Furthermore, we set the width of the beam such that it almost fully covers the whole detector area. With this, we obtained the flux F as the sum of counts over all the camera pixels. Since we normalized F, converting from CCD counts to real units was not necessary.

One of the additions in the new experimental setup described in Chapter 4 is the ability to simultaneously measure the mutual scattering for both directions. In this case, we also use a CCD camera for the measurements, but the beam area is much smaller than the detector area, so both beams are measured simultaneously. The distance between the detector and the sample is such that even for the largest angle measured, both beams are still fully detected. However, a significant drawback of this arrangement is that making the beam smaller also reduces the signal-to-noise ratio (SNR). We currently use low-power laser sources of the order of tens of milliwatts, and increasing the power of the source is a viable solution to increase the SNR without risking damaging the sample.

Although we do not need to physically move the detector, the beam position within the detector area changes. Since both beams are present simultaneously, summing up all pixels in the camera is not an option, and we need to detect the region of interest (ROI) of each beam. For the simplest scenario where we place no sample in the crossing point, the position and width of the ROI for each angle are fixed, so we could calibrate the setup once and use the same calibration for all measurements. However, in our experiments, we use samples embedded in PDMS. Due to the change in refractive index n, the position of the ROI is not the same with or without the medium. Furthermore, changes in the thickness of the PDMS layer also change the position of the ROI. For this reason, we decided to estimate the ROI for each measurement in the analysis *a posteriori*.

In our experiments, we measure phase dependency and angle dependency. We measure multiple steps ($N = 30$) of the relative phase between the two beams for each angle, going from 0 to 2π. To have statistical information, we repeat this for several iterations ($M = 3$). The position of the ROI is only dependent on the angle and not the phase of the incoming beam, so we consider the same ROI for all the measurements that have the same angle. To estimate the ROI of each beam for a certain angle, we employ the following procedure: (1) first, we add all the $M \times N$ pictures taken for this angle (Fig. 2.5b). We do this because the sample and the medium induce a diffraction pattern that depends on the phase, so adding up all the pictures reduces this effect. (2) Then, we apply a Fourier filter to get rid of the high-frequency (spatial) signals (Fig. 2.5c). This filter reduces the effect of the diffraction patterns and allows us to approximate the ROI to a Gaussian distribution. (3) We continue by taking the position of the pixel with the highest intensity, and we take a sub-area with a width $1.5\times$ the desired width of the ROI, which is set by the user. Ideally, the pixel with the highest intensity should be at the center of the beam, and thus no further analysis should be needed. However, because of the diffraction pattern, this is not always the case, so we use a Gaussian fit to estimate the real center. (4) With this sub-area, we take two vectors by collapsing the 2D image in either the x or the y-axis. Then, we fit both vectors with a Gaussian profile, and we get the

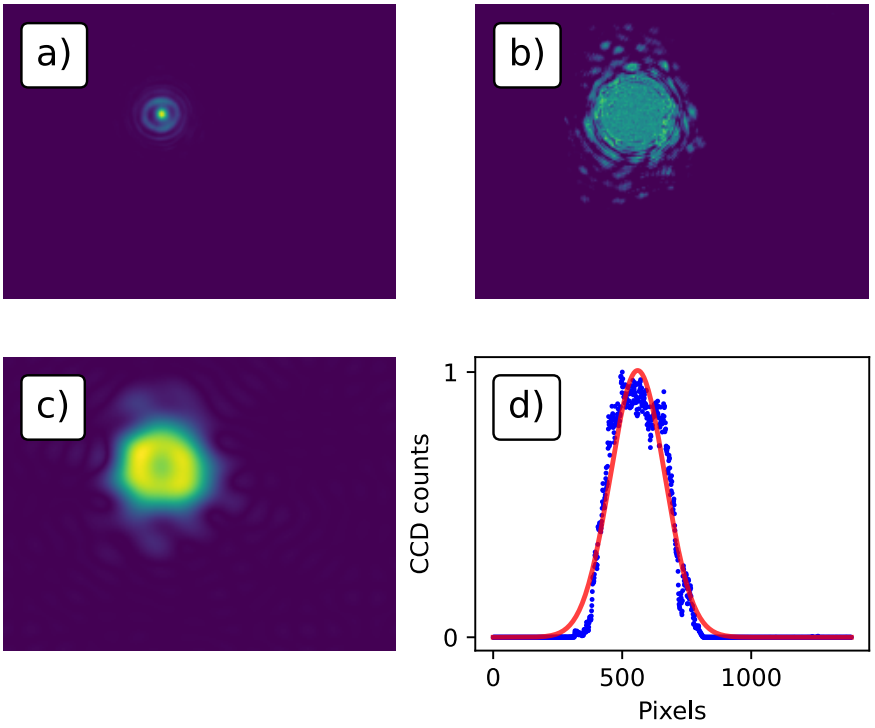

Figure 2.5: Steps to get ROI. a) Example picture of a single beam passing through the sample. b) Total sum of all pictures with the same angle. c) Total sum after passing through an FFT filter. d) Gaussian fit to the collapsing of the previous image into the x-axis.

position in x and y of the center of the ROI from this fit (Fig. 2.5d). Although imperfect, this method proved to be good and reliable for our data.

2.2.2 Phase information

The mutual scattering effect is the component of the total extinction that we modulate by cross-interference between the incoming wave of one beam and the scattered wave of another. This effect depends on the phase and angle between the beams. While the phase dependency always follows a cosine behavior, the angle dependency follows a trend set by the scattering amplitude f of the sample. Therefore, for experiments on scattering characterization, the phase dependency data is only relevant as a means to an end, and we care about three parameters: the maximum value, the minimum value, and the phase that reaches the maximum value.

Since we know the behavior of the phase dependency, we can fit it with a cosine curve and extract the three relevant parameters (maximum, minimum, phase at

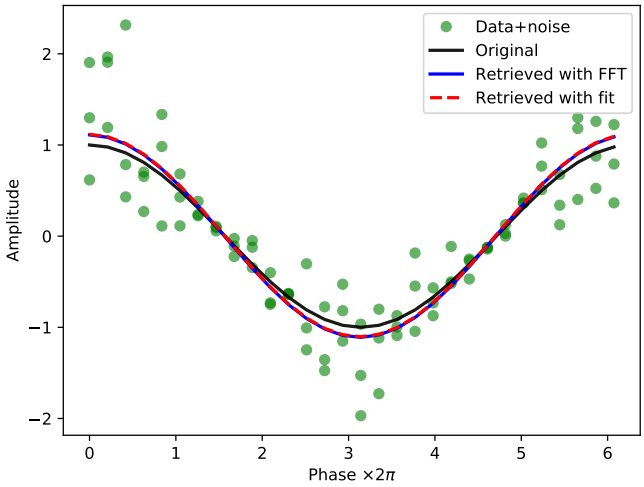

Figure 2.6: Example of the two methods to extract the amplitude and phase of the data. We simulate a noisy measurement with the green symbols based on a cosine curve with Gaussian noise. The original simulated cosine is shown in black. The curves extracted with the two described methods are shown in solid blue (FFT method) and dashed red (cosine fit method). The two curves are almost overlapping.

maximum) from the fit. Another solution is to take the Fourier transform and extract the component at the expected frequency of the cosine curve. The results of both methods are very similar, and there is no statistical difference in the final result (see Fig. 2.6). Nevertheless, fitting is a process that is very susceptible to the initial guess, and for signals with low SNR, the fit might fail. Hence, we decided to take the Fourier approach.

We consider the error r of our estimation as the average difference between the Fourier component and the data given by

$$r = \frac{\sum_n |x - \bar{x}|}{n}, \tag{2.3}$$

where n is the number of points, x is the fit data, and $\bar{x}$ is the experimental data.

We treat the error of the phase estimation differently because, although they are related, an uncertainty of the amplitude does not have the same magnitude as an uncertainty of the phase. To obtain the error of our phase estimation, we use an iterative process, which we illustrate in Fig. 2.7. We add phase offsets to the experimental data and calculate the amplitude error for every new phase offset. The offset where the amplitude error is *twice* the original amplitude error is chosen as the error range of our phase estimation. For example, if the original amplitude error is 10%, we start adding phase offsets until we reach an amplitude error of 20%. The amount of phase offsets we added is what we consider as the

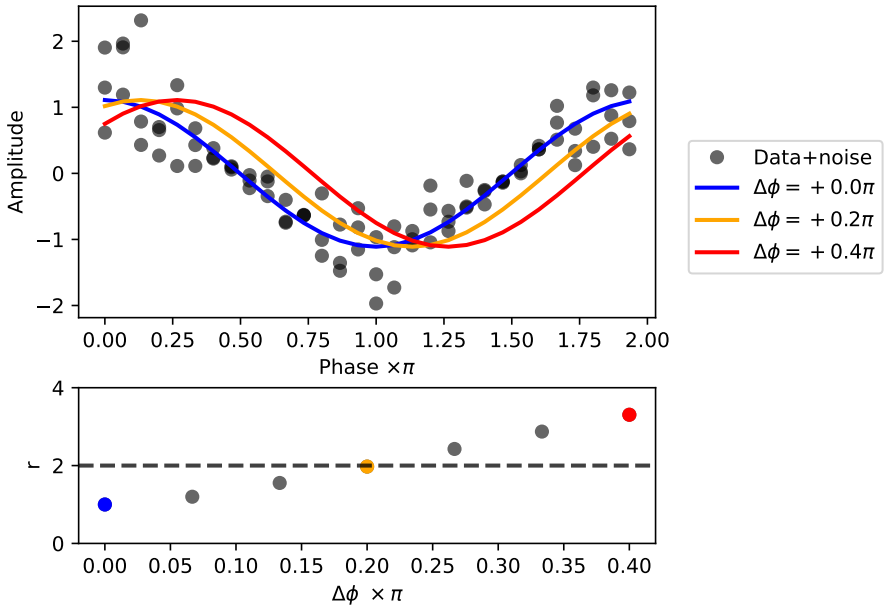

Figure 2.7: We use the same simulated data as in Fig. 2.6 to illustrate how we estimate the error of the extracted phase. The raw data is shown in the top panel as gray symbols, and the extracted cosine is shown in blue. To estimate the error of the phase, we add phase offsets $\Delta\phi$ iteratively, illustrated with the orange and red curves. For each iteration, we calculate the error (Eq. 2.3) shown in the bottom panel, normalized w.r.t. the initial error. The colored dots (blue, orange, and red) are related to the solid curves of the top panel. We estimate the error of the extracted phase as the phase offset that doubles the initial error. We illustrate this with the horizontal dashed black line in the bottom panel. We see that the yellow dot is the first one to surpass the limit. Thus, for this case, we select $\Delta\phi = 0.2\pi$ as our error.

phase uncertainty. If we reach an offset equal to 2π and the amplitude error is still not doubled, we consider the phase to be *undefined*, *i.e.*, the data does not have a cosine-like shape, and we are not able to estimate the phase of the data.

2.3 Limitations and possible improvements of mutual scattering experiments

2.3.1 Design choices

The mutual scattering effect has three key assumptions: the detector is in far field, the incoming wave is still present at the detector, and the incoming wave is a plane wave. The third assumption is due to the current extent of the theory, but

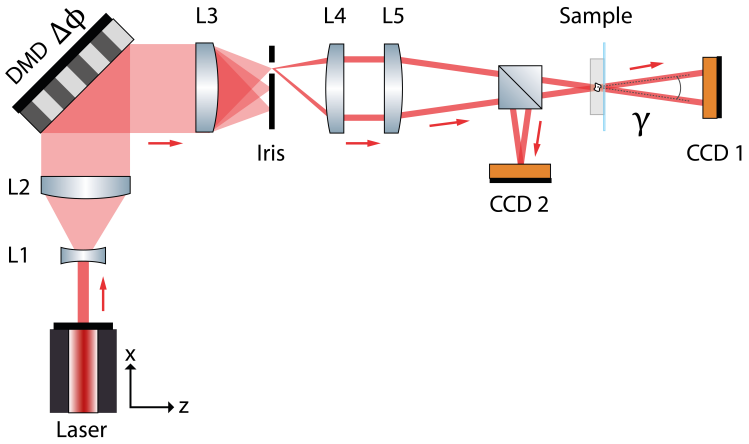

Figure 2.8: Diagram of the experimental setup, as shown in Chapter 4. The two incoming beams are generated using active areas in the digital micromirror device, which also sets the phase difference between the beams $\Delta\phi$. Lenses L3 and L5 and the iris are used for the holographic filter needed for the Lee holography technique, which allows us to control the phase of the wavefront. The two beams are focused into the sample by lens L5 forming an angle γ, and then collected by camera CCD1. A beamsplitter is placed in front of the sample such that the reflection focuses on camera CCD2.

it is believed that cross interference is still present for more complex wavefronts (*e.g.*, Gaussian beams). Because we only have a few assumptions, it is reasonable to assume that mutual scattering can be used in a wide variety of experiments, either in very small or very big objects or even in other areas of physics, such as acoustics.

Although the abstract concept of mutual scattering has only a few physical limitations when designing a new experiment, we have to make decisions that limit the applicability of the experiment. Here, we describe such decisions and limitations.

The experimental setup built for the experiments shown in Chapter 4 — which is the one currently in use — was designed to address the limitations encountered in the experiment shown in Chapter 3. To be able to compare both experiments, we aimed to measure samples with similar dimensions, with a default width of $a = 100\mu$m. As we need the incoming beam to have a width larger than the sample, we decided to have a beam waist of $2\omega_0 > 1.5a = 150\mu$m. We decided to use the same wavelength as the previous experiment $\lambda = 632.8$nm. The setup is shown in Fig. 2.8 and described more in detail in Chapter 4.

We use the model shown in the appendix of Chapter 3 as a reference for the angular behavior of the mutual scattering. In this model, the mutual scattering follows a sinc-like behavior, and the first node is positioned at $\gamma_0 = \lambda/a \approx 0.36°$. From here, we make two decisions: first, we want to have at least three nodes, which means that the maximum angle we can measure must be $\gamma_{\max} > 3\lambda/a =$

1.09°. Second, we want to have at least three data points between nodes, meaning the angular definition must be $\Delta\gamma < \lambda/4a = 0.09°$.

The DMD used is a Vialux VX4100, which has 1920×1080 pixels and a pixel size of 10.8μm. The focal length L of the focusing lens is related to the maximum angle required and the height of the DMD, following

$$\tan\left(\frac{\gamma_{\max}}{2}\right) = \frac{D_{\text{dmd}}}{2L}, \tag{2.4}$$

$$\tag{2.5}$$

where $D_{\text{dmd}} = 1920 \times 10.8\mu\text{m} \approx 20.7\text{mm}$ is the height of the DMD. We decided to use a lens with a focal length of $L = 150$ mm. This gives us a maximum angle of $\gamma_{\max} \approx 3.95°$. We move the active areas in the DMD pixel by pixel. We approximate the angular resolution $\Delta\gamma$ using a similar formula as in Eq. 2.4, and we get $\Delta\gamma \approx 0.002°$, within the required limits.

The size of the active areas on the DMD depends on the beam waist required at the focus. If the area on the DMD is small enough, we can approximate each beam to a single ray and disregard the focusing effect of the lens within the same beam. To verify this assumption we use the free software GaussianBeam [90] to make a first estimation of the beam waist. We decided to use an active area of 72 pixels (~ 0.78 mm), which results in a beam waist at the focus of $\sim 155\mu$m. Finally, we estimate a divergence in the beam of $\theta \approx 0.119°$. We summarize the parameters ranges in Tab. 2.2.

Parameter	**Value**
Maximum angle $\gamma_{\max}$	3.95°
Angle resolution $\Delta\gamma$	0.002°
Beam divergence θ	0.119°
Beam diameter $2\omega_0$	155μm

Table 2.2: Relevant experimental parameters related to the decisions taken during design.

2.3.2 Phase calibration

Measurements that provide phase information are highly valuable because this information allows us to draw conclusions about the complex properties (*i.e.*, both real and imaginary parts) of the scattering waves generated by the sample. However, this high reward comes with a high effort, as the main challenge is comparing the phases of different angles.

In a perfect scenario, where we use a DMD for modulation, and a plano-convex lens for focusing, a phase difference $\Delta\phi$ between two active areas on the DMD would be preserved at the focal point, and no calibration would be necessary. However, as emphasized throughout this chapter, our experiments could be better.

Phase measurements are very susceptible to misalignment, evident from the almost $24,000 : 1$ ratio between the focal length of our lens and the wavelength.

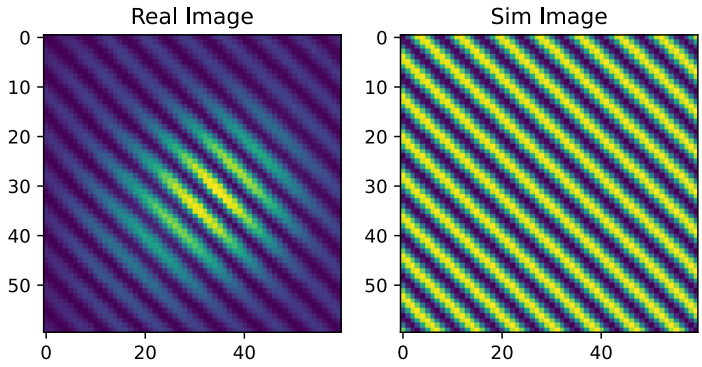

Figure 2.9: Example result of fringes fit. Left: the real fringes measured with CCD2. Right: the simulated fringes after fitting using the structural similarity index.

Correctly estimating the phase is challenging because any change in path length resulting from a change in angle adds a dephasing effect. For example, suppose we set an angle γ_1 with a phase difference $\Delta\phi_{\gamma_1}$. Now we change the angle gamma to γ_2 without adapting the phase difference ($\phi_{\gamma_2} = \Delta\phi_{\gamma_1}$ at the DMD). Any aberration, misalignment, or change of medium induces an additional dephase, such that $\Delta\phi_{\gamma_2} \neq \Delta\phi_{\gamma_1}$ at the sample position. Fortunately, the DMD is a very reliable and reproducible element, and we can calibrate and compensate for errors in the setup beforehand rather than struggling to achieve perfect alignment.

To calibrate our setup, we place a beamsplitter between the focusing lens and the focus, and we placed a second CCD camera at the focal point of the second arm. When measuring the intensity at the crossing point between two beams, we see the interference fringes (Fig. 2.9). The periodicity of the interference fringes T is related to the angle γ between the two beams. We can calculate this relation either by using the double slit formulation ($\tan(\gamma) = \lambda/T$) or assuming plane waves ($\sin(\gamma) = \lambda/T$). Both approximations hold for small angles. Similarly, we can estimate phase changes by looking at the displacement of the fringes. When comparing two pictures of fringes, the phase difference is calculated as $\Delta\phi = 2\pi\Delta x/T$, where Δx is the difference in the position of the fringes.

The most successful approach to calibrate phase and angle by looking at the fringes was to use the metric of *structural similarity index* [91, 92]. For every picture of fringes, we simulated a fringes pattern with T and $\Delta\phi$ as inputs. Then, we fit our model to the picture to obtain T and $\Delta\phi$. Instead of maximizing correlation or mean squared error, the fit maximized the structural similarity index. See Fig. 2.9 for an example. This metric considers not only differences in the pixel values but changes in the structure, *i.e.*, the spatial pattern, of an image.

Using this approach, we are able to calibrate the phase and angle between the two incoming beams. Sadly, this calibration does not apply to our experiments. Firstly, the CCD camera used for our experiment has a protective glass layer

with a refractive index of $n_g = 1.5$. This does not affect the angle calibration, but it does affect the phase calibration; if one beam is perpendicular to the glass surface and the other beam is angled, the difference in refractive index causes a change in path length and thus a change of phase. Nevertheless, as the properties of this layer are known, we can account for it in the phase estimation. But again, the phase estimation is sensitive to misalignment, and any camera tilt should be accounted for. Thus, we can add the effect of the protective glass layer as an additional dephase, given by

$$\Delta\phi = \frac{2\pi n_g (l' - l)}{\lambda n_{air}}, \tag{2.6}$$

$$\tag{2.7}$$

with

$$(l' - l) = \left(\frac{D_g}{\cos(\alpha)} - \frac{D_g}{\cos(\alpha')} \right), \tag{2.8}$$

$$\sin(\alpha') = \frac{n_{air}}{n_g} \sin(\alpha), \tag{2.9}$$

$$\alpha = \gamma + \alpha_c, \tag{2.10}$$

$$\tag{2.11}$$

where n_{air} is the refractive index of air, $D_g = 0.5$mm is the thickness of the glass (camera model Stingray F-125), α_c is the tilt of the camera, and γ is the angle between the incoming beams.

Similarly, our samples are embedded in PDMS, which affects both angle and phase estimation. This change depends both on the depth of the sample and the tilt of the PDMS surface. With all things considered, the effect of the medium can be estimated as

$$\Delta\phi = \frac{2\pi}{\lambda} \left((l - d) - \frac{n_m}{n_{air}} (l' - d') \right), \tag{2.12}$$

$$\tag{2.13}$$

with

$$(l - d) = \left(\frac{D}{\cos(\gamma - \alpha)} - \frac{D}{\cos(\alpha)} \right), \tag{2.14}$$

$$(l' - d') = \left(\frac{D}{\cos(\gamma' - \alpha')} - \frac{D}{\cos(\alpha')} \right), \tag{2.15}$$

$$\sin(\alpha') = \frac{n_{air}}{n_m} \sin(\alpha), \tag{2.16}$$

$$\sin(\gamma' - \alpha') = \frac{n_{air}}{n_m} \sin(\gamma - \alpha), \tag{2.17}$$

$$\tag{2.18}$$

where n_{air}, n_m are the refractive index of air and the medium, respectively, D is the depth of the sample in the medium, α_m is the tilt of the medium, and

γ is the angle between the incoming beams. Unfortunately, the contributions presented in this section are highly sensitive to unknown parameters, and using estimates is no better than an educated guess. For this reason, the corrections are not implemented in the results presented in Chapter 4. A possible solution is to remove the protective layer of the second CCD camera and place a PDMS layer with the same thickness as the depth of the sample. Even further, we may submerge the whole optical setup in an index-matching liquid. However, this solution is invasive and requires knowing the depth of all the samples precisely.

Before using the structural similarity index, we attempted to obtain the phase and periodicity of the fringes using Fourier analysis. This seemed straightforward: finding the peak at the Fourier transform and obtaining its complex value can get both phase and periodicity. However, we realized a mathematical limitation after many struggles. *When obtaining the phase of an FFT component, the phase is only meaningful if the frequency of the component is an integer divisor of the array.* If this is not fulfilled, the phase information is completely random. This is a numerical limitation of the discrete nature of the FFT. In our case, the frequency of the fringes is variable. We attempted to guess the frequency of the fringes for every picture and adapt the length of the array (*i.e.*, the size of the picture) in an iterative way. This method did not converge, so we changed to the analysis in real space. It is noteworthy that the Fourier method is the one followed by measurements of the transmission matrix. [28, 29, 67, 93, 94] Although the frequency of the fringes is known and easily controllable in those measurements, as far as we know, this mathematical limitation has yet to be explored.

Chapter 3

Observation of mutual scattering of light

Interference of scattered waves is fundamental for light-scattering techniques, including modern developments such as optical wavefront shaping. Recently, a new type of wavefront shaping was introduced where the *extinction* is manipulated instead of the scattered *intensity*. The underlying idea is that upon changing the phases or the amplitudes of incident beams, the total extinction will change due to interference as described by the cross terms between different incident beams. Here, we experimentally demonstrate mutual scattering in scattering media, in particular, a human hair and a silicon bar. To this end, we send two light beams with a variable mutual angle on the sample. Depending on the relative phase of the incident beams we observe either nearly zero extinction — mutual transparency — or almost twice the single-beam extinction — mutual extinction — in agreement with theory. In the theory, we use an analytical approximation for the scattering amplitude starting from a completely opaque object and discuss the limitations of our approximation. We discuss the applications of mutual scattering in various fields such as non-line-of-sight communications, microscopy, and biomedical imaging.

Parts of this chapter have been published in A. Rates, A. Lagendijk, O. Akdemir, A. P. Mosk, W. L. Vos, Physical Review A **104**, 043515 (2021) [70].

3.1 Introduction

Random scattering of light inside complex materials such as clouds, paint, milk, white LEDs, hair, or human tissue is what makes them appear opaque [9, 20, 53, 95, 96]. In these inhomogeneous materials, multiple scattering and interference distort the incident wavefront so strongly that the spatial coherence is immensely reduced [97]. The invention of optical wavefront shaping (WFS) [43], where N multiple waves are incident on a complex sample with adjustable phases and amplitudes, has revolutionized the study of scattering of light in nanophotonics and led to exciting applications, such as transmission optimization [44, 67, 98–100], light focusing [63, 64, 93, 101–104], light absorption and energy density control [72, 105–107], and new biomedical imaging techniques [64, 108–110].

In the absence of absorption, the power extinguished from an incident beam is equal to the total scattered power, a well-known conservation law called the optical theorem [111]. The standard formulation of the optical theorem considers only a *single* ($N = 1$) incident wave [112]. Naively using the single-beam optical theorem in the case of scattering with N multiple incident waves, a situation typical of WFS, leads to a violation of energy conservation. We have recently derived a generalized optical theorem to describe the scattering and extinction by *multiple* incident waves [69]. A crucial part in the derivation of the generalized optical theorem was the exciting discovery that multiple incident waves show *cross-extinction*, illustrated in Fig. 3.1. This phenomenon does not exist in common single-beam forward scattering or self-extinction, since the phenomenon is caused by interference between the scattered part of one incident beam and the coherent part of another beam. This cross-interference is always present, whether the samples are scattering or absorbing, and depending on the phases between the beams the interference is constructive or destructive, making it relevant for an *ab initio* description of WFS.

Mutual scattering allows us to control the total extinction by manipulating the phase difference between two incident beams. Depending on the angle formed by the two incident beams, when varying the phase the light extinction is varied by as much as $\pm 100\%$ in the case of $N = 2$.

In this chapter, we present an experimental observation of the mutual scattering of two beams crossing in a scattering medium that, to the best of our knowledge, has never been observed before. We study the situation with $N = 2$ beams since it is the simplest form of N-beam interference, as is typical of wavefront shaping. In our experiments, we study two different kinds of samples. The first type of sample is a human hair, which is a biological sample with a naturally near-cylindrical cross-section [113]. The second type of sample is a silicon bar with a rectangular cross-section made from a crystalline-Si wafer as used in CMOS fabrication, see, *e.g.*, Ref. [114, 115].

We compare our experimental results with an analytical approximation based on the mutual scattering theory, and we discuss when this approximation fails. Finally, we discuss several applications of mutual scattering.

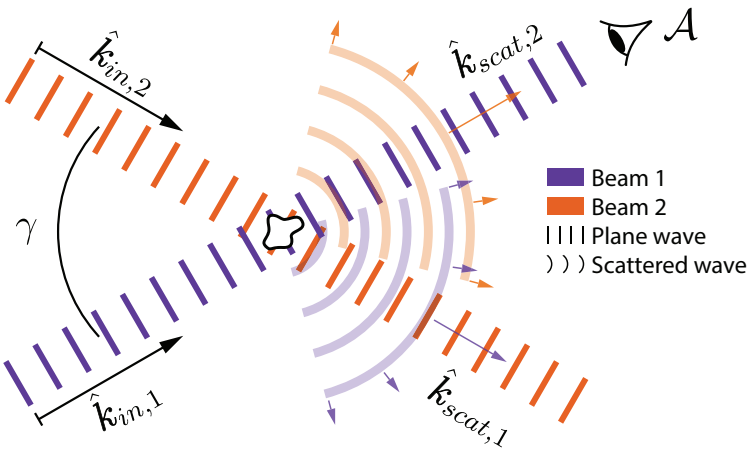

Figure 3.1: Schematic of two-wave mutual scattering: $N = 2$ beams with wavevectors $\hat{k}_{\mathrm{in},1}$ and $\hat{k}_{\mathrm{in},2}$ and mutual angle γ are incident onto a scattering sample. The scattered waves are shown as curved wavefronts to emphasize that they are present at all outgoing directions (with wavevectors $\hat{k}_{\mathrm{scat},1}$ and $\hat{k}_{\mathrm{scat},2}$). Scattered waves interfere with coherent beams leading to either mutual extinction or mutual transparency. The arrow colors distinguish the scattered waves and do not represent different wavelengths. The detector has an area $\mathcal{A}$ and is placed in the far field, hence it is clear that the dimensions are not to scale.

3.2 Power flux and mutual scattering

In a light scattering experiment, a detector with area $\mathcal{A}$ that is placed in the direction of the wavevector $\hat{k}_{\mathrm{det}}$ detects in far-field the power flux or Poynting vector [54]. In the scalar-wave approximation, the flux equals the current density[1] $\boldsymbol{J}$ integrated over $\mathcal{A}$ (see Fig. 3.1). When only one beam (beam 1) is incident in the scattering medium with wave vector $\hat{k}_{\mathrm{in},1}$, the power flux F observed by the detector is equal to [53]

$$F_{1,1} = F_1^{\mathrm{in}} - F_1^{\mathrm{ext}} + F_1^{\mathrm{scat}}, \tag{3.1}$$

where F_1^{ext} is the flux removed from the incident flux F_1^{in} due to interference between the outgoing coherent wave and the scattered waves. Since scattered light from beam 1 is present at all angles, a fraction of the scattered flux F_1^{scat} with wavevector $\hat{k}_{\mathrm{scat},1} = \hat{k}_{\mathrm{det}}$ is also scattered into detection area $\mathcal{A}$.

If a second beam (beam 2) is also incident, with a different wavevector $\hat{k}_{\mathrm{scat},2} \neq \hat{k}_{\mathrm{det}}$, *i.e.*, not in the direction of the detector, the power flux at the detector becomes

$$F_{1,2} = F_{1,1} + F_2^{\mathrm{scat}} + F_{1,2}^{\mathrm{scat}} + F_{1,2}^{\mathrm{cross}}. \tag{3.2}$$

[1] For a scalar wave ψ, the flux F is equal to $F \equiv \int_{\mathcal{A}} \boldsymbol{J}\mathrm{dA} \equiv -\int_{\mathcal{A}} \mathrm{Re}\left[(\partial_t \psi)^* \boldsymbol{\nabla}\psi\right]\mathrm{dA}$

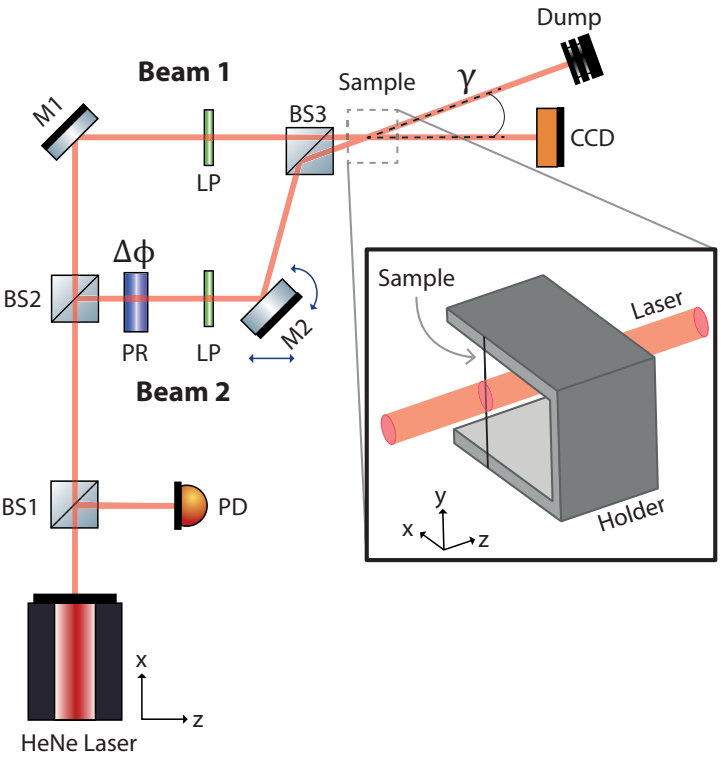

Figure 3.2: Schematic of the experiment. The angle γ between the two beams is controlled by moving and rotating mirror M2 and an LC phase retarder controls the phase difference $\Delta\phi$ between the two beams. The inset shows the position of the sample related to the direction of beam 1. (M: mirror; PD: photodiode; BS: beamsplitter; LP: linear polarizer; PR: phase retarder.)

Here, F_2^{scat} is the flux of the scattered fraction of beam 2 incident into the detector with wavevector $\hat{k}_{\text{scat},2} = \hat{k}_{\text{det}}$, similar to F_1^{scat} above. $F_{1,2}^{\text{scat}}$ is the cross term describing interference between the scattered waves from both incident beams. $F_{1,2}^{\text{cross}}$ describes interference between the coherent wave of the incident beam 1 and the scattered wave of the incident beam 2. This final term of Eq. 3.2 corresponds to either mutual extinction or mutual transparency, depending on its sign. In case of destructive interference, $F_{1,2}^{\text{cross}}$ is negative and the total extinction is increased, corresponding to mutual extinction. In the case of constructive interference, the total extinction is decreased, corresponding to mutual transparency. This term is present for both scattering and absorbing samples.

We experimentally obtain F_2^{scat} if we collect data when only the incident beam 2 is present, and we obtain F_1^{in} if we collect data without the scattering medium. Combining the data of the different situations, we get the desired interference

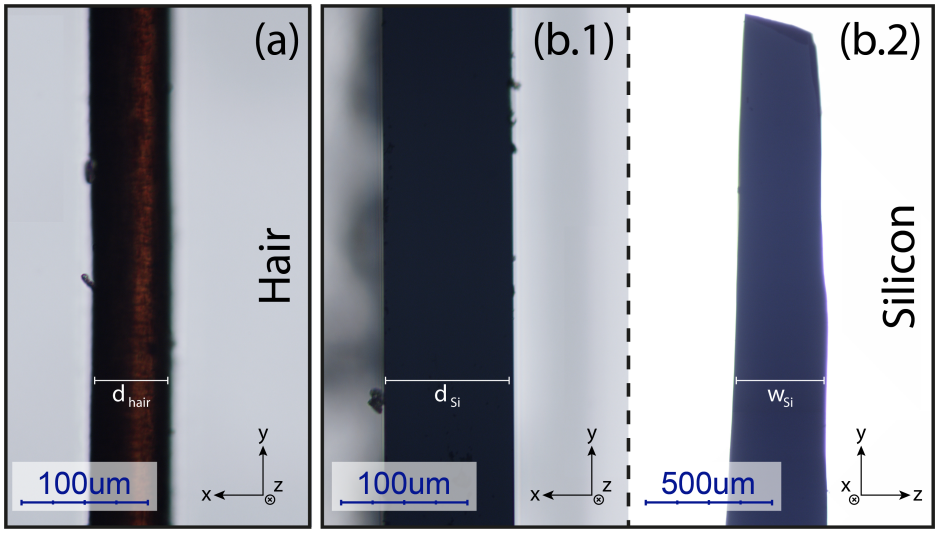

Figure 3.3: Microscope picture of samples used. (a) picture of a human hair, from which we extract a diameter $d_{\text{hair}} = 0.062 \pm 0.002$ mm. (b) is separated in a picture from the side (b.1) and from the top (b.2) of the silicon bar. From such microscopy pictures we extract a thickness $d_{\text{Si}} = 0.103 \pm 0.003$ mm and a width $w_{\text{Si}} = 0.440 \pm 0.002$ mm. Only one sample of each kind was used, thus one human hair and one silicon bar.

term $F_{1,2}^{\text{cross}}$ from the following observables

$$F_{1,2}^{\text{cross}} = F_{1,2} - F_{1,1} - F_2^{\text{scat}}. \tag{3.3}$$

Here, we assume $F_1^{\text{scat}} \ll F_1^{\text{in}}$ and thus also $F_1^{\text{scat}}, F_{1,2}^{\text{scat}} \approx 0$, which is reasonable because the measurement direction is equal to the incident direction ($\hat{k}_{\text{in},1} = \hat{k}_{\text{det}}$), and since coherent beams are generally much brighter than scattered beams [20]. Using this reasonable assumption, we extract the self-extinction F_1^{ext} in a similar way

$$F_1^{\text{ext}} = F_{1,1} - F_1^{\text{in}}. \tag{3.4}$$

We use F_1^{ext} for normalization, as we want to know how the total extinction changes due to these interferences with respect to the case when only self-extinction is considered. Thus, we obtain the normalized total extinction

$$F^{\text{TE}} = \frac{F_{1,2}^{\text{cross}}}{F_1^{\text{ext}}}. \tag{3.5}$$

It is this observable F^{TE} that reveals the desired mutual extinction and mutual transparency.

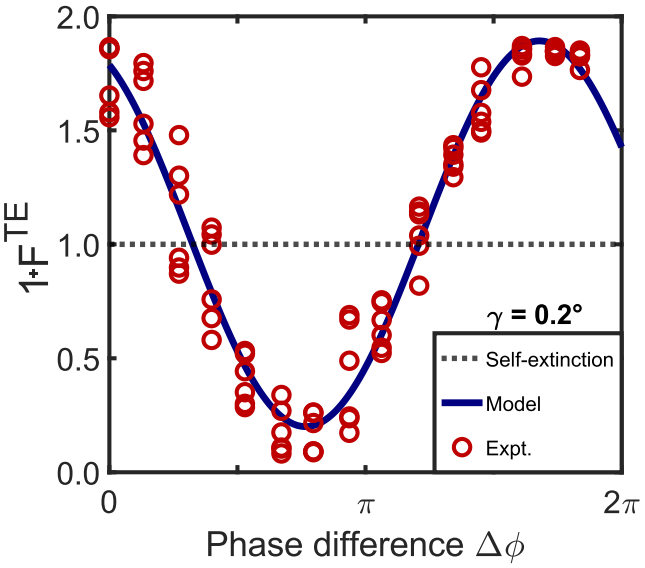

Figure 3.4: Total extinction F^{TE} versus phase difference $\Delta\phi$ for an angle $\gamma = 0.20^o$ between the two beams for the human hair. Dark red circles are experimental data while the solid blue line is a fit to the exact mutual scattering model. The dotted line is the case of no mutual scattering. The phase difference is extracted from the retardance of the phase retarder.

3.3 Experimental methods

To detect mutual scattering, we built the experimental setup shown in Fig. 3.2. A He-Ne laser ($\lambda = 632.8$ nm) is used as a source. The laser beam is split into two incoming beams, beam 1 and beam 2, in a modified Mach-Zehnder configuration with a slight and controllable skewness at the outgoing beamsplitter BS3. Before reaching BS3, both beams pass through linear polarizers (LPVIS050 Thorlabs), and beam 2 passes through a liquid crystal phase retarder (LCC1413-B Thorlabs), which we use to control the phase difference $\Delta\phi$. By carefully moving and rotating mirror M2, we control the angle γ between the two beams. At a fixed location downstream of BS3, where the sample is located, the two beams cross at an angle γ. We use a CCD camera to detect beam 1 by integrating over the illuminated pixels, and a photodiode at the beginning of the optical circuit to correct for laser fluctuations. Both the angle variation and the phase variations are made in beam 2, whereas only beam 1 is detected with the CCD camera. At every angle γ, the phase $\Delta\phi$ was varied from 0 to 2π and back. For each phase, we took three consecutive exposures with the CCD camera to average over environmental noise.

We position the sample in the intersection plane of the two beams, as shown in the inset of Fig. 3.2. All samples we study have a bar-like geometry, meaning that

one dimension is much larger than the other two. We define the active area as the overlapping area of the two beams in the illuminated face of the sample. Thus, in the x-direction the dimension of the active area is given by the geometry of the sample, and in the y-direction the dimension is given by the beam diameter.

We study two different samples: The first sample is a human hair, which has a natural near-cylindrical shape with a diameter of $d_{\text{hair}} = 0.062 \pm 0.002$ mm as observed with a microscope (see Fig. 3.3(a)). The scattering properties of human hair are of special interest for the 3D animation industry to obtain a realistic simulation of hair in animated characters [116]. Furthermore, single human hair fibers are widely used to teach light diffraction in undergraduate and secondary education, approximating it to the inverse of a single slit [117]. The second sample is a thin silicon bar cleaved from a standard Complementary Metal Oxide Semiconductor (CMOS) wafer, with a thickness $d_{\text{Si}} = 0.103 \pm 0.003$ mm and a width $w_{\text{Si}} = 0.440 \pm 0.002$ mm (see Fig. 3.3(b)). The scattering properties of silicon are highly relevant for the semiconductor industry. In particular, detecting the shape and position of silicon structures is a highly demanded metrology measurement, mostly done by optics. To limit the complexity, we use samples that are translational invariant along the y-axis. To accomplish this, the silicon bar is illuminated from the side and not from the top.

3.4 Experimental results

First, let us consider the case where the angle γ is fixed. In Fig. 3.4, we show the normalized total extinction of a human hair while changing the phase ϕ. The angle between incoming beams is $\gamma = 0.2^o$. We see that the extinction follows a cosine-like trend, as expected from the prediction [69] (see Appendix 3.7.1). We also see that at the maximum the extinction nearly doubles, while for the minimum the extinction is close to zero, so that the object appears nearly fully transparent. In theory, the total extinction is minimum for $\Delta\phi = 0$ and maximum for $\Delta\phi = \pi$. We see that the experimental data are shifted in phase, which arises from uncertainty in the true-zero phase (see Appendix 3.7.2). This effect is due to changes in the optical path of beam 2 when moving and rotating mirror M2 (see Fig. 3.2). Still, we see that the periodicity of the observed cosine-like curve agrees well with theory, and thus this phase offset does not affect the final results.

In Fig. 3.5, we plot the total extinction of the human hair versus angle γ. The symbols correspond to the maximum and minimum extinctions obtained as a function of the phase at each angle (see Fig. 3.4). The observed maximum and minimum extinctions show an oscillatory behavior versus incident angle γ, typical of interference between scattered and coherent beams. Our analytical model is shown to be in good agreement with the experimental data. This model uses the scattering amplitude of an impenetrable flat surface (see Appendix 3.7.1) as an approximation to obtain the variations in the forward scattering due to mutual scattering. Our model has no adjustable parameter since the width of the sample a_{mic} is obtained by microscopy inspection. We see that the data follows a sinc trend similar to the model, with a slight shift in angle discussed in the next section.

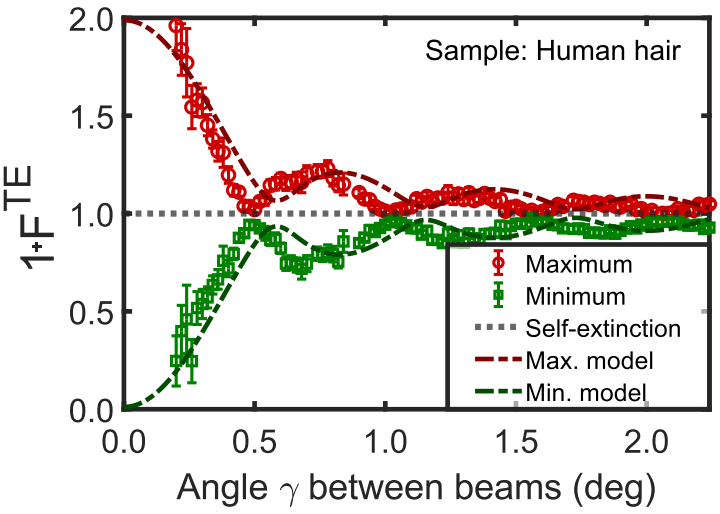

Figure 3.5: Total extinction versus angle γ between beams for a human hair. The red circles (green squares) correspond to the maximum (minimum) extinction obtained from phase variations (see Fig. 3.4). The dashed lines are our analytical model with no adjustable parameter (see Appendix 3.7.1).

For the silicon bar, the total extinction against angle is shown in Fig. 3.6. The data has a similar sinc shape as the human hair, but here the frequency of the interference fringes is higher. Furthermore, the analytical approximation agrees even better with the experimental data than for the hair sample.

3.5 Discussion

3.5.1 Observations and model

In both the phase and angle variation experiments, we obtain the trend predicted by the mutual scattering theory [69], namely a cosine-like trend in the phase variation experiments and a sinc-like trend in the angle variation experiments. We see that using our analytical model, we obtain a description of the mutual scattering, which gives a faithful interpretation of the observations.

In Fig. 3.4, we see that the modulation of the total extinction is close to the full range from 0 to 2. To discern how large this modulation is compared with the total signal of the beam, we obtained that in the case of the human hair, the extinguished light amounts to about 15.4% of the incoming light. With mutual scattering, the extinguished light varies from approximately 2.5% to 24%. This is close to the maximum modulation predicted by theory, which varies from 0% to 30.8%.

In Fig. 3.5, we observe that the model predicts a slightly lower frequency

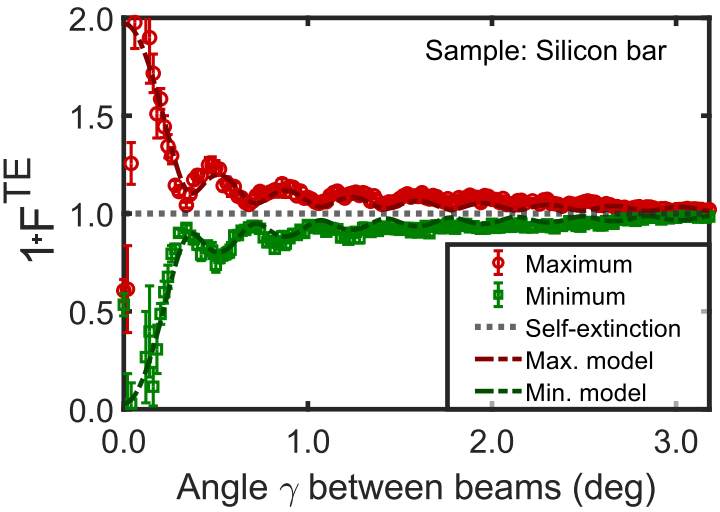

Figure 3.6: Total extinction versus angle γ between beams for a silicon bar. The red circles (green squares) correspond to the maximum (minimum) extinction obtained from phase variations. The dashed lines are our analytical model with no adjustable parameter.

of fringes than measured, meaning that the nodes of the model are located at larger angles than the ones from the experimental data. The curve shapes are in excellent overall agreement. The small deviations emerge from the fact that the human hair has a cylindrical geometry. Thus, the sample thickness varies with the lateral position within the incident beams. The thickness variation is not addressed in the model, where we assumed a flat impenetrable surface. We quantify this deviation using the width of the sample a as a single adjustable parameter in our model (see Eq. 3.7), and compare the estimated value a_{mod} with the width of the sample used originally as input for the model, which we extracted from optical microscopy inspection a_{mic}. In Table 3.1 we see from this comparison that the adjusted width does not match with the independent observation.

Sample	a_{mod} (mm)	a_{mic} (mm)
Hair	0.072 ± 0.001	0.062 ± 0.002
Silicon	0.105 ± 0.001	0.103 ± 0.003

Table 3.1: Table of sample dimension extracted from the model (a_{mod}), and extracted from optical microscopy inspection (a_{mic}). The error range of the model is due to the dispersion of the experimental data, while the error range of the optical microscopy inspection is due to microscope resolution and reproducibility.

In contrast, for the silicon sample, which has a box-like geometry, a_{mod} and

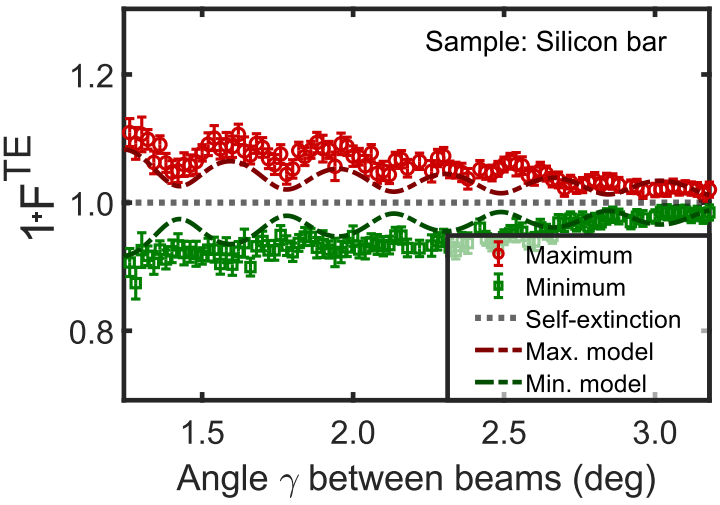

Figure 3.7: Total extinction versus angle γ between beams for a silicon bar. Zoom in for large angles from Fig. 3.6. The dashed lines are our analytical model with no adjustable parameter.

a_{mic} are equal within the error bars. We see in Fig. 3.6 that for small γ the analytical model describes the silicon data accurately. This can lead one to think that this approximation describes the results completely, but this is not the case. In Fig. 3.7, we zoom in on the silicon results to observe in detail the deviation for angles between $\gamma = 2$ to 3^o. We see that for $\gamma > 2.0^o$ the trend followed by the experimental data has some discrepancies with the model: in the beginning, the nodes start to shift, and finally, the shape of the sinc curve is completely lost. Importantly, at all these angles the measured phase dependencies keep following a cosine-like curve as in Fig. 3.4, and the signals are significantly larger than the errors. We extend our analytical model by also taking into account the beam divergence of the laser using a convolution over the Gaussian beam profile. Nevertheless, we see that the averaging effect caused by divergence does not explain this deviation.

The apparent random shape of the total extinction at larger angles is probably an indication that we are entering the speckle regime where the variations in the extinction do not depend only on the dimensions of the sample, but also on the detailed spatial distribution of the scatterers inside the material or the surface roughness. In the speckle regime, the depth of the sample also plays an important role. For the case of the silicon bar, when changing the angle, the path length inside the sample also changes, which modifies the scattering amplitude in that direction. This is not accounted for in the model, where we assume a flat impenetrable surface.

When the sample is fully opaque and its size is much larger than the wave-

length, the *angular dependence* of the scattering amplitudes, and thus of the mutual scattering, will follow the well-known Kirchhoff integral [85], which we used to derive our model. In the situation where the sample is not fully opaque, as in our experiments, the angular dependence of the scattering amplitudes will become speckle-like, starting at the large angles of γ. From theory [69], we expect the speckle regime to extend to very large angles, including for angles larger than 90^o.

If the sample has a mean free path l much larger than its size ($l \gg L$), the angular speckle will set out in the immediate vicinity of the first zero-crossing, which itself is determined by the geometry of the sample. The more transparent the sample is, the more prominent the speckle will be. But when averaging over many realizations, the result of the Kirchhoff integral is recovered.

3.5.2 Applications

Mutual scattering was discovered when explaining the apparent violation of energy conservation when simulating WFS. For that reason, an important application of mutual scattering is in WFS. It is well known that the information in a scattering material is not lost but *scrambled*. WFS is a common way to extract this information, yet many open questions remain regarding how to extract and use this information. We think that mutual scattering can contribute to the discussion on open channels in complex media [106] and in the simultaneous optimization of transmitted and reflected intensity, both currently studied with WFS. Furthermore, we think that wavefront modulation can be used to design a non-diffracting beam shape, such as Bessel beams [118, 119], which can be used in mutual scattering in extended samples.

Mutual scattering can have applications in the field of ultraviolet communications for non-line-of-sight links [120], which is based on light scattering in the atmosphere. The scattered light can be enhanced or reduced if the transmitter uses two beams that cross in the active area. Furthermore, mutual transparency can be used to reduce losses related to light attenuation in the atmosphere. Deeper research is needed to translate the results presented in this chapter into a more practical system.

Mutual scattering is a promising tool for inferring the shape and size of an object, including free-form samples, by utilizing the observed interference fringes [121]. Moreover, the speckle regime of mutual scattering exhibits high sensitivity to the positions of individual particles within the material, making it possible to sense the position of a nano-particle amidst a *sea* of similar nanoparticles [71].

Diffusion Wave Spectroscopy (DWS) has become a popular technique for studying time-dependent optical properties of complex materials and for bio-imaging [122–124]. Unfortunately, DWS is not well suited for samples that absorb light rather than scatter. To study the motion of scattering particles, one currently uses techniques such as Dynamic Light Scattering (DLS) [125], which is also not suited for samples that absorb rather than scatter. In contrast, Mutual scattering is suitable for samples that scatter or absorb (or both), as long as there

is some detectable intensity left of the incoming beam. We envisage for those samples that their dynamics can be probed by using a time-dependent mutual scattering technique.

3.6 Conclusions

We have measured the total extinction of two beams crossing through a scattering object, namely a human hair and a silicon bar. Upon varying the relative angle and phase between the beams, we measured the variations in the total extinction. When the angle is close to zero, we control the extinction in such a way that the scattering object is almost twice as opaque or nearly fully transparent to the beams. Alternatively, if the angle is larger we enter into the speckle regime where fluctuations of the mutual scattering depend on the precise shape and distribution of the scatterers distribution in the sample.

Our results are well described with the recently presented mutual scattering theory [69], turning this experiment into the confirmation of this effect. We used an analytical approximation of the scattering amplitude applicable when the sample is opaque. We have seen that this approximation is a good model for box-like geometries and small angles, but at the same time, we see that mutual scattering cannot faithfully be interpreted with such a simple approximation of the scattering amplitude, for transparent samples.

The data from our experiments are available in the publicly available Zenodo database [126].

3.7 Appendices

3.7.1 Model for angular dependence

In Ref. [69], we have calculated and described the scattering amplitudes of both a collection of point dipoles and a flat and opaque object. Here, we compare our experimental results with the latter, where the scattering amplitude is derived as (see Eq. 8 of Ref. [69])

$$f = \frac{iab}{\lambda}\mathrm{sinc}(\alpha)\,\mathrm{sinc}(\beta) \tag{3.6}$$

where λ is the wavelength in vacuum, $\alpha \equiv \frac{a}{2}(\cos\theta_{x,\mathrm{out}} - \cos\theta_{x,\mathrm{in}})$, $\beta \equiv \frac{b}{2}(\cos\theta_{y,\mathrm{out}} - \cos\theta_{y,\mathrm{in}})$, $\theta_{x,\mathrm{in}}$ and $\theta_{y,\mathrm{in}}$ are the angles of the incident waves with respect to the x and y-axes, $\theta_{x,\mathrm{out}}$ and $\theta_{y,\mathrm{out}}$ are the angles of the outgoing waves with respect to the x and y-axes, and a and b are the dimensions of the sample in the x and y-directions, respectively.

The scattering amplitude f is simplified if we consider both incident waves to be in the xz-plane. Consequently, the power flux F is simplified to

$$F_{\mathrm{model}} = \mathrm{sinc}\left(\frac{2\pi a}{\lambda}\sin\frac{\gamma}{2}\right), \tag{3.7}$$

For the human hair, the dimension a is defined as the diameter of the hair ($a = d_{\text{hair}}$), and for the silicon bar it is defined as the thickness of the bar ($a = d_{\text{Si}}$).

When the sample is absorbing, as in the case of our experiments, the amplitude of F is strongly affected by the absorption coefficient of the sample. This is not accounted for in Eq. 3.7, where the amplitude is 1. Nevertheless, when normalizing with the self-extinction, as it is done in Eq. 3.5, this effect is canceled out.

To take the divergence Θ of the laser beam into account, we implemented a convolution between F_{model} and the angular momentum profile of a Gaussian beam $U(\theta)$ given by [127]

$$U(\theta) = \exp\left(-\tan^2(\theta)/\tan^2(\Theta)\right). \tag{3.8}$$

F_{model} includes both positive and negative values, meaning both mutual extinction and mutual transparency. To separate between both cases, we take $F_{max} = 1 + |F_{model}|$ as the maximum curve and $F_{min} = 1 - |F_{model}|$ as the minimum curve, which corresponds, respectively, to the dashed red curve and the dashed green curve in Figures 3.5, 3.6, and 3.7.

3.7.2 Model for phase dependence

When the angle γ is fixed, mutual scattering fluctuates following a cosine function if we change the relative phase $\Delta\phi$. If γ is outside the speckle regime, the total extinction is minimum for $\Delta\phi = 0$ and maximum for $\Delta\phi = \pi$. Differently, if γ is inside the speckle regime, deviations in the position of maximum total extinction are a reflection of the complex part of the scattering amplitude f.

In our current experiment, the path length of beam 2 changes when we change the angle, meaning is not possible to retrieve the true phase for the maximum total extinction. Instead, to compare our experimental results with the model we use

$$F_{\text{fit}}^{\text{TE}} = 1 + c_1 \cdot \cos(c_2\Delta\phi - c_3\pi) + c_4, \tag{3.9}$$

where $c_1 = 0.8461$, $c_2 = 1.0954$, $c_3 = 0.7800$, and $c_4 = 0.0464$ are adjustable parameters. We can extract from here $\Delta\phi_{\text{off}} = 0.78\pi$ as the phase offset in the measurements.

Chapter 4

How to extract the complex scattering amplitude of any material using mutual scattering

We propose a novel experimental technique for optical characterization that utilizes mutual scattering. This effect arises when multiple beams intersect within a finite scattering sample, resulting in cross-interference between the incoming and scattered waves. By measuring mutual scattering, we determine the complex scattering amplitude f of the sample, which provides information on its scattering properties by linking incoming and outgoing waves from any arbitrary direction. We present our findings on mutual scattering for four distinct samples: a polystyrene sphere, a single black human hair, a strip of pultruded carbon, and a block of ZnO_2. Our measurements exhibit qualitative agreement with Mie scattering calculations for samples where the model is applicable. Deviations from the model indicate the complexity of the samples, both in terms of their geometrical structure and scattering properties. Our results offer new insights into mutual scattering and have significant implications for future applications of optical characterization in fields such as metrology, microscopy, and nanofabrication.

4.1 Introduction

The interaction between light and matter has been studied since the early days of optics, a field concerned with the properties of light and its behavior as it interacts with different media. Scattering is a fundamental concept in optics, describing the generation of scattered waves as light enters a complex medium and interacts with its scatterers. The theory of scattering is a mature, unifying branch of theoretical physics [9, 20, 128], and measuring scattered light of an object is a vast source of information on its optical properties [97]. Thus, it is not a surprise to see such measurements being used for characterization in a wide range of applications, with techniques such as dynamic light scattering [124, 129], optical coherent tomography [130–132], diffusion tomography [133], wavefront shaping [43, 44, 63, 72], transmission matrix measurements [28, 29, 67, 94], and many more.

In many studies of light scattering, the sample under study is *extended*, meaning the area of the incident light beam is much smaller than the size of the sample. This type of measurement induces a relevant yet commonly overlooked limitation: all incoming light is scattered, and the incoming wave is not present at the detector plane in transmission [53, 54, 73, 128]. However, when the sample is *finite*, *i.e.*, smaller than the area of the incident light beam, the incoming wave is always present at the detector plane when measuring in transmission, and this limitation is not present[1].

An advantage of studying finite samples is the ability to measure light extinction. Light extinction is the combination of both scattering and absorption and refers to the decrease of incoming light by passing through an object [112]. This process is fully described by interferences between the incoming wave still present in transmission and the scattered waves in the forward direction. It is common to use waveguides or extended slabs of opaque media in light scattering experiments. But in those samples, the incoming wave is absent in the detector plane, which means it is **imposible** to measure light extinction in such samples.

We recently discovered [69] that if multiple incoming beams cross in a finite sample, there is a cross-interference between the incoming coherent wave of one beam and the scattered wave of another. We call this cross interference *mutual scattering*. Fig. 4.1 illustrates this process in the case with two incident beams; the incoming purple wave interferes with the scattered orange waves in the direction of the detector. Furthermore, we discovered that mutual scattering modulates the total extinction of the sample. The modulation of the total extinction depends on the relative angle and phase between the incoming waves and on the scattering amplitude f of the sample. Thus, by changing the angle and phase of the incoming waves, we tune the extinction of the sample, making it appear more transparent (less extinction) or more opaque (more extinction). We demonstrated this modulation experimentally in a recent study [70], see Chapter 3.

Alternatively, by measuring the modulation of the total extinction, we can

[1] This is also the case for non-opaque media, *e.g.*, optical attenuators.

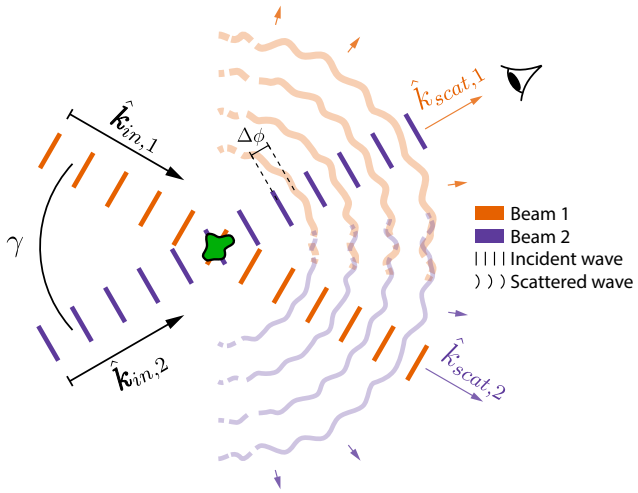

Figure 4.1: Schematic of two-wave mutual scattering: $N = 2$ beams with wavevectors $\hat{k}_{\mathrm{in},1}$ and $\hat{k}_{\mathrm{in},2}$ and mutual angle γ are incident onto a scattering sample. The scattered waves are shown as curved wobbly wavefronts to emphasize that they are present at all outgoing directions (with wavevectors $\hat{k}_{\mathrm{scat},1}$ and $\hat{k}_{\mathrm{scat},2}$). When $\hat{k}_{\mathrm{scat},1} = \hat{k}_{\mathrm{in},2}$ and $\hat{k}_{\mathrm{scat},2} = \hat{k}_{\mathrm{in},1}$, the scattered wave interfere with the incoming coherent beam. $\Delta\phi$ refers to the phase difference between two incoming waves. The arrow colors distinguish the scattered waves and do not represent different wavelengths.

extract the scattering amplitude f. The scattering amplitude, similar to a transmission matrix, encapsulates all the scattering properties of the sample [19, 73, 112, 134]. The parameter f dictates the relation of an incoming wave with the resulting scattered wave at any given angle. To obtain the complex properties of the scattering amplitude f and thus characterize the object, we need to extract both amplitude and phase information from the mutual scattering measurements. Since light extinction consists of both absorption and scattering components, mutual scattering provides a significant benefit as it enables the characterization of strongly absorbing samples.

In this chapter, we present an experimental method and protocol to measure mutual scattering and thus extract the scattering amplitude of a finite sample of any material. We do this by modulating two incident beams with a digital micromirror device (DMD) and measuring the transmitted light. This is an improvement from our previous experiments [70], where we used mechanical stages and phase retarders instead of a DMD. A DMD is significantly more stable and robust than mechanical stages and liquid-crystal phase retarders. Using a DMD in our experimental method allows for both amplitude and phase extraction, while our previous experiment had only access to the amplitude data. Here, we show the measurements of 4 samples with different optical properties: a polystyrene sphere, a single black human hair, a strip of pultruded carbon, and a block of ZnO_2. For the polystyrene sphere and the single human hair, we compare our

measurements with Mie calculations.

4.2 Experimental methods

To measure mutual scattering, we built the experimental setup shown in Fig. 4.2. We use a He-Ne laser (Hughes 3225H-PC, 5mW, $\lambda = 632.8$ nm) as a source and a $\times 15$ telescope to enlarge the beam area. We control the angle and phase of the incoming beams using a digital micromirror device (DMD, Vialux VX4100), where the two incoming beams are generated using two active areas in the DMD. An active area is a collection of adjacent DMD pixels (in this case, 72 pixels) that are simultaneously activated, surrounded by inactive pixels. We control the phase $\Delta\phi$ of the beams using the Lee holography technique [79, 80]. We implement the spatial filter needed for the Lee holography using lenses L3 and L4 and an iris in between. The two beams are focused into the sample using lens L5 in such a way that the beams cross, forming an angle γ. We change the angle γ by changing the position of the active areas of the DMD, thus making the beams closer or further apart before reaching lens L5 (see Fig. 4.5). We use two charge-coupled device cameras (CCD, Stingray F-125) to detect the flux F integrating over the illuminated pixels. Camera CCD1 measures the flux of the two incoming beams after passing through the sample, whereas camera CCD2 is placed at the focal distance of L5, and its measurement corresponds to the wavefront pattern at the sample position. We use camera CCD1 to measure mutual scattering, while camera CCD2 is used for calibration and characterization. Additionally, we place a Powermeter (not shown) at the beginning of the optical circuit to correct for laser fluctuations.

We measure 280 positions of γ in total from $0°$ to $2.8°$. For each angle γ, we vary the phase difference $\Delta\phi$ from 0 to 2π with 30 steps in between. To have better statistics, we iterate the phase scanning three times for each angle.

We extract the normalized mutual scattering component F_{MS} following the same procedure described in our previous work [70], as

$$F_{\mathrm{MS}} = F_{1,2}^{\mathrm{ws}} - F_{1}^{\mathrm{ws}} - F_{2}^{\mathrm{ws}} - \left(F_{1,2}^{\mathrm{ns}} - F_{1}^{\mathrm{ns}} - F_{2}^{\mathrm{ns}}\right), \tag{4.1}$$

where the sub-index represents which beam is activated (only beam 1, only beam 2, or both 1,2), and the upper-index states if we measure with the sample present (ws) or when there is no sample present (ns). F_{MS} represents the modulation of the extinction of light due to mutual scattering. We normalize this component with the total extinction of a single beam. If $F_{\mathrm{MS}} = 0$, the extinction has the same value as in a single-beam experiment; if $F_{\mathrm{MS}} = 1$, the extinction is twice as large, making the object twice as opaque; and if $F_{\mathrm{MS}} = -1$, the extinction is canceled out, making the object fully transparent.

We measure F_{MS} for 4 different samples: a polystyrene sphere (Thermo Scientific 7000 Series, 7550A 55 μm), a single black human hair, a strip of pultruded carbon, and a block of ZnO_2. With the exception of the single human hair, all

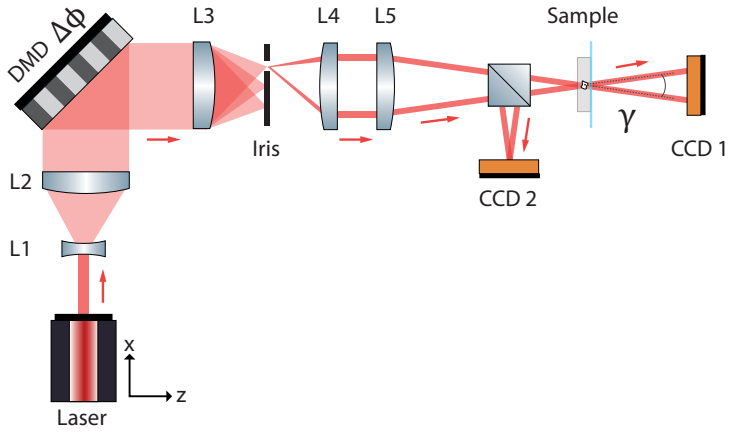

Figure 4.2: Diagram of the experimental setup. The two incoming beams are generated using active areas in the digital micromirror device, which also sets the phase difference between the beams $\Delta\phi$. Lenses L3 and L5 and the iris are used for the holographic filter needed for the Lee holography technique, which allows us to control the phase of the wavefront. The two beams are focused into the sample by lens L5 forming an angle γ, and then collected by camera CCD1. A beamsplitter is placed in front of the sample such that the reflected focus arrives on camera CCD2.

the samples are embedded in PDMS (Dowsil SYLGARD 184 & included curing agent). We prepare the samples with two layers of PDMS, as shown in Fig. 4.3. We first prepare a PDMS layer in a Petri dish and use a vacuum pump to remove the microbubbles in the PDMS. Once the PDMS is cured, we place the sample on top of it and fill a second layer following the same procedure. When the second layer is ready, we cut the area where the sample is embedded and glue it to a microscope glass slide. For all steps, the proportion between PDMS and the curing agent is 10:1. Meanwhile, we glue both ends of the single hair to a microscope glass slide such that it is suspended in the air.

A microscope picture of every sample already embedded in PDMS is presented in Fig. 4.4. Note that due to a microscope artifact, the ZnO_2 in Fig. 4.4d looks as opaque as the pultruded carbon in Fig. 4.4c. To better showcase the difference in optical properties, Fig. 4.4e shows a picture of the bulk materials.

While the sphere and the hair already have the desired dimensions ($2r_{\text{sphere}} = 59\ \mu$m and $2r_{\text{hair}} = 92\ \mu$m), the pultruded carbon and the ZnO_2 need to be manually prepared. The pultruded carbon is prepared from a commercially-available manufacturer (van Dijk Pultrusion Products DPP) with dimensions $1000 \times 10 \times 0.1$ mm, and it is manually cut to a cuboid with estimated dimensions $140 \times 54 \times 10\ \mu$m. Finally, the block of ZnO_2 is prepared using ZnO_2 particles (Sigma-Aldrich 544906 Zinc Oxide nanopowder) suspended in PDMS, following the same procedure discussed above, with a particle concentration of 10%. Then, the sample is manually cut into a cuboid with an estimated side size of 64 μm.

We position all the samples at the crossing point of the two incoming beams,

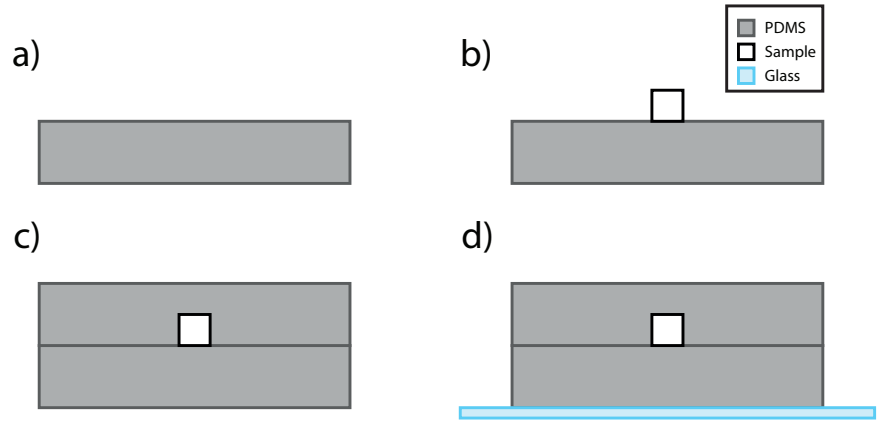

Figure 4.3: Illustration of steps for sample preparation. a) in a Petri dish, we prepare a layer of PDMS (grey), b) once the PDMS is cured, we place the sample (white) on top of it, c) we then cover the sample with a new layer of PDMS, d) once the second layer is cured, we cut the area where the sample is and glue it on top of a microscope glass slide.

i.e., at the focal distance of L5. All the samples have a size smaller than the beam waist at the focus. Thus, they do not block all the light, and the incoming beam is still present at the detector.

4.3 Experimental calibration and phase acquisition

A crucial aspect of the experiment is the calibration of the incident beams. Ideally, when using a plano-convex lens, all the rays cross at the focal point. Hence, two incident beams are sure to cross on the sample. Unfortunately, any misalignment or aberration will distort the focus. In addition, we realized the DMD itself causes strong aberrations in the wavefront (see Chapter 2). This is most probably because the micro-mirrors are not perfectly flat, and any curvature or imperfection adds up to the final wavefront.

To overcome this issue, we implement the correction shown in Ref. [84]. The correction is based on optimizing the intensity pattern at the focus by adding a phase mask using a pattern generated by Zernike polynomials. This is based on the assumption that common aberrations have a pattern described by Zernike polynomials [85]. In Ref. [84], they iterate the coefficients of the polynomials to maximize the intensity at the focal point. For our case, we found that instead of maximizing intensity, we obtain a better correction by calculating beforehand the expected intensity distribution at the focus and then maximizing the 2D correlation between the measurements and the calculated pattern. For this calibration, we used the camera CCD2 (see Fig. 4.2). Having a beamsplitter adds

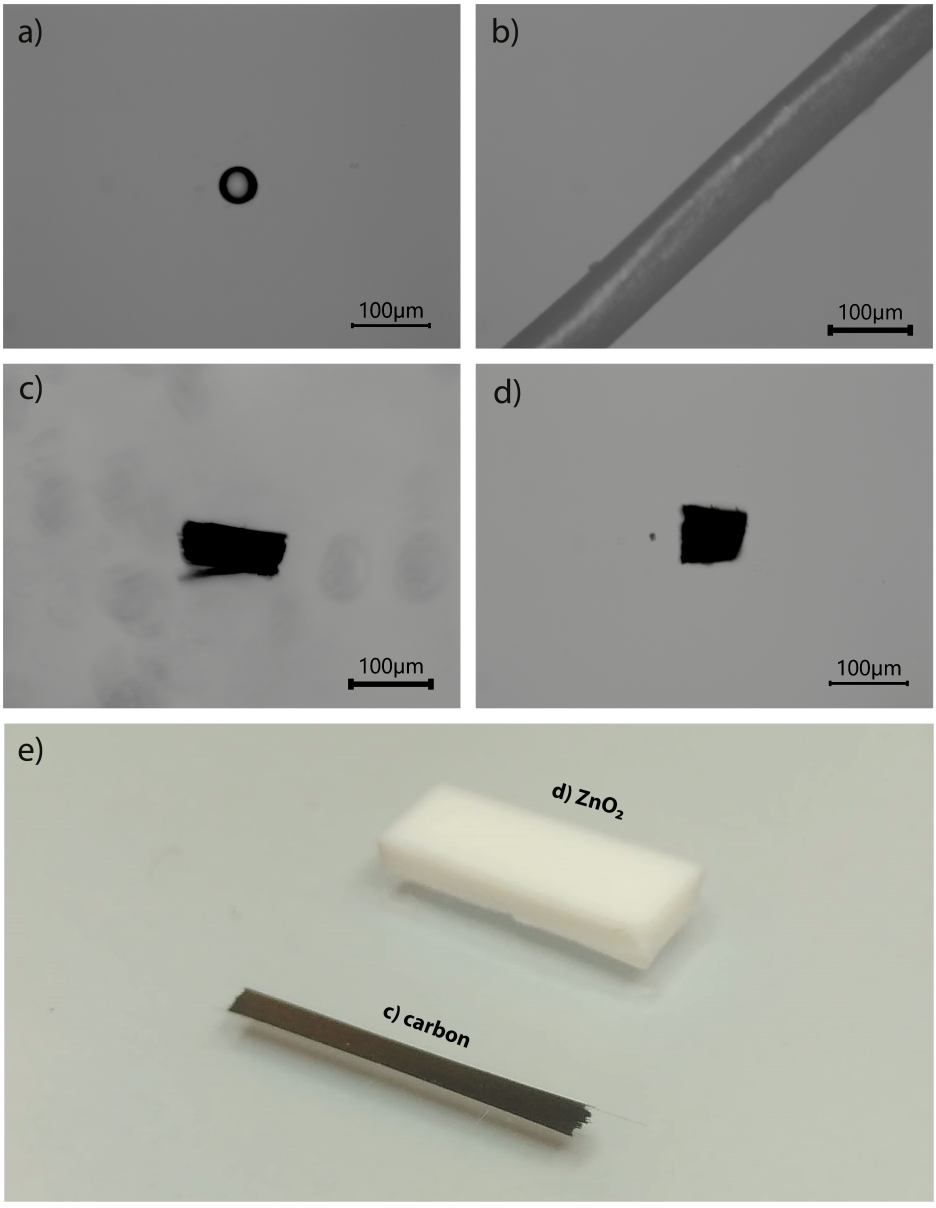

Figure 4.4: Microscope picture of samples used. a) A polystyrene sphere, b) a single black human hair, c) a pultruded carbon strip, and d) a ZnO_2 block. All pictures are at the end of the fabrication process, meaning all the samples except the hair are embedded in two stacked layers of PDMS. e) Picture of the macroscopic raw material for the pultruded carbon sample and the ZnO_2 sample. Both samples need to be manually cut to get the desired geometry.

the possibility of calibrating the setup without disturbing the sample.

In Fig. 4.5, we show an example of the phase masks used for different angles. We characterize our experiment by running the optimization we described above for every active area separately. In the experiments, only two areas are simultaneously activated for a given angle. For the results that we show in this chapter, we keep the center area (highlighted with a red circle) constantly activated, and we only vary the second beam. We call this the *asymmetric case*. Still, our experimental setup also allows for the *symmetric case*, where we vary both beams simultaneously. In our system, it is also possible to vary the position of the active areas not only in one line but at any angle by characterizing the whole DMD. Note that here we only show a set of selected angles. In reality, we have almost 600 different positions along the y-axis of the DMD.

It is very important to highlight the difference between the phase mask for the calibration of the experiments, which we measure and characterize using camera CCD2, and the phase information extracted from our experiments, which we obtain by controlling the incident beams onto the sample. When varying the phase difference between the two beams $\Delta\phi$ at a fixed angle, F_{MS} follows a sinusoidal curve, as illustrated in Fig. 4.6. We extract the amplitude and phase of the modulation of F_{MS} for each angle γ. We do this by taking the Fourier transform of the raw data and filtering the point with frequency $f = 1/2\pi$. This gives us the cosine-like behavior we expect from theory. The optimized amplitude of the filtered data is extracted as the amplitude of F_{MS}. Conversely, the phase information of the mutual scattering is the phase difference at which F_{MS} is maximized.

We treat the error of the estimation of amplitude and phase separately. We consider the error range of our amplitude estimation to be the average difference between the filtered curve (solid black line at Fig. 4.6) and the data (symbols at Fig. 4.6), similar to the residual of a fitting process. Meanwhile, the error of the phase estimation is done through an iterative process. We do this by adding phase offsets to the experimental data and calculating the amplitude error for every new phase offset. The offset where the amplitude error is *twice* (chosen based on experience) the original amplitude error, is chosen as the error range of our phase estimation (see Chapter 2).

If we reach an offset equal to 2π and the amplitude error is still not doubled, we consider the phase to be *undefined*, *i.e.*, the data does not have a cosine-like shape, and we are not able to estimate the phase.

The most challenging step to extract the phase information is to calibrate the phase difference $\Delta\phi$ when changing the angle. This is because any change in path length generated by changing the angle will add a dephase. For example, given angle γ_1 with the set phase difference $\Delta\phi_{\gamma_1}$, changing to angle γ_2 without adapting the phase difference, aberration, misalignment, or medium induces the dephase such that $\Delta\phi_{\gamma_2} \neq \Delta\phi_{\gamma_1}$.

Calibrations of this induced dephase turn out to be tremendously difficult. We initially calibrate $\Delta\phi$ and γ by measuring the interference fringes at CCD2. Besides technical limitations, such as noise, alignment, and camera resolution, we found that the camera cannot obtain the exact phase and angle information

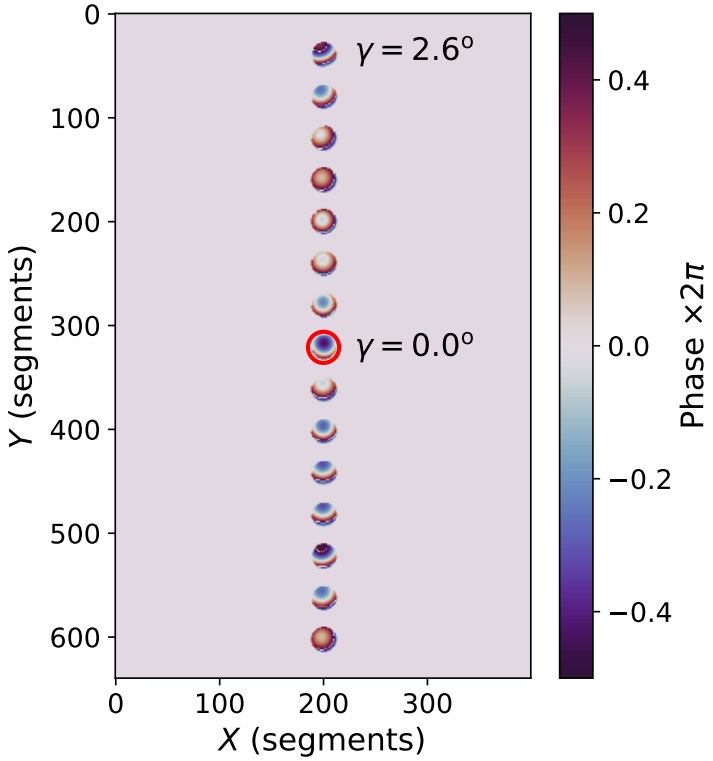

Figure 4.5: Phase masks in DMD for selected angles. We can control the phase of each segment of the mask from 0 to 2π. Each circle corresponds to a different incident angle at the sample. The red circle highlights the central circle, which is always activated. All the pixels outside the circles have phase *and amplitude* 0. The color bar is circular (the color at 1 is the same as the color at -1) to account for the periodicity of the phase.

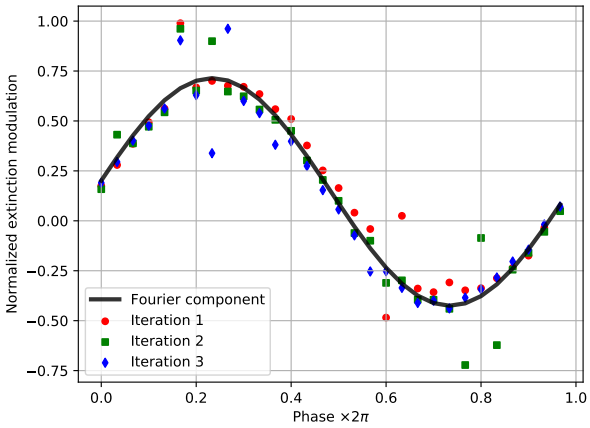

Figure 4.6: Total extinction against phase difference between beams for a fixed angle $\gamma = 0.74°$. Circle symbols are experimental data, and the different colors represent the different iterations of the measurements. The solid black line shows the extracted cosine component using Fourier filtering.

because the detector chip is covered by a protective glass [135], while the samples are embedded in PDMS. These two media have different effects on the phase and angle of the incoming light. Furthermore, to calibrate $\Delta\phi$ and γ we need to estimate multiple parameters such as the depth of the sample in the medium, the orientation of the sample inside the medium, the roughness of the surface of the medium, any tilt of both cameras, any misalignment, etc. The estimation has so many degrees of freedom that it is not far from an educated guess, making it also more susceptible to confirmation bias.

There is a glimpse of hope when looking at the raw data of the phase information extracted when measuring mutual scattering. Fig. 4.7 illustrates the steps we currently follow to calibrate the phase information. Fig. 4.7a shows the raw phase data for the dielectric sphere. Because of the periodicity of the phase, we know that $\phi = 2\pi + \phi$. Fig. 4.7b shows the same raw data multiple times with jumps of 2π. We select the 2π jump such that yields a continuous curve, shown in Fig. 4.7c. We see that there is a slow decaying envelope pattern in the phase, presumably coming from the dephases explained above, as it has a weak dependence on the angle (*i.e.*, slow variations when changing γ) and larger than the phase information of the mutual scattering that we expect from theory for any sample. Thus, it is possible to reduce the effect of the envelope pattern by making a linear regression and subtracting it from the data in order to obtain the phase information shown in Fig. 4.7d. This allows us to discuss the small variations in the data that have a strong dependence on the angle (*i.e.*, fast variations when changing γ), which we attribute to the sample itself. We believe this correction is enough to get relevant information from the measured samples. We

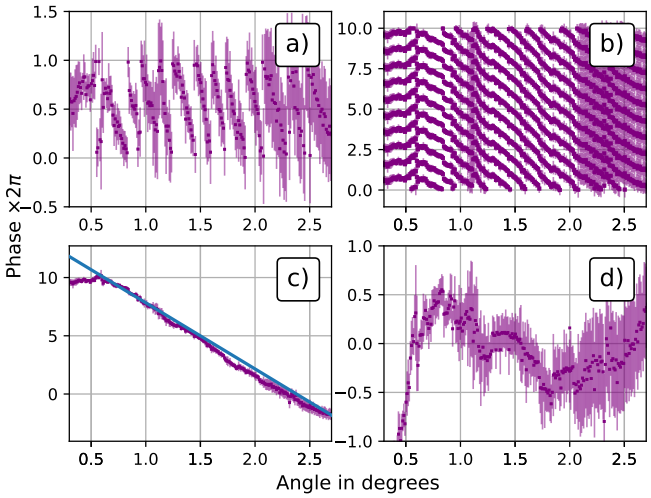

Figure 4.7: Steps for the calibration of the phase information. a) We obtain the raw phase data from the phase dependency plots (Fig. 4.6). b) Then we add the same curve many times with jumps of 2π. c) From this, we select the correct 2π jumps to obtain a continuous line. d) We finally do a linear regression (solid blue line) and subtract the linear regression to obtain the calibrated phase information.

follow this procedure for all the samples present in this chapter.

4.4 From total extinction to scattering amplitude

In our measurements, we extract the normalized mutual scattering component F_{MS} by measuring flux F, which is the integral of the current J over the detector area A [19]. We have two incoming waves with direction $\hat{k}_{\mathrm{in},1}$ and $\hat{k}_{\mathrm{in},2}$, and we integrate the current that goes in the direction $\hat{k}_{\mathrm{in},2}$. The mutual scattering in the direction of $\hat{k}_{\mathrm{in},2}$ is expressed as [71]

$$J_{\mathrm{MS}}\hat{k}_{\mathrm{in},2} = A_1 A_2 \mathrm{Im}[f(\hat{k}_{\mathrm{in},2}, \hat{k}_{\mathrm{in},1})e^{i(\Delta\phi_{2,1})}], \tag{4.2}$$

where $f(\hat{k}_{\mathrm{in},i}, \hat{k}_{\mathrm{in},j})$ is the scattering amplitude relating an incoming wave at direction $\hat{k}_{\mathrm{in},j}$ and an outgoing wave at direction $\hat{k}_{\mathrm{in},i}$. A_i is the amplitude of the wave at direction $\hat{k}_{\mathrm{in},i}$, and $\Delta\phi_{i,j}$ is the phase difference between the two incoming waves.

The complex-value scattering amplitude f can be decomposed in the exponent form as $f = |f|e^{(i\phi_f)}$. Thus, Eq. 4.2 can be simplified as follows:

$$J_{\mathrm{MS}}\hat{k}_{\mathrm{in},2} = A_1 A_2 |f_{2,1}| \sin(\phi_f + \Delta\phi_{2,1}), \tag{4.3}$$

where we change the notation $f_{i,j} \equiv f(\hat{k}_{\mathrm{in},i}, \hat{k}_{\mathrm{in},j})$ for simplicity. The same notation follows for the phase component. We see that we maximize this component if we set the phase difference as $\Delta\phi = \pi - \phi_f$. Knowing this, we obtain ϕ_f in our experiment by scanning the phase and finding the maximum value. Furthermore, the maximum value of the current is $\max(J_{\mathrm{MS}}\hat{k}_{\mathrm{in},2}) = A_1 A_2 |f|$. Consequently, we measure the amplitude of the incoming waves A_1, A_2 separately, and hence we obtain $|f|$.

For some cases, it is more informative to normalize the mutual scattering by the self-extinction $J_{\mathrm{in}} = A_2^2 \operatorname{Im}(f_{2,2})$, as we do for our experimental results. We define the normalized mutual scattering as

$$F_{\mathrm{MS}} = \frac{\int_A J_{\mathrm{MS}}}{\int_A J_{\mathrm{in}}}, \tag{4.4}$$

where we integrate the current over the detector area A to obtain the flux. Thus, the effect of the mutual scattering on the total extinction is clearer: if $1 - F_{\mathrm{MS}} = 2$, the total extinction is twice as large. If $1 - F_{\mathrm{MS}} = 0$, the total extinction vanishes. Experimentally, F_{MS} is obtained by measuring the flux for different scenarios, as shown in Eq. 4.1.

4.5 Experimental results

4.5.1 General observations

We measure the mutual scattering component for 4 samples: a dielectric sphere, a single black human hair, a strip of pultruded carbon, and a block of ZnO_2. We show the results for all the samples in Fig. 4.8 and Fig. 4.9. The top panel of each figure shows the angular dependency of the amplitude of the modulation, where the blue circles and green squares represent the minimum and maximum modulation, respectively, obtained by changing the phase. These values are obtained from the phase dependency at each angle, as shown in the example of Fig. 4.6.

Additionally, the solid red lines in Fig. 4.8 show the results from our Mie modes, both for amplitude and phase. Note that we plot the model against the right y-axis, which has a scaling and offset factor for clear comparison. We include multiple model curves with 2π spacing to account for the periodicity of the phase. For our calculations, we use a sphere geometry for the dielectric sphere and a cylinder geometry for the single human hair. The inputs to the model are the refractive index of the sample n_{s}, the refractive index of the medium n_{m}, and the sample radius r_{s}. The parameters used for the models are presented in Table 4.1. Obviously, these Mie models are not applicable to the strip of pultruded carbon and the block of ZnO_2 due to their complicated shape.

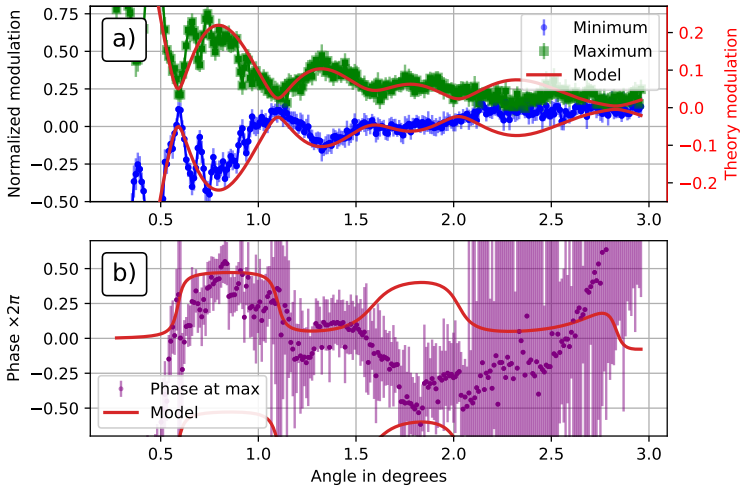

(a) Polystyrene sphere.

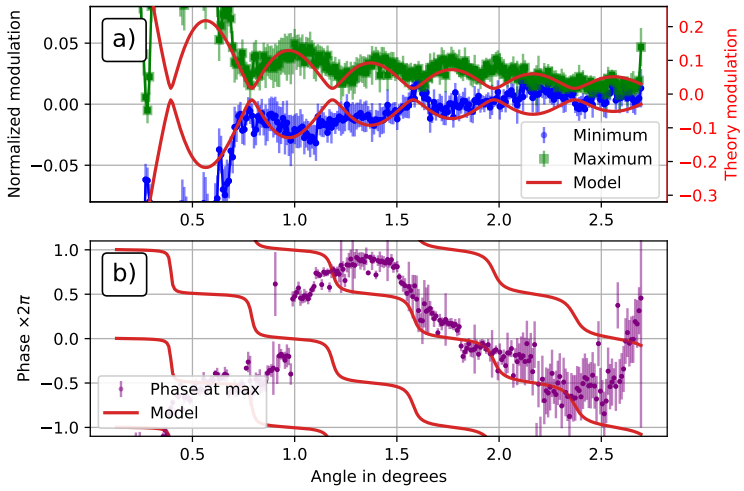

(b) single black human hair.

Figure 4.8: Mutual scattering result for a) polystyrene sphere and b) single black human hair. Both sub-figures have two panels, top and bottom. The top panel shows the amplitude of the total extinction modulation, and the bottom panel shows the phase of the modulation. At the top, green square symbols are the maximum modulation, and blue square symbols are the minimum modulation. The solid red line shows the results from our model. This model at the top panel is plotted against the right red y-axis.

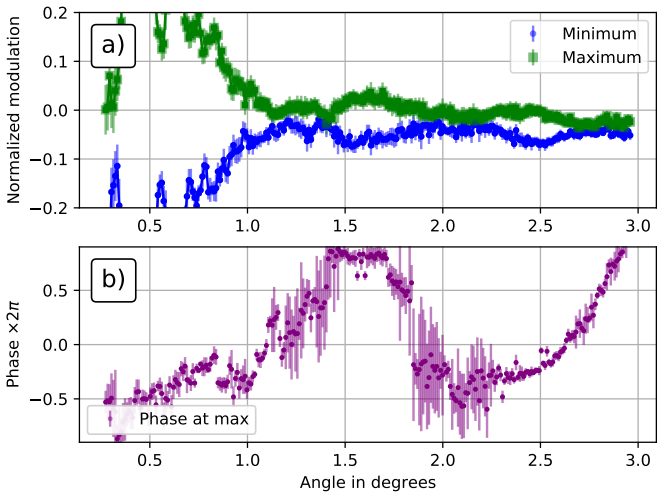

(a) Pultruded carbon strip.

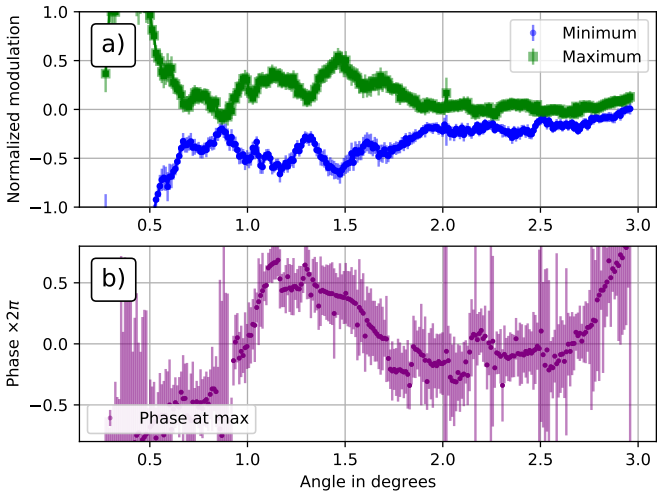

(b) ZnO_2 block.

Figure 4.9: Mutual scattering result for a) pultruded carbon strip and b) ZnO_2 block. Both sub-figures have two panels, top and bottom. The top panel shows the amplitude of the total extinction modulation, and the bottom panel shows the phase of the modulation. At the top, green square symbols are the maximum modulation, and blue square symbols are the minimum modulation.

Sample	n_s	n_m	$2r_s$ (μm)
Polystyrene sphere	1.5875[1]	1.412[1]	59
single black hair	1.55+1i [116]	1	92

Table 4.1: Table of parameters used for our Mie calculations. ([1]From manufacturer)

The bottom panel of each sub-figure of Fig. 4.8 and Fig. 4.9 shows the angular dependency of the phase information, which is the phase at which we obtain the maximum value (green squares in the top panel). We calibrate the phase information as discussed previously. When the amplitude of mutual scattering is close to zero, the phase has an increasing error margin. We consider these as the points where the phase is *undefined*.

4.5.2 Polystyrene sphere

We see in Fig. 4.8a that the measurements of the polystyrene sphere have a trend that is in agreement with our model, both in amplitude and phase. In a previous work [70] (see Chapter 3), we show how analytical models are in agreement with experiments when the angle is close to zero $\gamma \to 0$, and when increasing the angle the model deviates, as we approach the *speckle regime*, where the distribution of scatterers and the exact 3D shape of the object gain more relevance. Here we see a similar behavior, with the model for the amplitude information starting to deviate around $\gamma = 2.1°$. Around $\gamma = 1.5°$, the model and the data seemingly split; the model goes upwards while the data goes downwards. Although the trend is different, the phase goes down to $-0.5 \times 2\pi$, which is close to the value of the model after accounting for the periodicity of the phase.

The measurements show that the phase becomes undefined at the *nodes* of the amplitude, namely around $\gamma = 0.6°$ and $\gamma = 1.2°$. We call these *closed nodes*, where the modulation is so small that it is not possible to define the optimal phase. Still, a third node is present around $\gamma = 1.6°$ which is not accompanied by an undefined phase. We call these types of nodes *open nodes*, as the gap between maximum and minimum modulation is not completely closed.

The measurements of the polystyrene sphere show a larger error range compared to the other samples. This is mainly due to the low contrast of the refractive index between the sample and the surrounding media. This translates into a weak scattering signal and, thus, a lower signal-to-noise ratio (SNR). This is particularly relevant at the end of the angular range for the amplitude data, where the low SNR makes the phase undetermined. Interestingly, the phase data starts deviating from the theory just at the point of the expected third node, which is an open node, located before the amplitude deviates from the theory.

A possible reason for the differences between theory and experiments is the geometry of the sample. While the Mie calculations assume a perfect, homogeneous sphere, our sphere is exposed to fabrication imperfections. As an example, it has been previously observed [136] that a dielectric sphere fabricated by a two-step growing process has the scattering properties of two spheres, one inside the other.

Our experiment is particularly sensitive to such effects when increasing the angle γ, as we are entering the speckle regime.

4.5.3 Human hair

For the measurements of the single human hair shown in Fig. 4.8b, we see that the model is in good agreement with the experimental measurement of the amplitude of mutual scattering. Similar to the polystyrene sphere, when increasing the angle we approach the speckle regime and the model deviates from the experimental data. This happens around $\gamma = 1.9°$, although for small angles we also see a difference between the model and the data, as the first node of the model is not present in the experimental data. Note that for very small angles, the two incoming Gaussian beams overlap in the area of the detector, and thus the measurements are less precise.

For the phase measurements, we see an abrupt jump of $\delta\phi \approx \pi$ around $\gamma = 1°$, which is not accounted for in the model. Besides this, the phase information follows the same decreasing trend as the analytical model. We also see that even though we have nodes in the amplitude measurements, the phase is never undefined, even when $\gamma > 1.9°$ where the model starts deviating from the amplitude data.

In this case, the Mie calculation is useful as a first approach, but incomplete. We can use it to, *e.g.*, extract the width of the sample, which dictates the periodicity of the nodes in the amplitude data; we note that the periodicity of the nodes in the sphere measurements is larger than the periodicity in the hair measurements, meaning the sphere is smaller than the hair. Nevertheless, the complexity of a biological sample as a single human hair is not encapsulated in our calculations, where we assume the sample to be a perfect cylinder. It is well known that human hair is composed of layers, namely the cortex, medulla, and cuticle. [137, 138] Each layer has different scattering properties, and it may not be homogeneous along the hair. [113, 116] Furthermore, the surface of the human hair may contain overlapping cuticle cells that form a scale-like structure, deviating even more from the ideal structure used in the calculation. The scanning electron microscope (SEM) images shown in Fig.4.10 provide an insight into the structure of human hair, revealing deviations from the assumed cylindrical shape. The cross-sectional images presented in Fig.4.10a,b show that the hair strand in our sample seems to have a triangular shape. Additionally, Fig. 4.10c,d highlight the presence of scale-like structures, which as we mentioned before, are not accounted for in the Mie calculation. In addition, the calculation imposes a certain orientation of the sample with respect to the incident beam. Thus, any tilt in the sample is reflected in the measurements. This is not a problem in the case of the sphere because of its symmetry.

4.5.4 Pultruded carbon strip

For the amplitude data of the pultruded carbon in Fig. 4.9a, we identify three nodes, namely around $\gamma = 1.25°$, around $\gamma = 2.1°$, and around $\gamma = 2.8°$. These

nodes are not as clear as for the rest of the samples, and other interpretations are possible, *e.g.*, instead of a single node around $\gamma = 1.25°$, there might be two nodes close to each other, around $\gamma = 1.2°$ and $\gamma = 1.45°$. For the case of the phase data, we see a long step between $\gamma = 1.2°$ and $\gamma = 1.8°$, where the phase is also undefined. These positions are close to the nodes described above.

Due to the free-form shape of this sample, it is very challenging to build an analytical mathematical model to predict experimental results, which is the type of challenge we address in our research program "Free form scattering optics (FFSO)". We may, in turn, use a simpler approximate model based on diffraction theory, with which we model the sample as a perfectly flat, fully absorbing object. One of the many problems with this approach is that it is highly sensitive to the geometry and orientation of the sample. Even supposing the sample has a perfect cuboid shape, mutual scattering depends heavily on the orientation of the sample with respect to the axis where the angle γ between the two incoming beams is formed. We hypothesize that the orientation of the carbon strip is the reason why the first node is not so clear for this measurement.

4.5.5 Block of ZnO_2

In Fig. 4.9b, we see that there are many nodes in the amplitude measurements that show up at specific angles. These nodes are located at $\gamma = 0.69°$, $0.87°$, $1.03°$, $1.3°$, $1.62°$, $2.0°$, $2.17°$, $2.27°$, and $2.5°$. Some of these nodes also have undefined phases. However, there are four nodes at $\gamma = 0.69°$, $1.03°$, $1.3°$, and $1.62°$ that do not have undefined phase, which we call open nodes. As in the previous cases, the phase data shows a long step between the node at $\gamma = 0.87°$ and the node at $\gamma = 2.0°$. This step seems to agree with an overall increase in the amplitude data.

To better analyze the amplitude data, we divide it into two functions: One with a strong angle dependency, known as the carrier signal, and another with a weak angle dependency, known as the envelope signal. The carrier signal is responsible for the nodes that are present across the entire angular range and is in sync with the points of undefined phases. The envelope signal, on the other hand, is responsible for the overall increase in the amplitude data and is in sync with the step present in the phase data. We attribute these two signals to different characteristics of the free-form nature of the sample. The carrier signal is related to the object's overall shape, while the envelope signal is related to small changes in geometry. Furthermore, the small jumps in phase, such as those observed at $\gamma = 1.17°$, $1.85°$, and $2.14°$, are indicative of the speckle behavior of mutual scattering.

4.6 Conclusions

In this chapter, we present an experimental procedure to measure the modulation of light extinction in different materials. This is done using two incoming laser beams and exploiting mutual scattering. By varying the relative angle and phase between the two beams, we obtain the amplitude of the modulation and the

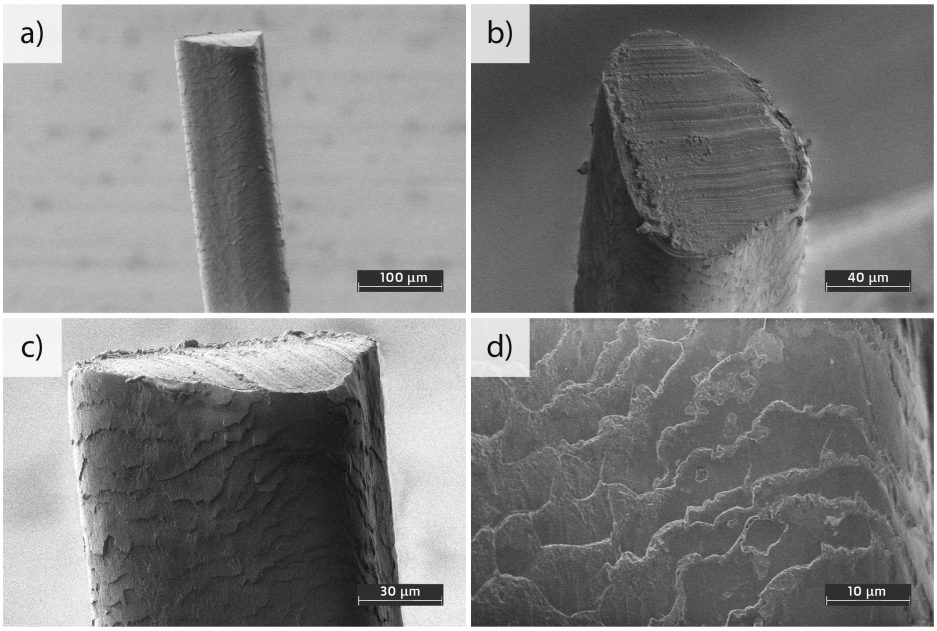

Figure 4.10: SEM images of the human hair sample for different positions and magnifications.

phase at which the extinction is maximized. From this, it is possible to extract the scattering amplitude, which fully describes the light-scattering properties of the object.

We studied 4 samples: a dielectric sphere, a single black human hair, a strip of pultruded carbon, and a block of ZnO_2. All these samples are finite in a three-dimensional space, *i.e.*, smaller than the incident beam, and are embedded in PDMS. Except for the single human hair, which is extended in one dimension and suspended in the air. With all these samples, we cover objects with different geometries, objects that are either absorbing or scattering, and we include a biological sample as well. We compared the polystyrene sphere and the single human hair to Mie calculations, and we found that, especially for the amplitude data, the model is in close agreement with the data. In turn, deviations from the model are attributed to sample characteristics that differ from the ideal, homogeneous geometries considered in the calculations.

In general, we see at the end of the angular range in the phase measurements a steady increase in the signal. This is attributed to the calibration of the experimental setup rather than to the sample itself. This uncertainty keeps us from drawing any conclusion regarding the phase for that region, regardless of the SNR of the measurements. We believe the sample preparation creates a significant amount of degrees of freedom in the calibration. A potential improvement of our measurement method is to develop a predictable and accurate fabrication process such that the calibration is applicable for every angle.

One of the advantages of our approach with mutual scattering is that it is applicable for either very absorbing or very scattering materials. Furthermore, as long as the approximation of far-field holds, mutual scattering is applicable for any sample size and wavelength. By slightly modifying the setup with the right phase modulators, we can adapt the experiment to have a better angular resolution or to extend the angular range. On top of that, a DMD allows us to rotate the plane of the two incoming beams or even add more incoming beams, which resembles the multiple-beam wavefront shaping setup [43, 44]. Finally, we believe the extraction of the complex scattering properties has plenty of promise for future applications in areas such as metrology, microscopy, and nanofabrication.

Chapter 5

Mutual scattering for light extinction optimization

Mutual scattering occurs when multiple coherent waves are incident on a finite-size scattering object and refers to a cross-interference between the incident and scattered waves. By modulating mutual scattering, we control the total extinction of the system, thereby making the object more transparent or more opaque. We present an extension of previous mutual scattering experiments from $N = 2$ to $N = 64$ incident waves (and up to $N_{\max} = 400$). In comparison, wavefront shaping — a well-established modulation technique — optimizes the forward intensity in a given direction. In our study, we compare the final intensity and extinction in a particular outgoing direction when maximizing intensity through wavefront shaping and maximizing transparency through mutual scattering. As expected, wavefront shaping outperforms mutual scattering in terms of maximizing intensity. Intriguingly, however, we not only find that mutual scattering is superior to wavefront shaping in maximizing transparency, but also that applying wavefront shaping actually increases the extinction of the system, and thus *decreases* the transparency. These findings open up opportunities for further comparisons between wavefront shaping and mutual scattering to discern when one approach is better than the other, as well as for exploring additional applications of light extinction optimization, such as increasing the extinction of fluorescent particles to enhance their emission or decreasing the extinction of samples in optical tweezers to mitigate the effects of heating in the sample.

5.1 Introduction

Mutual scattering is a recently discovered effect, which is always present when multiple coherent incident waves pass through a finite-size object [69, 71]. If multiple incident waves cross in a finite sample, there is a cross-interference between one coherent incident wave and the scattered wave generated due to another incident wave. This cross interference is the mutual scattering effect, which affects the total extinction of the sample. With mutual scattering, we tune the extinction of the sample, making it appear more transparent (minimizing the extinction) or more opaque (maximizing the extinction) [70].

Mutual scattering was originally discovered while studying energy conservation in wavefront shaping. Wavefront shaping is an extensively used technique for studying light scattering, where the incident wavefront is modulated to achieve a specific transmitted wavefront [43, 63, 72, 103, 139]. The incident wavefront is modulated such that the light propagation through the sample is controlled by interference. These interferences generate a random pattern in the far field, called the speckle pattern.

So far, mutual scattering has only been studied when $N = 2$ incident waves are present. Although many applications of mutual scattering — *e.g.* optical characterization, optical cloaking — do not require more incident waves, having a larger $N > 2$ number of incident waves makes it possible to compare wavefront shaping and mutual scattering. This is particularly interesting because it shows the differences — both at the fundamental level and for applications — between optimizing light intensity in a detector plane and optimizing light extinction through a sample.

In this chapter, we perform a study to greatly expand the mutual scattering measurements to a large number of beams $N_{\max} = 400$. We use this to compare the enhancement of intensity η_{I} and enhancement of transparency η_{E} when optimizing intensity (wavefront shaping) and when optimizing extinction (mutual scattering). We tackle the question, does maximizing forward intensity and minimizing extinction yield the same result?

5.2 Experimental methods

To optimize light extinction using the mutual scattering effect, we use the experimental setup described in Chapter 4, with the main difference being that now we do not have only two incident beams, but up to $N_{\max} = 400$ beams. We present the diagram of our experimental setup in Fig. 5.1. We use a He-Ne laser (Hughes 3225H-PC, 5mW, $\lambda = 632.8$ nm) as a source and a $\times 15$ telescope to enlarge the beam area. We use a digital micromirror device (DMD, Vialux VX4100) for wavefront modulation. Since the DMD is a binary amplitude modulator, we use the Lee holography technique to convert it into phase modulation [79, 80]. We implement the holographic filter needed for this technique using lenses L3 and L4 and an iris in between, followed by a focusing lens L5. We use two charge-coupled device cameras (CCD, Stingray F-125) to detect the flux F integrating over the illuminated pixels. We form two paths with a beamsplitter, and we

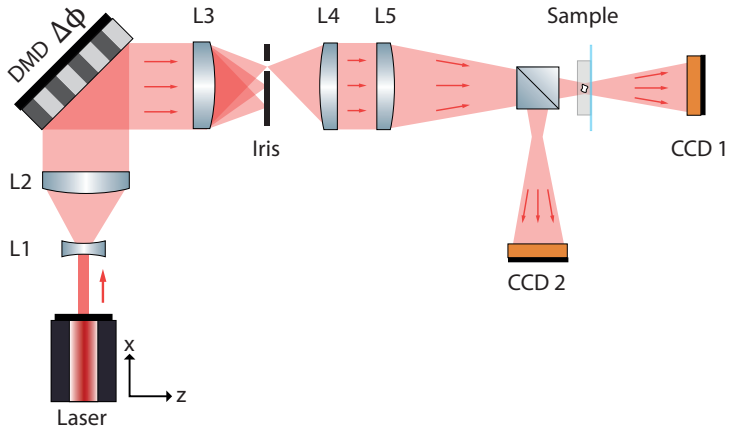

Figure 5.1: Diagram of the experimental setup. The incident beams are generated using active areas in the digital micromirror device, which also sets the phase difference between the beams. Lenses L3 and L5 and the iris are used for the holographic filter needed for the Lee holography technique, which allows us to control the phase of the wavefront. The wavefront is focused into the sample by lens L5 and then collected by camera CCD1. CCD2 is placed virtually at the same position as camera CCD1 without a sample in front.

place two cameras, CCD1 and CC2, at the same distance from the beamsplitter, beyond the focal distance of the lens L5. The sample — a single strand of hair suspended in the air — is positioned in one of the focus in front of camera CCD1. Camera CCD1 measures the flux of the incident beams after passing through the sample, whereas camera CCD2 measures the flux of the incident beams without the sample. Additionally, we place a powermeter (not shown) at the beginning of the optical circuit to correct for laser fluctuations.

To extend the experiment shown in Chapter 4 from 2 beams to N beams, we filled the DMD screen with active areas, using all active areas simultaneously. An active area is a collection of adjacent DMD pixels (in this case, 72 pixels) that are simultaneously activated, surrounded by inactive pixels. Therefore, we followed the same optimization procedure explained in Chapter 2, where we optimize each active area separately using Zernike polynomials to correct for the aberrations induced by the DMD. We show the final results in Fig. 5.2.

Although it was possible to optimize the entire DMD at once, this approach was not pursued due to the desire for a clear separation between incident beams and to avoid excessively small beam waists at the focus point, to remain within the resolution of the CCD camera. Moreover, optimizing the entire continuous wavefront would require a larger number of Zernike coefficients compared to optimizing smaller active areas independently.

If only two active areas are ON, the angle formed by the two incident beams depends on the relative position between the active areas that can be tuned with high resolution by changing their separation pixel by pixel. If multiple

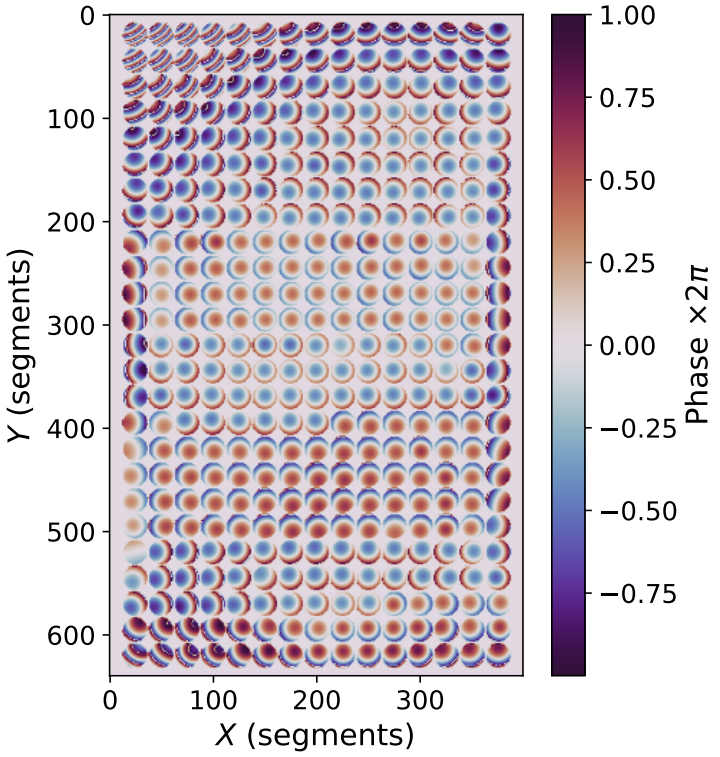

Figure 5.2: Phase masks in DMD for every active area. We control the phase of each segment of the mask from 0 to 2π. Each circle corresponds to a different incident angle at the sample. All pixels outside the circles have phase *and amplitude* 0. The color bar is circular (the color at 1 is the same as the color at -1) to account for the periodicity of the phase.

beams are present simultaneously, the angular resolution is dictated by the size of the active area. For this experiment, we chose active areas with a diameter of $d = 72\text{px} = 777.6\mu\text{m}$ with a minimum separation of $d_{\text{gap}} = 3\text{px} = 32.4\mu\text{m}$, resulting in a maximum number of beams equal to $N_{\text{max}} = 25 \times 16 = 400$ with an angular resolution of $\delta\gamma \approx 0.23°$. However, increasing the number of beams increases the duration of the experiment. We realized that only the central segments affected the optimization in a significant way. Thus, we decided to use only the $N = 8 \times 8 = 64$ active areas at the center of the DMD.

5.3 Experimental procedure

In Chapters 3 and 4, we describe how to extract the mutual scattering component from flux measurements when two incident beams are present. Here, we expand the procedure for the case when N beams are incident in the sample. We extract the mutual scattering component in a particular direction $\hat{k}_{\mathrm{in},i}$ by isolating the components of the field that include a cross-interference between the incident beam i and all the scattered waves in the direction $\hat{k}_{\mathrm{in},i}$ generated by the $N-1$ other incident waves.

When N plane waves are incident in a scattering object, the resulting total wave in the far field is a combination of $2N$ waves, namely N incident and N scattered waves

$$\psi = \sum_{i=1}^{N} \psi_{\mathrm{in},i} + \sum_{i=1}^{N} \psi_{\mathrm{scat},i}, \tag{5.1}$$

Where ψ is the resulting field, $\psi_{\mathrm{in},i}$ is the incident wave in direction $\hat{k}_{\mathrm{in},i}$ and $\psi_{\mathrm{scat},i}$ is the scattered wave generated by the incident wave $\psi_{\mathrm{in},i}$. $\psi_{\mathrm{in},i}$ is a plane wave only present in direction $\hat{k}_{\mathrm{in},i}$, while $\psi_{\mathrm{scat},i}$ is a spherical wave present in all directions.

When we place a detector in the far field, we measure a *flux* F, which is the integral of the *current* J over the area A of the detector equal to

$$F = \int_A J \mathrm{d}A = \int_A \mathrm{Re}\left[(\partial_t \psi)^* \boldsymbol{\nabla} \psi\right] \mathrm{d}A. \tag{5.2}$$

Because N incident waves are present, F is composed of $N!$ components. We assume the detector area to be small w.r.t. the angular dependency of the scattered waves such that $F = \int_A J \mathrm{d}A = JA$. To simplify the notation, we define the operators $\star$ and $\star\star$ as

$$x \star y \equiv \mathrm{Re}\left[(\partial_t x)^* \boldsymbol{\nabla} y\right], \tag{5.3}$$

$$x \star\star y \equiv x \star y + y \star x. \tag{5.4}$$

With this, we express J as

$$\begin{aligned} J = &\sum_{i=1}^{N} \psi_{\mathrm{in},i} \star \psi_{\mathrm{in},i} + \sum_{i=1}^{N} \psi_{\mathrm{scat},i} \star \psi_{\mathrm{scat},i} + \sum_{j=i+1}^{N} \sum_{i=1}^{N-1} \psi_{\mathrm{in},i} \star\star \psi_{\mathrm{in},j} \\ &+ \sum_{j=i+1}^{N} \sum_{i=1}^{N-1} \psi_{\mathrm{scat},i} \star\star \psi_{\mathrm{scat},j} + \sum_{i=1}^{N} \psi_{\mathrm{in},i} \star\star \psi_{\mathrm{scat},i} + \sum_{j=i+1}^{N} \sum_{i=1}^{N-1} \psi_{\mathrm{in},i} \star\star \psi_{\mathrm{scat},j}, \end{aligned} \tag{5.5}$$

where the first term of Eq. 5.5 is the flux of the incident beams, the second term is the flux of the scattered waves, the third term shows the interference between incident waves, the fourth term shows the interference between scattered waves, the fifth term shows the self-extinction of each beam, and the sixth term is the mutual scattering.

We are interested in optimizing mutual scattering in a particular direction, *e.g.* $\hat{k}_{\mathrm{in},1}$. To isolate the terms related to mutual scattering in one direction, we note that by measuring the current without the sample, there are no scattered waves, and so we obtain the first and third terms of Eq. 5.5. To obtain the second and fifth terms, we measure each beam individually. This yields the term $\psi_{\mathrm{in},i} \star \psi_{\mathrm{in},i} + \psi_{\mathrm{in},i} \star \star \psi_{\mathrm{scat},i} + \psi_{\mathrm{scat},i} \star \psi_{\mathrm{scat},i}$, so we also measure the case when no sample is present to eliminate the first term.

Because $\psi_{\mathrm{scat},1}$ is present only if $\psi_{\mathrm{in},1}$ is also present, it is not possible to isolate the mutual scattering term further, but we can make some assumptions instead. It is justified to assume the scattered waves have much smaller amplitudes than the incident waves, which in turn means the interference between two scattered waves has a very small contribution compared to the interference between a scattered wave and an incident wave. This means that the fourth term of Eq. 5.5 is neglected. Furthermore, we assume that in the direction $\hat{k}_{\mathrm{in},1}$, $\psi_{\mathrm{in},1}$ has a much larger amplitude than any other incident beam, and thus any interference between $\psi_{\mathrm{scat},1}$ and $\psi_{\mathrm{in},i\neq 1}$ is much smaller than the mutual scatter term. This means that the sixth term is reduced to $\sum_{i=2}^{N} \psi_{\mathrm{in},1} \star \star \psi_{\mathrm{scat},i}$. It remains to be tested that these assumptions are reasonable in experiments.

Considering the procedure explained in this section, we extract the mutual scattering term for N incident beams in the direction $\hat{k}_{\mathrm{in},1}$ as $F_{\mathrm{MS}} = J_{\mathrm{MS}} A$, with

$$J_{\mathrm{MS}} \approx J - J_{\mathrm{NS}} - \sum_{i=1}^{N} \left(J_i - J_{i,\mathrm{NS}} \right), \tag{5.6}$$

where J is the current when all beams are present and the sample is placed in the experiment, J_{NS} is the current when all beams are present and no sample is placed in the experiment, J_i is the current when only $\psi_{\mathrm{in},i}$ is present and the sample is placed in the experiment, and $J_{i,\mathrm{NS}}$ is the current when only $\psi_{\mathrm{in},i}$ is present and no sample is placed in the experiment. We see that to measure the mutual scattering of N incident beams, we need a total of $2N+2$ measurements.

5.4 Results and discussion

The first relevant measurement related to light extinction optimization using mutual scattering is to compare it to wavefront shaping (WFS), which is uniquely concerned with light intensity. We could use WFS to optimize light extinction by optimizing the forward intensity *e.g.*, maximizing the forward intensity as a means to minimize the light extinction, but this method is incomplete. As we described in the previous section, the resulting wave in far-field has multiple

Target	η_{I}	η_{E}
Intensity	4.69	0.63
Transparency	1.70	1.47

Table 5.1: Intensity enhancement η_{I} and transparency enhancement η_{E} after optimizing for intensity (wavefront shaping) and optimizing for extinction (mutual scattering).

interference terms besides the light extinction term. If we are only concerned about light intensity, then it is more efficient to optimize the interference between the incident waves in the detector plane than to optimize the light extinction in the sample.

To compare mutual scattering and wavefront shaping, we implemented both techniques in our experiments. We chose the central active area of the DMD as $\hat{k}_{\mathrm{in},1}$. First, we maximize the intensity (wavefront shaping) in the direction $\hat{k}_{\mathrm{in},1}$ using the sequential algorithm [43]. In the sequential algorithm, we scan every active area one by one, changing the phase from 0 to 2π, and selecting the phase that maximizes the intensity. We use three iterations of this algorithm. Once the maximization is complete, we measure the final intensity *along with the final light extinction* and we compare them to their initial values. Second, we optimize the extinction (mutual scattering) in the direction $\hat{k}_{\mathrm{in},1}$ by maximizing the transparency, *i.e.*, minimizing the light extinction. Again, once the maximization is finalized, we measure the final intensity along with the final light extinction and we compare them to their initial values.

In Table 5.1, we show the intensity enhancement η_{I} and the *transparency* enhancement η_{E} for both optimizations, wavefront shaping and mutual scattering. We decided to refer to transparency instead of extinction to have a more intuitive comparison between maximizing intensity and maximizing transparency. The intensity enhancement is calculated as in previous wavefront shaping studies [43, 63, 72, 103, 139], and the transparency enhancement is defined as

$$\eta_{\mathrm{I}} \equiv \frac{I_{\mathrm{opt}}}{\langle I_0 \rangle}, \tag{5.7}$$

$$\eta_{\mathrm{E}} \equiv \left[\frac{F_{\mathrm{ext}} + F_{\mathrm{MS,opt}}}{\langle F_{\mathrm{MS,opt}} + F_{\mathrm{MS},0} \rangle} \right]^{-1}, \tag{5.8}$$

with I_{opt}, $F_{\mathrm{MS,opt}}$ the final intensity and extinction, respectively, $\langle I_0 \rangle$, $\langle F_{\mathrm{MS},0} \rangle$ the ensemble average of the initial intensity and extinction, respectively, and $F_{\mathrm{MS,opt}}$ the total extinction before optimization. Note that the transparency enhancement metric is defined as the inverse of the extinction enhancement. We also show in Fig. 5.3 the intensity and extinction pattern in the vicinity of the direction $\hat{k}_{\mathrm{in},1}$ after intensity and extinction.

From the results presented above, we see that maximizing intensity with wavefront shaping yields a higher intensity enhancement than when maximizing transparency with mutual scattering. This agrees with our initial hypothesis. Importantly, although the enhancement is low, we see that there is an increase in

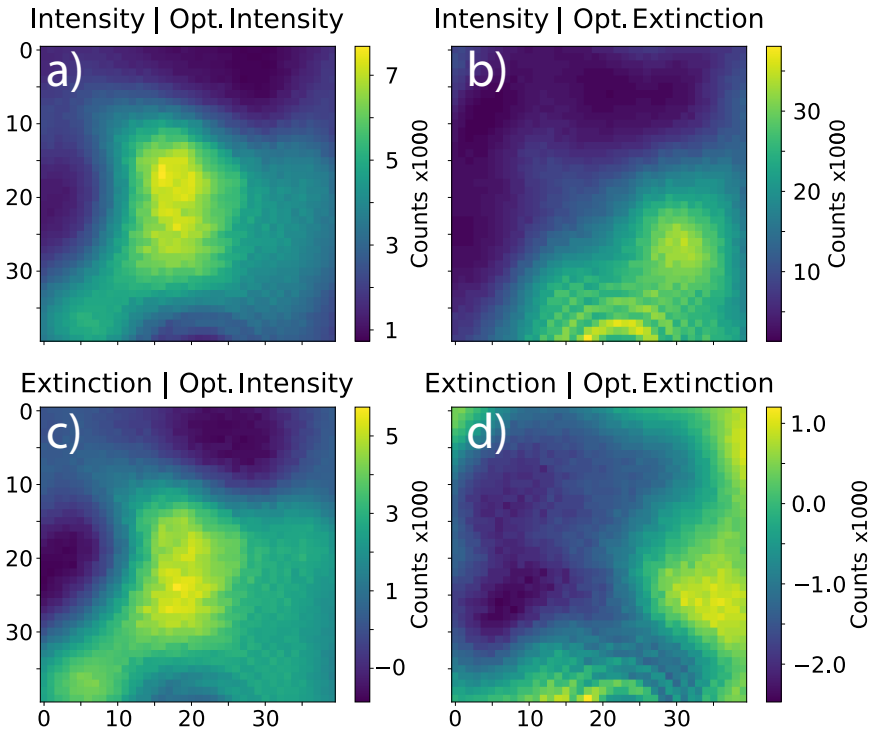

Figure 5.3: (a,b)Intensity and (c,d)extinction pattern in the vicinity of the direction $\hat{k}_{\mathrm{in},1}$ after optimizing (a,c) intensity and (b,d) extinction.

intensity when maximizing transparency using mutual scattering. When looking at the transparency enhancement, we see that the transparency increases ($\eta_E > 1$) when maximizing transparency, while it decreases ($\eta_E < 1$) when maximizing intensity with wavefront shaping. A lower transparency means that we extract more light out of the incident beam, which seems to be in contradiction with the fact that the resulting intensity increases. However, as we measure extinction and intensity in a certain direction, the increase in intensity is most probably due to interference between the incident waves and not necessarily due to cross-interference between the incident waves and the scattered waves. This means that when we maximize intensity, we focus more on the waves passing *on the sides* of the sample, regardless of how much light interacts with the object.

An important parameter to compare mutual scattering and wavefront shaping is time. Although better algorithms and faster modulation devices can be used, the amount of ancillary measurements needed to measure mutual scattering makes this alternative much slower than wavefront shaping. This limits applications of light extinction optimization using mutual scattering to static materials.

5.5 Summary and outlook

We draw a comparison between maximizing intensity using wavefront shaping and maximizing transparency using mutual scattering. We optimize the phase of multiple waves incident with different directions and measure intensity and extinction in a specific outgoing direction. As anticipated, wavefront shaping proves to be more effective in maximizing intensity. Intriguingly, however, we not only find that mutual scattering is superior to wavefront shaping in maximizing transparency, but also that applying wavefront shaping actually increases the extinction of the system, and thus *decreases* the transparency.

For future steps, new samples with various scattering properties should be studied to generalize the results for other samples. Furthermore, by changing the focusing lens, we can adjust the angular resolution such that all the active areas of the DMD make a non-negligible contribution to light extinction. And as the angular range needed depends on the sample size, both parameters have to be decided accordingly.

Our results open up opportunities for further comparisons between wavefront shaping and mutual scattering. Specifically, we introduce mutual scattering as a novel approach to optimize extinction, prompting us to investigate its applicability, especially in areas where wavefront shaping may not be viable. Notably, optimizing extinction has important implications in various applications, such as fluorescent particles and optical tweezers. For instance, optimizing extinction in fluorescent particles leads to higher fluorescence signals, as increased absorption results in an enhancement of excited signals. Conversely, a limitation of optical tweezers is the absorption of samples, especially biological samples, as the heat generated during absorption damages the samples. Reducing the absorption of samples in optical tweezers would significantly broaden the applicability of this technique.

Chapter 6

Wavefront shaping through a free-form scattering object

Wavefront shaping is a technique to study and control light transport inside scattering media. Wavefront shaping is considered to be applicable to any complex material, yet in most previous studies, the only sample geometries that are studied are slabs or waveguides. The slab geometry offers a simple approach to light scattering but is in its essence not relevant to practical applications in industry, where free-form shape and finite devices are used. In this chapter, we study how macroscopic changes in the sample shape affect light scattering using the wavefront shaping technique. Using a flexible scattering material, we optimize the intensity of light in a focusing spot using wavefront shaping and record the optimized pattern, comparing the enhancement for different curvatures and beam radii. We observe the changes in light transport inside the material due to macroscopic changes of the shape by measuring the correlation of optimized wavefronts. We validate our hypothesis that wavefront shaping has a similar enhancement regardless of the free-form shape of the sample and thus offers relevant potential for industrial applications. We propose a new figure of merit to evaluate the performance of wavefront shaping for different shapes. Surprisingly, based on this figure of merit, we observe that for this particular sample, wavefront shaping has a slightly better performance for a free-form shape than for a slab shape.

6.1 Introduction

How to transport light efficiently from A to B? This deceivingly simple question is the central challenge in the functionality of daily used devices such as cameras, projectors, lighting systems, and even optically-secured bank cards. When light travels from point A to B through a transparent medium with macroscopic, optionally curved, surfaces it follows a path that — following the famous principle of Fermat (1658) — has an optical length which is an extremum [26]. This changes fundamentally when the medium contains microscopic particles that scatter light. The technologically relevant question "what happens when both macroscopic curved interfaces and nanophotonic scattering media appear simultaneously", has remained unaddressed and unanswered yet. To date, free-form optics and nanophotonics have developed separately from each other, the former originating from optical engineering and the latter from condensed matter physics. The interplay between microscopic scattering and refraction or reflection by macroscopic free-form surfaces offers new, largely unexplored, opportunities and solutions to diverse technological problems.

The question of how light travels efficiently from A to B is central to many advanced technologies that play important roles in modern society, such as high-precision metrology for integrated nano-circuits in the Internet of Things (IoT) and our smartphones, or detectors in earth-observing satellites. In modern optics, the question is addressed by custom-designing free-form components — lenses and curved mirrors —- that transfer a given distribution of light at the source to a desired distribution at the target. Over the last decade, free-form optics have been used in the development of versatile, miniature, and efficient devices that appear in daily life [26, 27].

While nanophotonic media that scatter light cannot be understood with current free-form design methodologies, many modern devices greatly benefit from these media. For instance, in our homes, offices, and streets, a quiet revolution is taking place as white LEDs are replacing energy-inefficient light sources. A white LED consists of a blue diode [140], whose output is converted and diffused in a layer of phosphor particles [95, 141]. The presence of the light-scattering (and also absorbing and re-emitting) phosphor layer is essential to the functionality of a white LED. Other applications of nanophotonic media include high-precision metrology tools for nanolithography, the calibration of space instruments for earth observations, and novel (quantum) optically secured information technology for privacy. Currently, it is not feasible to describe light-scattering coatings, diffusers, or suspensions with free-form optics. Conversely, in nanophotonics, analytic solutions exist only for simple sample geometries such as spherical, slab, and planar. No analytic solutions exist for arbitrary free forms. The presence of microscopically structured materials in macroscopic free forms implies a huge difference in scale to which conventional optical models cannot be applied. Hence current industry solutions invoke shortcuts, including untested assumptions. Today's lack of knowledge on free-shape scattering optics hampers fast, efficient, and systematic design progress as well as the development of new optical architectures.

One method extensively used for studying nanophotonic scattering media is wavefront shaping (WFS), where the light propagation through a scattering medium is controlled by interference [43, 63, 72, 103, 139]. These interferences generate a random pattern in the far field, called the speckle pattern. Recently, the potential of WFS has been extended to, for instance, time-varying samples [61, 104, 142], and periodic samples such as 2D (and 3D) photonic crystals [143, 144]. The interferences inside a scattering media are considered random. But still, when certain properties are only slightly changed, a correlation in the speckle pattern persists. This is called the memory effect and has been studied by changing the angle of the incident beam, its position on the sample, and its wavelength [39–42]. But for all these experiments, the sample's shape was kept constant.

In most cases to date, WFS has been done on the quintessential scattering sample shape, namely in slabs. However, as previously illustrated, real-world applications require samples to have a free-form shape and be finite. Although many robustness studies have been made in WFS, as far as we know, no study includes changes in the sample's shape. Because of that, the impact of the macroscopic characteristics of the object is not addressed in current theories.

Here, we present the study of an opaque sample of TiO_2 particles suspended in silicone, as shown in Fig. 6.1. Exploiting the mechanical flexibility of silicone, we modify the shape of the sample and measure the enhancement of the intensity η in a point of the speckle pattern. We used a tailored-made sample holder to change both the curvature of the flexible sample and a focusing lens with a linear stage to change the beam radius on the sample. When it is curved, the sample has a curvature radius of approximately $R_c = 15$ mm. The thickness and the radius of curvature of the slab are inspired by the dimensions used in, *e.g.*, the Philips HUE bulb, see Fig. 6.1b). In this product, a set of colored LEDs is used to create both colored and white light at will using wireless control. To mix the light of these LEDs, the outer bulb plays an instrumental role. The typical thickness of the bulb is close to 2mm, and the radius varies with position, of which we considered 15 mm a typical value. We compare the performance of WFS in a flat and a free-form sample as a function of beam radius. With this, we want to draw the attention of the community to study the properties of industrially relevant free-form scattering objects both in theory and experiments.

6.2 Experimental Methods

The optical setup is depicted in Fig. 6.2[1]. We use a green laser (Coherent COMPASS 315M-100, $\lambda = 532$ nm) as a source, and we modulate the wavefront using a digital micromirror device (DMD, DLP7000 Texas Instruments). To convert the binary amplitude modulation into a phase modulation, we use the Lee holography technique [79, 80] implemented with a 4f system, where we filter the -1 order in the Fourier plane with an iris. The beam is then focused into the

[1]The setup is based on the COPS wavefront shaping "demo" that is compact and portable for demonstrations in schools and other venues

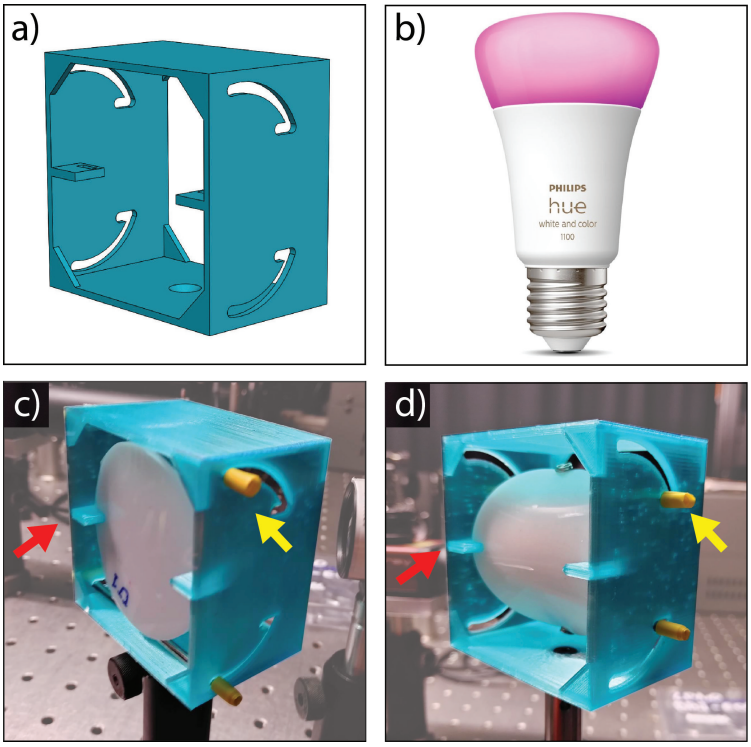

Figure 6.1: Tailored-made holder and sample used for experiments. a) 3D model of the sample holder. b) Commercial smart light bulb, Philips HUE, from which the free-form shape of our sample is inspired. c) The sample in the sample holder in the flat position, and d) the sample in the curved position. The sample is attached horizontally to the holder (red arrow) and vertically to two movable metal bars (yellow arrow). The bars move in the range delimited by the rails on the side of the holder.

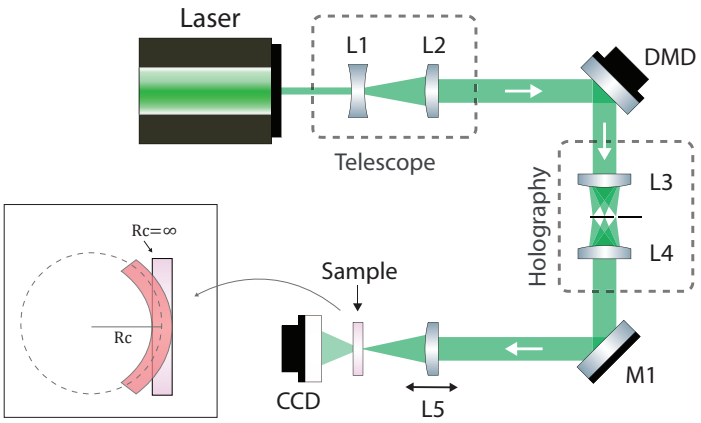

Figure 6.2: Experimental setup for wavefront shaping. We use a DMD device combined with the Lee holography method to achieve phase-only modulation. Lens L5 is placed on top of a linear stage, to control the distance between L5 and the sample. We collect the speckle pattern in transmission. Inset: diagram of the curvature of the sample R_c. The sample is curved in such a way that the position of the center of the sample is constant. The sample is curved using the holder shown in Fig. 6.1. (L: lens; M: mirror).

scattering material, placed in a tailored-made holder, and a CCD camera (Guppy PRO F-125b) collects the light transmitted through the sample. The focusing lens L5 is placed on top of a linear stage to have control over the position of the sample related to the focal length. The information collected from the CCD camera is used to optimize the DMD pattern following the sequential algorithm [43, 44].

The sample consists of TiO_2 particles suspended in silicone with a weight concentration of 0.1 wt%. The sample has a wafer-like shape with a thickness of $L = 2$ mm. To study the free-form sample, we exploit the flexibility of silicone to do measurements when the sample is flat and perpendicular to the incident beam and when the sample is curved. To curve the sample in a controlled manner, we designed a special sample holder, shown in Fig. 6.1. The sample is attached to the holder from the side with clamps and on the top and bottom to sliding metallic bars. These fixed points are highlighted in Fig. 6.1c) and Fig. 6.1d) with yellow and red arrows, respectively. When the bars are close to the front, the sample is completely flat, and when the bars are fixed close to the back, the sample is curved. With this holder, we control the curvature of the sample during scattering and wavefront shaping experiments while other physical parameters are constant.

6.3 Enhancement in curved objects

A relevant parameter to study in WFS experiments is the intensity enhancement η. The enhancement is defined as

$$\eta \equiv \frac{I_{\text{opt}}}{\langle I_0 \rangle}, \tag{6.1}$$

where I_{opt} is the intensity at the target position after wavefront optimization and $\langle I_0 \rangle$ is the ensemble average intensity of the pattern before optimization [46]. The ensemble average intensity is calculated by averaging the total counts on the detector at the target position over multiple random wavefronts.

We compare a free-form sample with a slab-like shape by measuring the enhancement η for a different number of segments N_{s}. In Fig. 6.3, we plot $\eta(N_{\text{s}})$ for both a flat and a curved sample. Each symbol is composed of the maximum enhancement obtained with the corresponding number of segments, averaged over three iterations of the optimization loop. Every iteration uses a flat incident wavefront as the initial value, meaning each optimization is independent of the others. Fig. 6.3 also includes two curves corresponding to theoretical limits. We see that the maximum theoretical limit is considerably above the experimental data. This is because the maximum theoretical limit does not take into account variations in the speckle size. In section 6.4 we will elaborate an extension of the theoretical limit, which yields values much closer to the experimental data.

Fig. 6.3 shows that both shapes give the same trend in enhancement, suggesting that the performance of the wavefront shaping technique is the same regardless of the macroscopic properties of the object. This is in agreement with our hypothesis and current theory of wavefront shaping [20, 68]. If we represent the scattering object as a random transmission matrix, regardless of the value of each coefficient, the efficiency of the wavefront optimization is unchanged. A possible effect that would cause a change in the total enhancement is if the number of open channels changes, changing the saturation point of the enhancement. Our data does not show any sign of a change in saturation, meaning the number of open channels is seemingly unchanged.

An alternative interpretation of these results is that the curvature is simply not affecting the light transport inside the material or that it only affects the border of the optimized wavefront with a curvature effect. To test this new hypothesis, we calculate the correlation between the optimized wavefront of different measurements. For each number of segments, we have a total of 6 measurements, three from a curved sample and three from a flat sample. We take the optimized wavefront for each measurement, and we calculate the Pearson correlation coefficient between the 6 cases. We use the SciKit python library to calculate the correlation, which is defined as [145]

$$C_{\text{P}} \equiv \frac{\sum_{\text{i,j}}(x_{\text{i,j}} - \overline{x})(y_{\text{i,j}} - \overline{y})}{\sqrt{(\sum_{\text{i,j}}(x_{\text{i,j}} - \overline{x})^2 (y_{\text{i,j}} - \overline{y})^2}}, \tag{6.2}$$

with $x_{\text{i,j}}$ the value of segment (i, j) of the first wavefront, $y_{\text{i,j}}$ the value of segment (i, j) of the second wavefront, and $\overline{x}$, $\overline{y}$ the average segment values of the first and second wavefront, respectively.

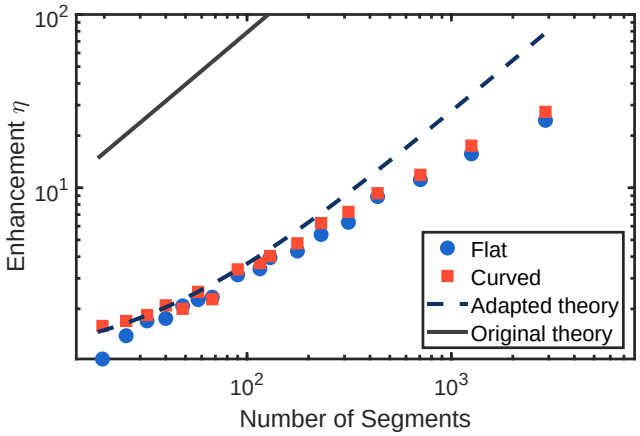

Figure 6.3: Enhancement versus the number of active modulating segments. The diameter of the illumination area is $2r_b = 4.5mm$. The blue circles represent the enhancement when the sample is flat and the red squares are for the curved sample. Each symbol is an average from three independent repetitions of the optimizations. The dashed line is the theoretical curve after correcting for the variable speckle size, while the solid line is the maximum theoretical curve without correction. Wavefront shaping is as effective in optimizing the intensity of a curved sample as it is with a flat sample.

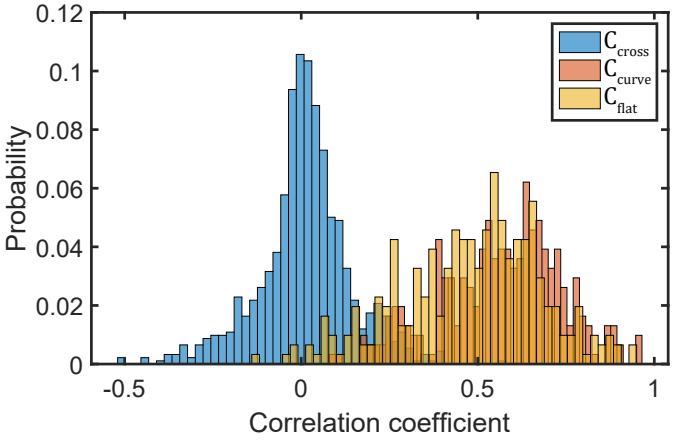

Figure 6.4: Correlation distribution between optimized phase patterns. The blue distribution corresponds to the correlation between patterns from different shapes, while the orange and yellow distribution corresponds to the correlation between the same sample's shape (curve and flat, respectively).

We separate the correlations of wavefronts into three classes: the cross-correlations between wavefronts for a flat and a curved sample C_{cross}, the correlation between wavefronts with flat shape C_{flat}, and the correlation between wavefronts with curved shape C_{curve}. For the cases where the sample's shape is not changed (C_{flat} and C_{curve}), we expect the optimized wavefronts to converge to a similar configuration, therefore, a high mutual correlation, regardless of the hypothesis we mentioned before.

If the macroscopic shape does affect the light transport when we change the sample's shape, we expect the optimized wavefront to converge to a new configuration, therefore C_{cross} to be small. On the other hand, if the macroscopic changes do not affect the light transport, then we expect the same value of C_{cross} regardless of the sample's shape.

The probability distribution of the correlations is shown in Fig, 6.4. We see that C_{cross} is centered at 0 and extends from about -0.3 to $+0.3$. In contrast, both C_{flat} and C_{curve} have higher and mostly positive correlations, between 0 and 1 and centered near 0.5. From this difference, we conclude that the macroscopic shape of the object affects the light transport inside it, and to control the scattered light in a free-form shape, we need a new optimized wavefront compared to the flat shape.

In the field of light scattering, the *memory effect* is a widely known property [17, 20, 39, 41]. The memory effect shows that when the light transport inside the scattering media is slightly changed, the speckle (and thus the optimized wavefront) are correlated with the previous one. This means that the same optimized wavefront can be used to enhance the intensity. From our observation that curved wavefronts are nearly uncorrelated with flat wavefronts, we conclude that the change in curvature is beyond the range of the memory effect. In previous studies, the light transport is changed by displacing the scattering media, tilting the incident beam, or changing the wavelength of the source. We thus believe our work is the first step towards studying the free-form memory effect, *i.e.*, the memory effect when changing the shape of the scattering media.

In theory, we expect the distributions of C_{flat} and C_{curve} to be centered at 1, while they are centered at 0.5. We attribute this to the fact that the DMD is not evenly illuminated because the laser beam has a Gaussian profile. Thus, the segments at the edges do not affect the optimization significantly, and hence the weights of each $(x_{\text{i,j}}, y_{\text{i,j}})$ from Eq. 6.2 are different between one iteration and the other, thereby decreasing the correlation.

6.4 Enhancement in presence of variable speckle size

To estimate the maximum enhancement possible η_0 in WFS, one generally invokes wave-guide approximations typical of random matrix theory [31–33, 68]. We simplify the scattering medium as a set of scattering channels, and we conclude that the maximum enhancement is obtained when all the channels are optimized. This is expressed as

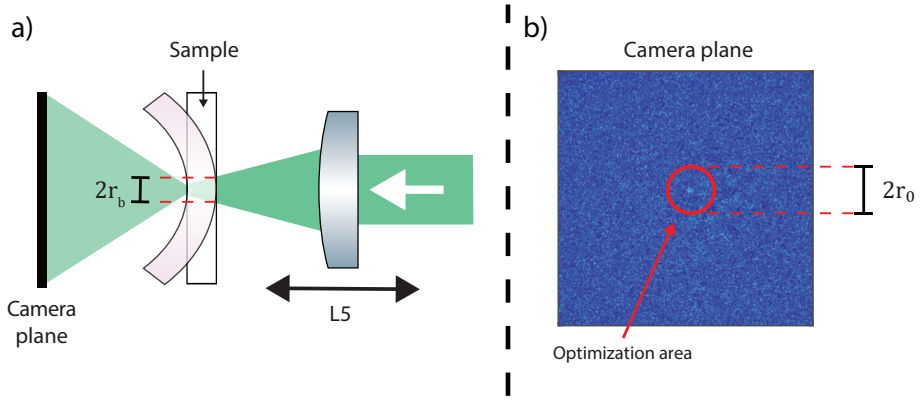

Figure 6.5: a) Cartoon diagram of the illumination area, defined by its radius r_b. This depends on the distance between lens L5 and the sample. The curvature of the diagram is exaggerated for a didactic purpose. b) Diagram of the optimization area on the camera, defined by its radius r_o. This depends on the speckle size at the detector. To maintain a standard comparison, we keep r_o constant in our experiments.

$$\eta_0 = \frac{\pi}{4}(N_s - 1) + 1, \tag{6.3}$$

where N_s is the total number of segments used in the modulator. This equation is valid for phase-only modulation and does not consider the saturation point when N_s is equal to the number of transmission channels inside the sample N_c.

To compare η_0 with our experiments, we need to distinguish between the beam radius r_b and the optimization radius r_o. This difference is illustrated in Fig. 6.5, where r_b is the radius of the illumination area at the sample surface that depends on the focusing lens L5 and the position of the sample. Conversely, r_o is the radius of the area of the speckle pattern that we observe at the detector, and it is relative to the speckle size of the speckle pattern.

Although the optimization process does not depend on r_b directly, it depends on r_o. This is because to get the maximum enhancement, the optimization area must have the same size as a single speckle $r_o = r_s$. The size of this single speckle in the detector plane depends on the design of the experiment, particularly if we use or not a lens at the detector. For our measurements, we use a lens-less system, hence the size of a single speckle is equal to [146].

$$r_s = \frac{2.44 \cdot \lambda}{4r_b} d, \tag{6.4}$$

with λ the wavelength of the incident light and d the thickness of the sample. We infer from Eq 6.4 that r_o and r_b are inversely related, which means the optimization process depends on both parameters.

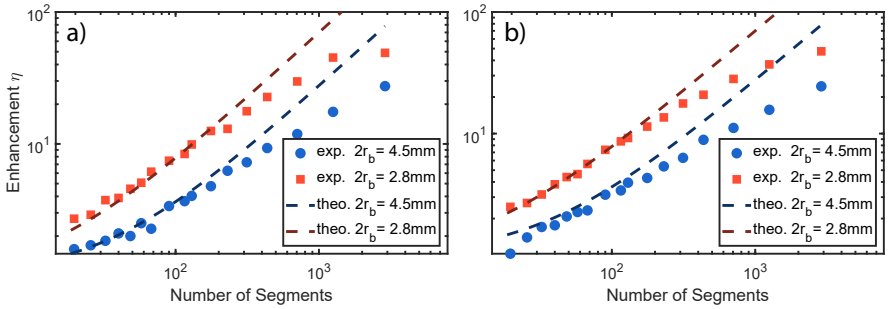

Figure 6.6: Enhancement versus the number of active modulating segments for a) flat shape and b) curve shape. On each plot, we show the enhancement for the maximum ($2r_\mathrm{b} = 4.5$ mm, blue circles) and minimum ($2r_\mathrm{b} = 3.8$ mm, red squares) illumination radius. The dashed lines show the theoretical enhancement corrected based on r_b.

In Ref. [107], Ojambati and co-workers studied how the maximum enhancement changes when changing r_o, thus $\eta_0' = \eta_0'(r_\mathrm{o})$. This dependency is expressed as [107]

$$\eta_0'(r_\mathrm{o}) = \frac{K}{r_\mathrm{o}^2} + 1, \tag{6.5}$$

where the correction factor K depends on the number of segments N_s and on the speckle size. The theoretical limit η_0 is reached when r_o approaches the speckle size $r_\mathrm{s}(r_\mathrm{b})$, $\lim_{r_\mathrm{o}\to r_\mathrm{s}(r_\mathrm{b})} \eta_0'(r_\mathrm{o}) = \eta_0$. If we take the limiting value of $r_\mathrm{o} = r_\mathrm{s}(r_\mathrm{b})$ in Eq. 6.5 and we replace it with Eq. 6.4, and we take the limiting value of $\eta_0'(r_\mathrm{o}) = \eta_0$ and we replace it with Eq. 6.3, we obtain an extended correction factor $K(N_\mathrm{s}, r_\mathrm{b})$:

$$K(N_\mathrm{s}, r_\mathrm{b}) = \frac{2.44^2\pi\lambda^2}{4^3 r_\mathrm{b}^2} d^2(N_\mathrm{s} - 1). \tag{6.6}$$

Finally, the theoretical enhancement corrected for optimization and beam areas is given by

$$\eta_0'(r_\mathrm{o}, r_\mathrm{b}) = \frac{2.44^2\pi\lambda^2}{4^3 r_\mathrm{b}^2 r_\mathrm{o}^2} d^2(N_\mathrm{s} - 1) + 1. \tag{6.7}$$

In Eq. 6.7 we see that the enhancement is inversely proportional to r_b^2 and r_o^2, and directly proportional to d^2. This is in accordance with usual WFS experiments, where one focuses the incident beam to a narrow spot and reduces the optimization area to a single speckle while placing the detector far from the sample to increase the size of the speckle on the detector. In our experiments r_o is fixed, and we compare the measurements while varying r_b.

6.5 Effect of sample curvature

We study the impact of the ratio between the beam radius r_b and the radius of curvature of the sample R_c. We vary the radius r_b in a range between 1.9 mm and 2.3 mm (hence diameters $2r_\mathrm{b} = 3.8$ to 4.6 mm) by changing the position of the focusing lens L5 (see Fig. 6.2). We measure the enhancement versus number of segments N_s (as in Fig 6.3) for six different beam radii r_b and both flat and curved sample's shapes.

Fig. 6.6 shows the enhancements for the lowest and highest r_b for both shapes, along with the maximum theoretical limit for each case, calculated from Eq. 6.7. We see that the enhancement decreases when increasing the beam radius, and so does the theoretical limit. This is in accordance with our theory (see Eq. 6.7). When increasing r_b, the speckle size is smaller. If r_o is constant, there are more speckles inside the optimization area, thus the maximum enhancement is lower.

Finally, we compare the enhancement of a curved and a flat sample for different r_b. For this comparison, we propose the following figure of merit F, defined as:

$$F \equiv \langle \eta_c / \eta_f \rangle_N, \tag{6.8}$$

with η_c the enhancement for the curve shape, η_f the enhancement for the flat shape, and $\langle . \rangle_N$ the *geometric mean* over the number of segments N. This figure of merit is applicable regardless of the shift shown in Fig. 6.6 because we expect this shift to occur both in the flat and the curved shape.

We show F in Fig. 6.7 for different beam radii. We see that F is constant at about $F = 1.08$ and it is independent of r_b.

Finally, we see that all data are larger than $F = 1$, showing that, on average, we achieve a larger enhancement with a curve shape instead of a flat shape. This challenges the current theoretical framework of wavefront shaping because no fundamental scattering property was changed except the macroscopic sample's shape, yet based on this figure of merit, the enhancement difference is statistically significant.

6.6 Conclusions

In this chapter, we studied how the intensity enhancement obtained using wavefront shaping changes when we change the macroscopic properties of the object. We compare the case of two macroscopic shapes, a free-form curved sample and a flat sample with a slab shape. We used a tailored-made sample holder to change the curvature of a flexible sample and a focusing lens with a linear stage to change the beam radius on the sample.

We see a low correlation between the optimal wavefronts for different macroscopic shapes, suggesting a change in the light transport inside the scattering media at a mesoscopic level. Meanwhile, when optimizing the intensity using the wavefront shaping technique, we reach a similar enhancement for a curved sample

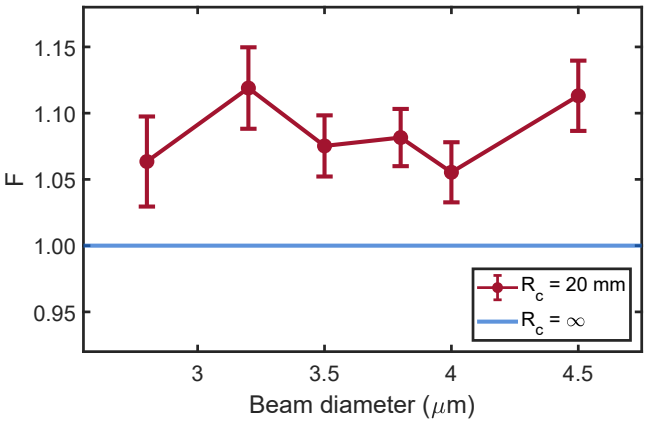

Figure 6.7: The figure of merit versus beam diameter $2r_\mathrm{b}$. The figure of merit is based on comparing a curved sample with $R_\mathrm{c} = 20$ mm and a flat sample ($R_\mathrm{c} = \infty$). The light blue line corresponds to the case when the curvature is not changed, *i.e.*, $F = 1$.

as for a flat sample. This is in agreement with our hypothesis; regardless of the changes in light transport, the number of open channels is unchanged, thus the maximum enhancement is not affected by these changes. Our results confirm the idea that wavefront shaping is applicable regardless of the form of the object.

We derive an extension of the theory for maximum enhancement based on the beam radius and the optimization radius. Our experiments are in agreement with our theoretical prediction, and our theory explains the trend for both a curved and flat sample. Furthermore, we propose a figure of merit to compare the enhancement between different shapes. Based on this figure of merit, we see an increase in the total enhancement by 10% for every beam radius. This increase is not explained using current theories, which are based on slab shapes only.

With this chapter, we aim to encourage the community to consider free-form objects both in experiments and theory of light scattering, as they have a larger impact on industrial applications.

Chapter 7

Enhanced Secrecy in Optical Communication using Speckle from Multiple Scattering Layers

We study the secrecy of an optical communication system with two scattering layers, to hide both the sender and receiver, by measuring the correlation of the intermediate speckle generated between the two layers. The binary message is modulated as spatially shaped wavefronts, and the high number of transmission modes of the scattering layers allows for *many* uncorrelated incident wavefronts to send the *same* message, making it difficult for an attacker to intercept or decode the message and thus increasing secrecy. We collect 50,000 intermediate speckle patterns and analyze their correlation distribution using Kolmogorov-Smirnov (K-S) test. We search for further correlations using the K-Means and Hierarchical unsupervised classification algorithms. We find no correlation between the intermediate speckle and the message, suggesting a person-in-the-middle attack is not possible. This method is compatible with any digital encryption method and is applicable for codifications in optical wireless communication (OWC).

Parts of this chapter have been published in A. Rates, J. Vrehen, B. Mulder, W. L. Ijzerman, and W. L. Vos, Optics Express **31**, 23897-23909 (2023) [147].

7.1 Introduction

Scattering of light occurs in any 3D complex opaque material such as paint, foam, or biological tissue, independent of its shape: whether slab, fiber, or free-form [20, 53, 73, 128]. When light travels through a complex material, it takes many different paths or channels inside the medium, whereby the light performs a random walk with a typical step size called the mean free path [20]. Along these contorted paths, the light waves pick up a random distribution of phase changes. Therefore, it is intuitively reasonable that a random interference pattern appears in a target plane, called a speckle pattern, that consists of a random arrangement of bright and dark areas. While a random speckle interference also arises due to scattering from a rough surface [148], the speckle due to light scattering in a 3D complex material has several additional physical properties, notably, a number of intricate correlation functions, see Refs. [20, 128]. Since the arrangement of speckle spots in an observation plane is exceedingly difficult to predict due to the huge number of degrees of freedom in a complex material, the complex light scattering in such materials offers an attractive opportunity to encode information; indeed, complex materials play a central role in optical physically unclonable functions (PUF) and are employed in optical cryptography [149–153].

Although a speckle pattern is random, the intensities of many single speckle spots have a well-defined exponential distribution, also known as the Rayleigh distribution, that is characterized by the average intensity. The transport of scattered light through a complex material is successfully described by random matrix theory from mesoscopic physics, which invokes a large transmission matrix with many complex-valued elements [28, 29, 67, 94], illustrated in Fig. 7.1a). Knowledge of the transmission matrix has been successfully extracted and even applied to imaging and transmitting encoded data [66, 67].

Statistics of the transmission matrix reveal the existence of "closed channels", with zero transmission, and "open channels", with almost perfect transmission [34–37]. So even a thick complex scattering medium is effectively transparent thanks to these states [44]. Modulation techniques such as wavefront shaping (WFS) and mutual scattering profit from the high-transmission states to control the transmission through the scattering medium, thereby modulating the intensity distribution of speckle spots [43, 44, 69, 70]. This can be used, notably, to concentrate the intensity at a specific focal point, transmit information, or change the overall transparency of the scattering medium.

When the properties of the incident light are changed (*e.g.*, positioned, tilted, shaped, or frequency shifted), the light is scrambled in a different way resulting in a new speckle pattern in the observation plane. When the range of perturbations of the incident light is moderate, known as the memory range, the new speckle pattern has remarkable non-zero correlations with the original speckle pattern [39]. This effect is typically characterized by intensity-intensity correlations between pairs of different positions in *one observation plane*, known as C1 correlations [20, 38]. Such speckle and intensity correlations find many applications, ranging from imaging through an opaque screen [110, 154] to transmitting images and information through opaque media [155].

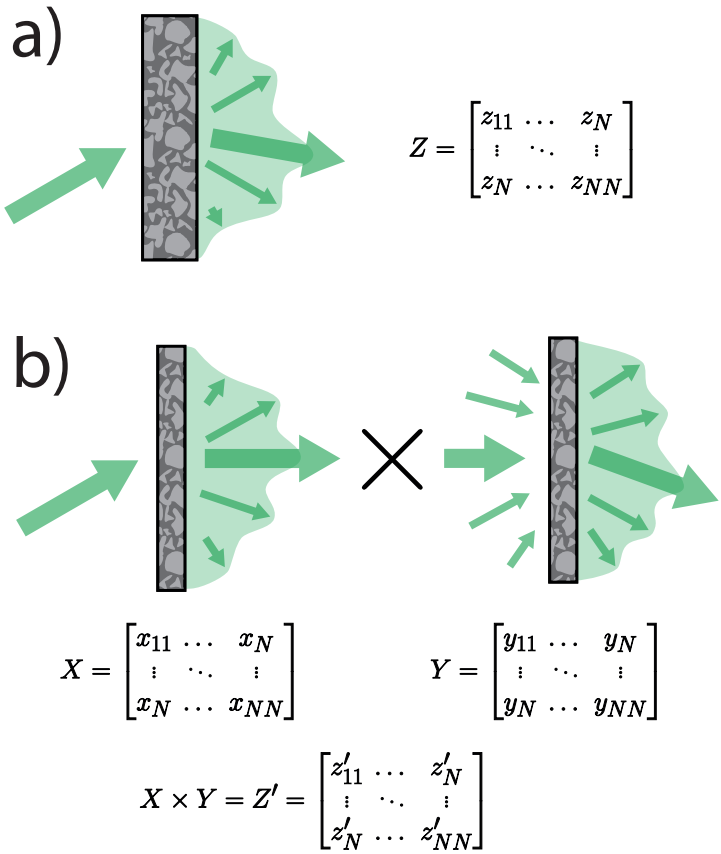

Figure 7.1: Schematic of the light scattering systems studied here. (a) A single incident light beam is sent through $N = 1$ scattering slab, yielding a complex speckle pattern as output. The speckle pattern transmitted through the slab is described by a transmission matrix Z. (b) A single incident light beam is sent through $N = 2$ scattering slabs. The speckle pattern emanating from the first slab is the intermediate pattern (described by transmission matrix X) that is sent onto the second slab (with transmission matrix Y). The final output is a new speckle pattern described by a transmission matrix Z' with $Z' = X \times Y$.

In this chapter, we study speckle correlations in a different setting, where we use two layers of scattering media and observe the *intermediate* speckle pattern in between the scattering layers. Instead of measuring changes of a speckle pattern in a target plane — as is described above — we collect two speckle patterns in *two different observation planes*, namely one in between the two scattering layers and the other after passing through both scattering layers, illustrated in Fig. 7.1b). For applications to optical wireless communication, we study if a binary message sent through these scattering layers can be extracted or not by only observing the intermediate speckle pattern. The presence of the first scattering layer is essential to spatially scrambling the incident wavefront, effectively "hiding" the sending modulator for direct inspection and subsequent decoding. The question we address in this work is whether different incident wavefronts are correlated with each other, knowing the message they result in. In other words, if the two transmitted wavefronts correlate, does that mean the two intermediate wavefronts are also correlated?

We synthesize $N_{\mathrm{W}} = 50,000$ different incident wavefronts and collect the resulting intermediate and final speckle patterns. The message is encoded as an intensity distribution in the final speckle pattern, where each speckle pattern is assigned to either a binary 0 or a binary 1. Thus, we have thousands of available wavefronts to send the same value. We measure the correlation between intermediate speckle patterns, to study if the intermediate speckle patterns resulting in the same message encoded in the final speckle pattern are somehow correlated.

7.2 Working principle and experimental methods

In light scattering theory, and in general in mesoscopic physics, a single thick slab of scattering material with thickness L is equivalent to N thin slabs with average thickness (L/N) since the total thickness is the same: $N(L/N) = L$. Here, we study $N = 2$ as illustrated in Fig. 7.1. A scattering material is represented as a random transmission matrix that couples the modes of the incident light to the ones of the outgoing light, and the random components of the transmission matrix represent the scattering events inside the material [20, 28, 30]. Studying $N = 2$ scattering slabs is represented as the multiplication of two of these random matrices, which because it is a linear system, results in yet another random transmission matrix. The reasoning above implies that techniques such as wavefront shaping or mutual scattering are also relevant and valid when multiple slabs are used, independent of the distance between the slabs. Here, we study if there are correlations between the intermediate speckle pattern that we observe between the two scattering slabs on the one hand and the output speckle pattern on the other hand.

To study the speckle correlation, we used the experimental setup shown in Fig. 7.2. The initial light source is a frequency-doubled continuous wave green ($\lambda = 532$ nm) Nd:YAG^3+ laser (Coherent Compass 315M-100, 100mW). The signal is encoded as a phase-modulated wavefront using a digital micromirror

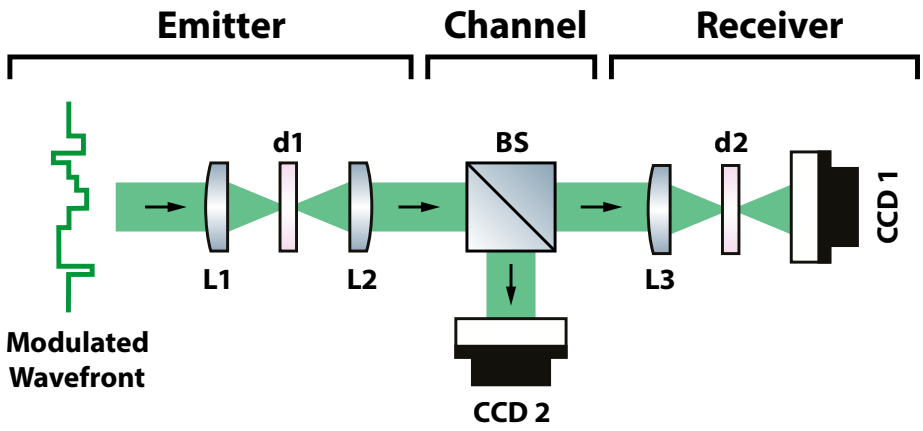

Figure 7.2: Diagram of the experimental setup. The incident wavefront is spatially phase-modulated using a digital micromirror device (DMD, not shown) [156]. The diffusers d_1 and d_2 are scattering materials forming speckle patterns. Camera CCD1 records the final speckle pattern after both d_1 and d_2 and CCD2 records the intermediate pattern after d_1 only. (L: Lens, BS: Beamsplitter).

device (DMD, Vialux VX4100), in the same way as usually done in Wavefront Shaping experiments [156]. The DMD applies a binary, ON-OFF modulation to the wavefront, which we transform into a phase modulation using the Lee Holography technique [79]. Using phase modulation rather than amplitude-only modulation we achieve greater control over the scattering events. [79, 80] The modulated wavefront is focused into a diffuser (Ground Glass Diffuser 220 Grit, Thorlabs) using lens L1 ($f = 75$ mm), and collimated using a microscope objective (NA=0.3, Nedoptifia Zeist). This diffuser has a large diffusing pattern and high transmission, and it is commonly used in scattering experiments [154, 157]. To measure the light speckle between the diffusers, a beamsplitter is used to pick up half of the signal, which is collected by a charge-coupled device (CCD) camera (Guppy F-146B), to detect the intermediate speckle pattern. The other half is focused on a second diffuser similar to the first one using lens L3 ($f = 50$ mm), and collected by a second CCD camera (Stingray F-125), which we call the receiver. The CCD camera is placed in the far field, at a distance of 30 mm from the second diffuser.

Light coherence is a key factor in our experiment. We need spatial coherence in order to obtain and measure the speckle pattern. In our experiment, we use a well-defined laser beam as a source, meaning we have a high temporal and spatial coherence. The laser Coherent Compass 315M-100 is estimated to have a line width of around 10MHz, and a coherent length on the order of tens of meters [158], by far sufficient for our purposes. Our experiment has a path length on the order of one meter, thus ensuring the wavefront is spatially coherent.

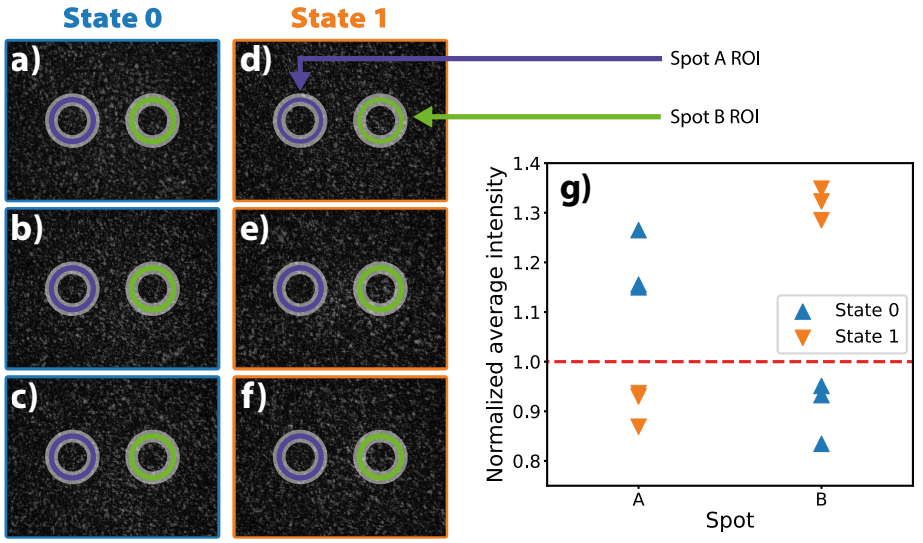

Figure 7.3: Examples of observed speckle patterns. (a-c) Speckle patterns selected as state 0. (d-f) Speckle patterns selected as state 1. The colored circles in each panel show the region of interest (ROI) of spot A (purple) and spot B (green). (g) Average intensity of spot A and spot B normalized by the average intensity of the background for each speckle pattern selected as state 0 or state 1.

7.3 System characterization

The goal of our experiment is to send a signal through the two scattering slabs and study if there is any correlation between the intermediate speckle pattern and the resulting pattern. As a starting point, we aim to obtain a binary signal, *i.e.*, only two levels: state 0 and state 1. Obviously, the modulated incident wavefront has many more degrees of freedom than these two states. For this reason, there exist multiple incident wavefronts, and thus multiple intermediate speckle patterns, that can result in the same signal. We use this property to see if different intermediate speckle patterns need to have some degree of correlation in order to result in the same final state.

To be robust against environmental noise and to have a large dynamic range, we consider in the receiver plane only two regions of interest (ROI), called spot A and spot B, as shown in Fig. 7.3. From the intensity distribution of the speckle at the receiver, we estimate this area to be $\times 15$ larger than the size of a single speckle. Only when the local average intensity of spot A is high and the local intensity of spot B is low, a state 0 is received. Conversely, if the local intensity of spot A is low and the local intensity of spot B is high, state 1 is received, see Fig. 7.3g).

To select the speckle patterns corresponding to state 0 or state 1, we send a total of $N_{\mathrm{W}} = 50,000$ randomized wavefronts. For each wavefront, the speckle pattern at CCD2 is collected along with the intensities at spot A and spot B.

Table 7.1: Example of pairs of intermediate speckle patterns used to calculate the Pearson correlation distribution for each relevant case. The left column indicates the case, while the right column shows each pair used for that case. The letters between parentheses refer to the sub-figure indexes of the speckle patterns shown in Fig. 7.3.

Case	Pairs of speckle patterns
0-0 correlation	(a,b), (a,c), (b,c)
1-1 correlation	(d,e), (d,f), (e,f)
0-1 correlation	(a,d), (a,e), (a,f), (b,d), (b,e), (b,f), (c,d), (c,e), (c,f)

From the definition of each state, we define arbitrary intensity thresholds based on the joint intensity distribution of spot A and spot B, shown in Fig. 7.4, where the thresholds are marked with dashed lines. For both spot A and spot B, we set the thresholds at 20% and 80%. This means that a speckle pattern is classified as state 0 only if the intensity at spot A is higher than 80% of the distribution, and the intensity at spot B is lower than 20% of the distribution. The classification of wavefronts as state 1 follows the same principle.

The red and yellow regions in Fig. 7.4 highlight which speckle patterns are accepted as state 0 or state 1, respectively. With the given thresholds, there is a total of $N_{\mathrm{W},0} = 1839$ available wavefronts (3.7% of the total) to get a state 0, and $N_{\mathrm{W},1} = 1774$ (3.5% of the total) to get a state 1. We modulate the wavefront using a grid of 15×15 segments, controlling the phase of each segment. In our current realization, we modulate the phase from 0 to 2π in 16 steps. That means that the maximum number of different wavefronts that we generate is equal to $N'_{\mathrm{W}} = 16^{225}$, which is on the order of $\mathcal{O}(10^{307})$. The large complexity of the scattering material is such, that small changes in the phase of a single segment at the modulator produce large changes in the intensity distribution at the receiver. This means that the number of available wavefronts can be made arbitrarily large, at the expense of longer measurements and digital memory.

7.4 Correlation distribution of intermediate speckles

Every wavefront used to send a message also generates an intermediate speckle pattern between the slabs. When sending two messages separately, we generate two intermediate speckles and we calculate the correlation between these two intermediate speckles. We are interested in comparing three cases: the correlation between two speckle patterns from state 0 (0-0 correlation), the correlation between two speckle patterns from state 1 (1-1 correlation), and the correlation between a speckle pattern from state 0 and another from state 1 (0-1 correlation).

We illustrate the combinations of speckles in Table 7.1 using the panel's indexes of Fig. 7.3. To characterize the correlations between speckle patterns, we use the Pearson correlation coefficient C_{P} from the Python library SciKit [145], calculated

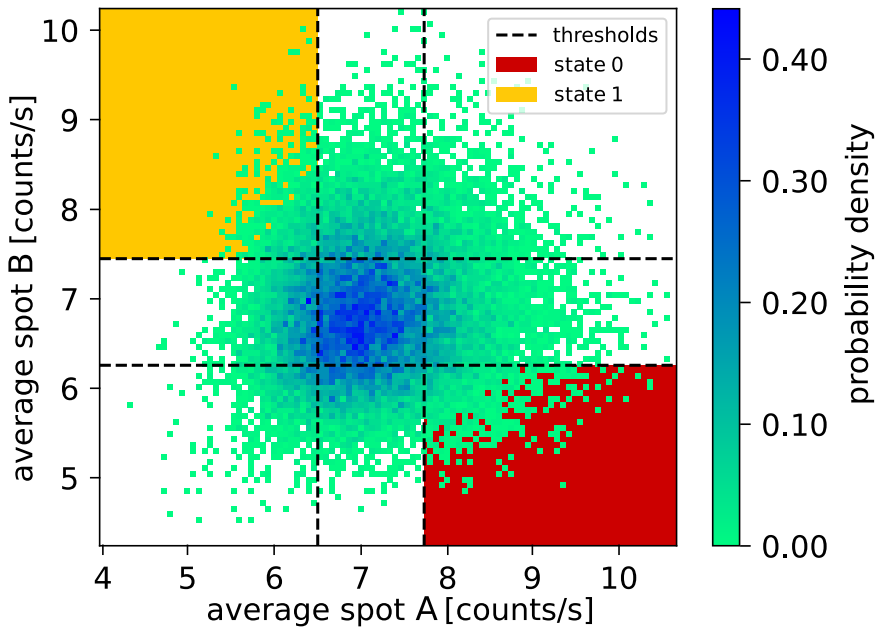

Figure 7.4: Joint distribution of average intensities at spot A and at spot B at the receiver for different incident wavefronts (green symbols). The horizontal and vertical dashed lines are the intensity thresholds that define the states 0 or 1. Here, the red region indicates the accepted state 0 with high intensity in spot A and low intensity in spot B. The yellow region indicates the accepted state 1 with low intensity in spot A and high intensity in spot B.

Table 7.2: K-S statistic between the different correlation distributions. Each K-S statistic is calculated between Dataset 1 and Dataset 2. The p-value for every case is on the order of 10^{-15}.

Dataset 1	**Dataset 2**	**K-S statistic**	p**-value**
0-0 correlation	1-1 correlation	0.03	0.00
0-1 correlation	0-0 correlation	0.03	0.00
1-1 correlation	0-1 correlation	0.02	0.00

as follows:

$$C_{\mathrm{P}} \coloneqq \frac{\sum_{\mathrm{i,j}}(x_{\mathrm{i,j}} - \overline{x})(y_{\mathrm{i,j}} - \overline{y})}{\sqrt{(\sum_{\mathrm{i,j}}(x_{\mathrm{i,j}} - \overline{x})^2 (y_{\mathrm{i,j}} - \overline{y})^2}}, \tag{7.1}$$

with $x_{\mathrm{i,j}}$ the value of pixel (i, j) of the first speckle image, $y_{\mathrm{i,j}}$ the value of the pixel (i, j) of the second speckle, and $\overline{x}$, $\overline{y}$ the average pixel values of the first and second speckle, respectively.

We calculate the correlation C_{P} between two intermediate speckles s_{int}, *e.g.*, $C_{\mathrm{P}}(s_{\mathrm{int},1}, s_{\mathrm{int},2})$. Whether a message is classified as a state 0 or a state 1 does not depend on the intermediate speckle s_{int} but on the final speckle s_{f}. The final speckle is expressed as $s_{\mathrm{f}} = Y s_{\mathrm{int}}$, with the transmission matrix of the second slab as Y (see Fig. 7.1). We thus choose states 0 and 1 as the set of final speckles s_{f} that have a high correlation with the target patterns $s_0^\star$ and $s_1^\star$, respectively. Following what we showed in section 7.3, the target pattern $s_0^\star$ has a high intensity in spot A, zero intensity in spot B, and average intensity elsewhere. Conversely for $s_1^\star$. Thus, an intermediate speckle results in a state 0 if $C_{\mathrm{P}}(Y s_{\mathrm{int}}, s_0^\star) \approx 1$, and in a state 1 if $C_{\mathrm{P}}(Y s_{\mathrm{int}}, s_1^\star) \approx 1$.

When measuring the correlations for the cases 0-0, 1-1, and 0-1, we investigate if the intermediate speckle patterns correlate, given that their resulting speckle correlate. If any correlation is needed to result in the same state, we expect the correlation between two patterns from the same group to be larger than between two patterns from different groups, *e.g.*, we expect the 0-0 and 1-1 correlations to be larger than the 0-1 correlation. For perspective, previous studies of speckle correlation, such as the memory effect, focus on the autocorrelation of the resulting speckle $C_{\mathrm{P}}(s_{\mathrm{f},1}, s_{\mathrm{f},2})$ or in the correlation between the incoming and outgoing pattern $C_{\mathrm{P}}(s_{\mathrm{int},1}, s_{\mathrm{f},1})$.

When we calculate C_{P} between *all* N_{W} available intermediate speckles, *i.e.*, C_{P} between individual pairs of speckles with all the combinations possible, we get a distribution of C_{P}. In Fig. 7.5 we show the correlation distribution for the three cases previously described, 0-0, 1-1, and 0-1. We see that, qualitatively, the distributions are very similar, with the same peak position.

To compare these distributions quantitatively, we used the two-sample Kolmogorov–Smirnov (K-S) test [159]. This test compares the empirical distribution of two sets of observations. When the two observations are from the same distribution, the K-S statistic tends to zero. The results of this test are shown in Table 7.2. We see that the K-S statistic is close to zero and that the p-value is

lower than 5% ($\mathcal{O}(10^{-15})$), this tells us that the correlation distributions of the three groups are indistinguishable.

We see that the correlation distributions are not centered around zero. When we claim there is no clear correlation between speckles from the same group, it is because this correlation is the same as the correlation between speckles from different groups. However, the fact that the correlation is not zero leads to the question if there is any underlying relation between speckle patterns that the Pearson correlation coefficient does not have access to. To test this further, we used unsupervised classification algorithms.

7.5 Unsupervised classification of intermediate speckles

For our analysis of the intermediate speckle correlations, we use two different classification algorithms: the K-means algorithm and the Hierarchical clustering algorithm. We choose these two algorithms based on our familiarity with them, their required input data, and the ability to visually illustrate their classification process, so that we can have a better understanding of the results. We use the open-access Scikit-learn Python library to implement both algorithms. The procedure for classification is the following: first, to reduce the computational time we reduce the resolution of the picture by averaging the 5×5 adjacent pixels. This is much smaller than the speckle size, thus no information is lost. Then, we transform the representation of the data: we consider each pixel as a different dimension and the intensity of this pixel as the position of the realization in that dimension. This forms a new high-dimensional space, called the *feature space*. Due to the resolution of our camera (1280×960) and the reduced resolution, the feature space has almost $50,000$ dimensions, where each point is a realization (or speckle).

To reduce even further the dimensionality of the problem and thus make the problem addressable for a personal computer, we use the principal components analysis (PCA) and only consider the first 100 principal components, explaining $> 90\%$ of the variance of the data. This new data representation is finally used for the classification algorithm, where each principal component is now a dimension of the feature space, and its value corresponds to the position of that dimension. Now, the feature space has $N_\mathrm{d} = 100$ dimensions.

For both algorithms, we use two different classes, intending to separate state 0 and state 1. For the K-Means algorithm, we use 100 initializations and a maximum of $30,000$ iterations. For the Hierarchical clustering algorithm, the agglomerate strategy is used. For the sake of generality, the classification is also run without reducing dimensionality, *i.e.*, without using PCA. For these cases, the image was reduced by averaging the 10×10 adjacent pixels, considering the data memory compared with the previous cases.

We show the results of the classification in Table 7.3. In total, four classification methods are used, two different algorithms, and two different data representations.

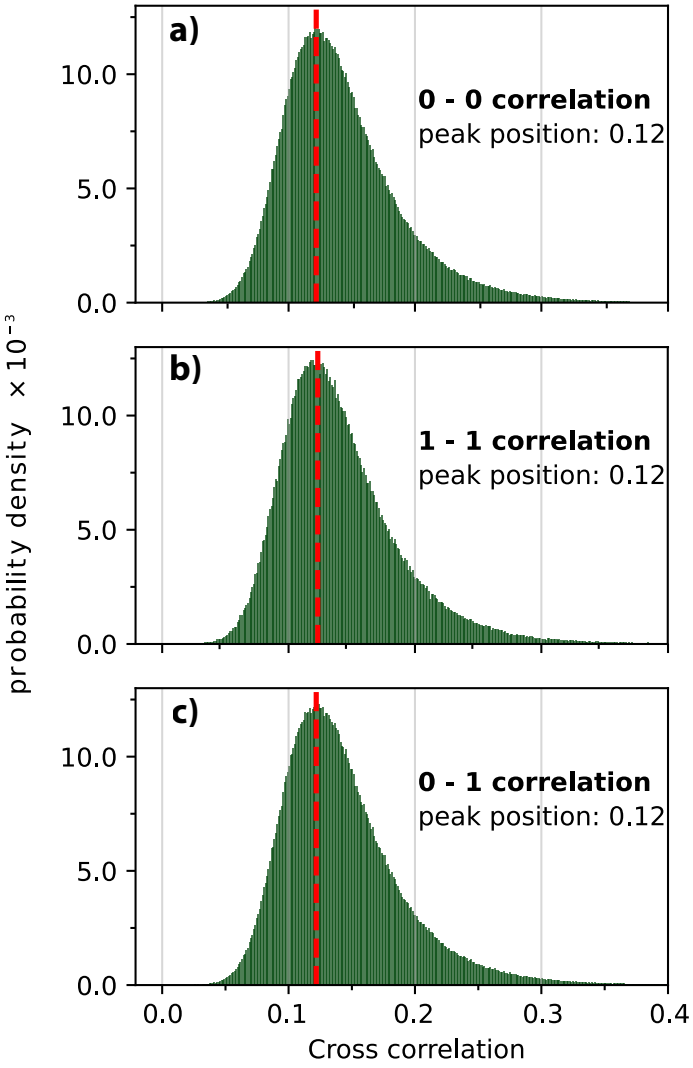

Figure 7.5: Probability density histograms of speckle cross-correlation between different signals: a) between all pairs of speckle patterns belonging to state 0, b) between all pairs of speckle patterns belonging to state 1, and c) between speckle patterns from state 0 and speckle patterns from state 1. The vertical dashed red lines indicate the peaks of the distributions.

Table 7.3: Balanced classification accuracy of the unsupervised methods under study.

Method	Average (%)	STD (%)	0's predicted (%)
K-Means	51	4.07	50
Hierarchical	49	7.58	50
K-means no PCA	49	2.52	50
Hierarchical no PCA	50	0.00	100

To get statistical information from the classification, each method is repeated 5 times with sub-groups of half of the data. Furthermore, for each sub-group, we repeat 5 more times to average over the initial random guess of the algorithms. Note that we select an equal number of speckle patterns from both groups, $N_{W,0} = N_{W,1} = 1774$, so the data is evenly distributed between the two groups. Table 7.3 presents the balanced accuracy of the classification algorithms. The balanced accuracy is an average between the true positive rate (TPR) and true negative rate (TNR), which is the rate of predicted versus the total amount of positives and negatives, respectively [160]. In our case, positive and negative represent a binary 0 and a binary 1. We see that the balanced accuracy of all the methods we used is around 50%. As this is a binary classification and only two options are possible, a random classifier yields on average the same accuracy of 50%. This shows that the classification is as effective as tossing a coin, thus we obtain no new information from it. Furthermore, the right column of Table 7.3 shows the percentage of 0's predicted by the clustering. For the last method, all the data points were classified as 0, which also yields 50% accuracy. All the other methods separate the data exactly in half for every sub-group and every repetition.

We thus find that there are no trivial correlations between intermediate speckle patterns, regardless of their corresponding encoded message. Furthermore, the different unsupervised classification algorithms are not able to find any correlation or separation between the patterns. This means that when measuring two intermediate speckle patterns, is not possible to know for certain if they are encoding the same message or not in the final speckle pattern. We believe that this knowledge is relevant for applications, particularly in the field of optical wireless communication (OWC), to make communication more secure. Therefore, in the following section, we described a possible implementation of a communication link based on these findings.

7.6 Proposed communication scheme

Based on the described scenario, we propose a new communication scheme based on two layers of physical unclonable functions (PUFs). This scheme is depicted in Fig. 7.6, which is inspired by the experimental setup shown in Fig. 7.2. Alice sends a message to Bob through free space using visible or infrared coherent light. The initial digital message is encoded as a phase-modulated wavefront that is encrypted by the first PUF. When arriving at the destination, the signal passes

through a second PUF, and the message is recovered as light intensity by Bob. If an attacker, depicted in Figure 7.6 as Eve, intercepts the signal, the message will not be recovered as the second PUF is not known. Similarly, if Eve tries to send a false message to Bob, this will not be considered as it does not pass through the first PUF.

The secrecy of the proposed system relies on the lack of correlation between speckle patterns, as demonstrated before. If for every binary message, the sender randomly selects one wavefront from a large library with many options, the attacker is not able to separate which speckle patterns are related to a state 0 and which ones are to a state 1. The proposed system is also resilient for an attacker to send false messages or store the message for future decryption. This is thanks to the first PUF, which scrambles the incoming wavefront. If the first PUF is not present, the attacker has access to the incident wavefront and they can measure, store, and replicate it. This is not challenging because the spatial complexity of the incident wavefront is limited by the spatial resolution of the modulator. Inversely, if the first scattering layer is present, the attacker only has access to the intermediate speckle, which has a much larger spatial complexity and it is highly challenging to record with all its properties and fluctuations [149]. Furthermore, if the attacker wants to send a false message, they will need a modulator device or optical system able to replicate the intermediate speckle pattern with high resolution in order to result in the proper final speckle pattern.

If the digital codification of the message forces Alice to repeat a specific bit on a predictable basis, *e.g.*, for identification, Eve can record the speckle of these bits to identify each binary 0 and binary 1. In this case, the number of messages Eve needs to record to obtain all speckles grows as $\mathcal{O}(N_{\mathrm{W}} log(N_{\mathrm{W}}))$ [161]. An implementation without this identification is possible by changing the digital codification to avoid any predictable bit. Even more, based on the complexity of the scattering material and the degrees of freedom at the wavefront modulation, the number of available wavefronts can be made arbitrarily large, increasing the number of messages needed. This also limits Eve to send a false message to Bob.

Many alternatives have been studied to break the secrecy of PUFs employ Machine Learning (ML) techniques, which have proved to be powerful tools for these attacks [162, 163], at a large expense of time and digital memory from the side of the attacker. In most of these studies, however, they needed to obtain a Challenge-Response Pair (CRP) set for training a supervised algorithm. To do so, it is assumed that Eve can send a challenge to the PUF and read the response. In our case, the CRP corresponds to the system characterization shown in Section 7.3. We obtain all the CRP sets offline and prior to the communication link, as it is end-to-end encryption. Obtaining a CRP set means that Eve has a subset of speckle patterns at CCD2 with their respective classification at CCD1. In our system, an attacker does not have access to the space between the second PUF and CCD1, and gaining access for an invasive measurement poses a threat larger than eavesdropping, thus we disregard such attacks in this study. If Eve does not have a CRP set, there are no training data for a supervised algorithm. Therefore, we do not consider the use of supervised classification methods to be a realistic scenario.

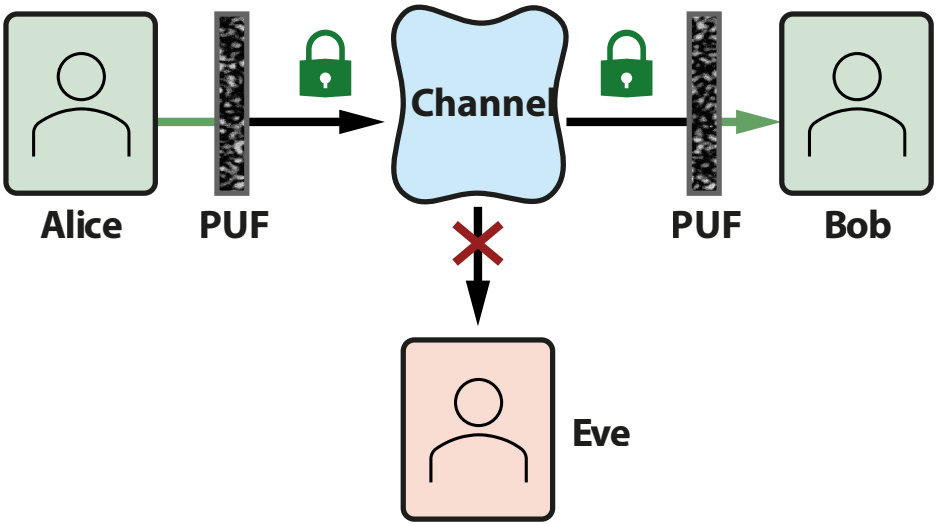

Figure 7.6: Scheme of the communication link. Alice sends a message to Bob through the channel (free-space), which is encrypted using two Physical Unclonable Functions (PUF).

Nevertheless, an attacker may try to classify the speckle patterns using unsupervised algorithms. The results from Section 7.5 show that none of the tested unsupervised methods are significantly better than a random classification, which suggests that the data are not classifiable given the intensity speckle pattern obtained from the channel. Hence, the communication is secure against an attacker in free-space.

7.7 Applications and limitations

We initially envision our scheme in an indoor communication scenario as a one-way communication. A central device would include the modulator device with the first PUF layer, and the receiving device would have a pair of photodiodes representing the regions of interest ROI A and ROI B, with its own integrated PUF. In this system, the central device can send many messages to different devices using different wavefronts, while the receiver is an inexpensive and fast device. The calibration can be done for specific positions of the receiver, *e.g.*, cubicles in an open office. If the layout is not changed, the calibration only needs to occur once per device. We believe our method opens many possibilities to both test the applicability of the scheme, and study the scattering properties of complex media.

Several questions and limitations arise from our system, which need to be addressed to scale up this scheme. One limitation of our scheme is the bit rate. If only two ROIs are considered, the receiver can consist of two fast photodiodes, thus not limiting the speed. The bottleneck arises from the refresh rate of the

DMD, which for our DMD model is around 20 kHz. This limitation can be remedied by sending multiple bits in one wavefront (*e.g.*, sending 50,000 bits per image results in 1Gbit/s). In this scenario, the camera at the receiver is needed, which will limit the speed as well. Another solution for higher speed is using another faster modulation technique, like Free-Space Electro-Optic Modulators, which can get up to 100 MHz [164].

Another limitation of our system is the source. The need to have a coherent light source hinders us from extending our technique to applications such as light fidelity (Li-Fi). This restriction is present in any technology that wants to take advantage of luminaries already installed. Nevertheless, it has been demonstrated that modulation techniques such as WFS are applicable to LED sources [165]. Extending our method to LED sources would simplify the architecture. Furthermore, it was recently demonstrated that is possible to use a random material as a PUF having a screen projector as a source [166], which is a commercial combination between an ultra-high-performance (UHP) lamp, which is incoherent, and a DMD.

Since our system is based on light scattering, it may be highly sensitive to noise, misalignment, or additional scattering events. This sensitivity depends on the power of the signal, the distance, and the dynamics of the medium. Importantly, we use a diffuser with around 80% of transmission and a collimating lens, so the use of PUFs does not drastically increase the losses of the system. This suggests that the restrictions on noise and power are similar to any OWC scheme. Furthermore, if the PUF is static and reliable, the dynamics of the medium may fall under the memory effect of the system. It remains to be tested to what extent these factors limit the applicability of the scheme.

In case the medium changes significantly or we want to extend this to moving users, the calibration needs to be done online. One way of implementing this is adding a secondary classical channel where the users can share the CRP. More studies are needed to test the secrecy of such implementation.

Finally, the main advantage of our system is that the secrecy is imposed by the number of measurements needed from an attacker to learn the message. This is more restrictive than only computational power, as traditional digital encryption. While the results presented in this manuscript indicate no correlation between the signal retrieved by the attacker and the final message, it is important to acknowledge that it is impossible to account for all possible scenarios that could potentially benefit the attacker.

For future tests, we conceive that an attacker may benefit from other detection configurations that may give more information. We think of at least three possible extensions to the proposed detection configuration: (a) measure the complex information of the speckle (both amplitude and phase), (b) measure in the conjugated plane of the sample, and (c) measure the reflective speckle from the receiver PUF. The reflective speckle pattern is particularly relevant, as it has been successfully used in imaging through scattering media [65, 167, 168]. It has been proven that the reflective speckle pattern has a certain correlation with the transmitted speckle pattern [169], similar to the correlations between the incident and transmitted wavefront mentioned before and may prove useful

to decipher the message in our communication scheme. Because we calibrate the system beforehand, if the commented configurations give useful information to the attacker (*e.g.*, the reflection-transmission correlations), we believe it is possible to account for it beforehand by filtering further which available wavefronts are available to send the message. Furthermore, from the practical point of view, one attractive part of the present scheme is that the detection of the message by the receiver can be done easily, fast, and cheaply. This is because the receiver only needs two photodiodes to measure the average intensity. In turn, the commented possible configurations impose high technical difficulties. Further studies are needed to evaluate how obtaining this new information may affect the secrecy of the scheme.

7.8 Conclusion

In this chapter, we have studied the correlation between speckle patterns when passing through multiple slabs of scattering media. We spatially modulate the phase of the incoming light and we send a signal through two diffusers, measuring the resulting speckle pattern both between and after the two diffusers. The signal is encoded as changes in light intensity at two regions of interest (ROI) at the receiver, where multiple modulated incoming wavefronts may result in the same message. We have studied the correlation between speckle patterns when sending different messages. Therefore, we use the Pearson correlation coefficient and two unsupervised classification algorithms. In all cases, we observe that there is no correlation between the intermediate speckle pattern and the resulting pattern (or message). This method is attractive for optical wireless communication (OWC) schemes, particularly in line-of-sight communication and wireless indoor communication.

The experimental data from our experiments are available in the Zenodo base [170].

Chapter 8

Summary and Outlook

8.1 Summary

In this thesis, we study various wavefront modulations of light for various scientific and applied purposes and scenarios. In summary, the thesis can be distinguished into three projects, where we apply wavefront modulation to 1) study mutual scattering in depth, 2) test the performance of the wavefront shaping technique (WFS), and 3) study speckle correlation for applications in visible light communication (VLC). Modulating the wavefront of light incoming into a complex media is a powerful tool for understanding and controlling light propagation within the media. This technique applies to highly random materials, such as paper, clouds, or biological tissue. Moreover, it is also applicable to structured materials, such as photonic crystals or integrated circuits. Several techniques and active devices can be utilized to modulate the wavefront, such as spatial light modulators (SLM), digital micromirror devices (DMD), metamaterials, deformable mirrors, electro-optic modulators, and many more.

The main project of this thesis is dedicated to mutual scattering, which is covered in Chapters 2 to 5. This thesis presents the first experimental observation of mutual scattering and its first application in light scattering characterization of complex media. Mutual scattering occurs when two or more incoming beams cross in a finite object, and it is the cross-interference between the coherent incident wave of one beam and the scattered wave generated by the other beam. In our experiments, we modulate the incoming beams to change their relative angle and phase, thereby controlling and characterizing the scattering properties of the object.

Besides measuring mutual scattering, we apply WFS in free-form objects (Chapter 6). In this project, we intend to defy the standard approach to light scattering in complex media, where the geometry of the object under study is considered a *slab*. Surprisingly, although WFS is assumed to apply to any scattering media, other geometries have yet to be explored. In this project, we demonstrate

that WFS is equally effective in a free-form sample as in a slab geometry, thus confirming our hypothesis.

Last but not least, we explore wavefront modulation in a VLC system (Chapter 7), utilizing the properties of complex scattering media for encryption purposes. To achieve this, we employ a scattering layer as a physical unclonable function (PUF), which serves as an additional security layer in the system. We expand on previously studied situations by incorporating *two* scattering layers, one at the emitter and the other at the receiver. This approach aims to prevent a person-in-the-middle attack, where an attacker intercepts the communication between the emitter and the receiver. The scattering layer at the emitter stops the attacker from exactly copying the source message, and the scattering layer at the receiver stops the attacker from understanding the message and avoids jamming attacks. Moreover, the complexity of the system allows for thousands of available wavefronts to send the same message. The emitter can alternate between the available wavefronts without any added expense, making it exceedingly difficult for an attacker to decipher the message.

The experimental results of wavefront modulation presented throughout this thesis may be further extended and improved. In the next section, we outline a few possible directions for further research.

8.2 Next steps in mutual scattering experiments

8.2.1 Sample fabrication & phase calibration

Mutual scattering is a recent discovery, and its theory is still developing. Its potential impact on the field remains unknown. There is much room for improvement in the current experiments on mutual scattering and many exciting new experiments to explore.

As discussed in Chapter 2, one limitation of current experiments is the phase ϕ calibration for different angles γ. Changing the angle γ induces a change in the path length and, consequently, an extra phase change. We presented a preliminary model for the induced phase change in Chapter 2. This model depends on several known parameters, such as the thickness and refractive index of the protective layer of the camera and the refractive index of the PDMS where the samples are located. However, it also depends on several unknown parameters, such as the tilt of the camera, the tilt and thickness of the PDMS, and any aberration induced by the DMD. An in-depth study of phase calibration is necessary to fully understand the causes and solutions of the phase changes.

The sample fabrication process must also be improved to better understand mutual scattering. Currently, the dimension of the samples is within a range too small to see comfortably with the naked eye but too large to fabricate using standard nano-fabrication techniques. Due to a lack of expertise, the fabrication of the sample is currently not reproducible, and parameters such as the thickness of the PDMS or the orientation of the sample within the PDMS are unknown. Switching to a reproducible and reliable procedure, such as mechanized fabrication methods, is crucial for future experiments. Understanding the characteristics

of a test sample, such as a dielectric sphere, including the surrounding medium, is essential for accurately comparing theory and experiments and distinguishing between noise and speckle.

8.2.2 Limits of diffraction approximation

In Chapter 3, we deliberately avoided mentioning diffraction theory and making a comparison between diffraction and mutual scattering. This decision was based on our belief that the fundamental differences between diffraction and mutual scattering are mistakenly disregarded when the reader realizes that the angular dependency of mutual scattering is explained relatively accurately by diffraction theory. However, it is essential to note that in diffraction theory, we assume a perfectly absorbing, infinitely extended thin screen [54, 97]. Moreover, to calculate the diffraction pattern of a finite object, we use the Babinet principle [85, 171], which uses a rather heuristic factor, called *obliquity factor*[172].

After further developments in the theory of mutual scattering, we concluded that everything boils down to the scattering amplitude f of the sample [134]. For example, a beamsplitter has a distinct scattering amplitude composed only of delta functions in the forward and reflected directions. If the sample satisfies the assumptions of diffraction theory, then the scattering amplitude can be described with diffraction theory. However, as the assumptions of diffraction are unphysical, deviations from theory are expected. The same is valid for Mie scattering calculations; if the sample satisfies the assumptions of Mie scattering, then the scattering amplitude is described by Mie calculations.

An interesting experiment to compare diffraction and mutual scattering is to test the limits of the assumptions of diffraction, *i.e.*, measure mutual scattering while changing either the sample thickness L or the absorption mean free path l_a. Ideally, when $(L, l_\mathrm{a}) \to 0$, the mutual scattering measurements are fully described by diffraction, and by increasing L or l_a, the experimental result starts to deviate from diffraction theory. To achieve this experimentally, a tunable laser can be used. We need a sample for which, for a certain range of wavelengths, l_a is highly dependent on the wavelength λ, so l_a changes without significantly changing the ratio $L : \lambda$. At the same time, we need another wavelength range where l_a is weakly dependent on the wavelength λ, so the ratio (L/λ) changes without changing l_a.

A possible implementation is to use our readily available tunable laser MBR-110, a Ti:Sapphire laser with a tunable wavelength from 780nm (1.66 eV) to 870nm (1.49eV), which is available at the COPS labs. To fabricate the sample, a bar of AlGaAs is a promising candidate. GaAs has a wavelength range where l_a has a high dependence on λ [173]. By engineering the proportion between AlAs and GaAs, an AlGaAs alloy may have the desired dependency in the corresponding wavelength range.

8.2.3 Fluorescence modulation

Modulating the light extinction of an object means controlling both light scattering and absorption. Because previous techniques rely mainly on controlling light scattering, controlling light absorption is a promising application of the mutual scattering effect. However, many unanswered questions remain about the process, such as how deep inside the object we can effectively control absorption.

A follow-up experiment to those presented in this thesis is to measure the mutual scattering of a fluorescent object. The emitted fluorescence of the object is dependent on the amount of light it absorbs, so by measuring the fluorescence, we can observe the modulation of light absorption. Additionally, various samples can be designed, such as fluorescent particles with different emitting wavelengths throughout the sample, to investigate the depth of absorption modulation.

8.2.4 Relevance of mutual scattering to CMOS industry

In Chapter 3, we mentioned that the angular dependency of mutual scattering gives information about the width and shape of the sample. Truong *et al.* [71] showed how mutual scattering is capable of sensing the position of a single scatterer inside an object filled with identical scatterers. Thus, mutual scattering promises to be a powerful tool to detect the shape and position of nano-objects, even when the nano-object is surrounded by other objects made of the same material, which is usually the case in silicon nano-fabrication.

Because of the high refractive index of silicon of $n > 3.5$ and the ever-decreasing size of nano-fabrication structures of the order of nanometers, we may consider a nano-object as a single scatterer. The procedure of Ref. [71] allows us to detect with high sensitivity the change in position of a single nanostructure, while the procedure of Chapter 3 allows us to detect the width of the nanostructure.

8.3 Measuring the free-form memory effect

In Chapter 6, we presented a comparison of the performance of wavefront shaping (WFS) on a flat and a curved sample. We believe these results contribute towards observing what we call the *free-form memory effect*.

Light scattering materials are highly complicated, and the interferences that give rise to the speckle pattern are due to a high number of degrees of freedom present in the sample. It is reasonable to assume that a slight change in the sample will lead to an entirely different speckle pattern. However, multiple studies [39, 40] have observed that a correlation in the speckle pattern persists even when specific properties are slightly changed. This phenomenon is known as the memory effect and has been investigated by altering the incident beam's angle, position on the sample, and wavelength [17, 20, 41, 42].

Following the results presented in Chapter 6, we are interested in studying how the enhancement of WFS and the speckle correlation change when the shape of the sample is *continuously* changed. We expect the speckle pattern to preserve

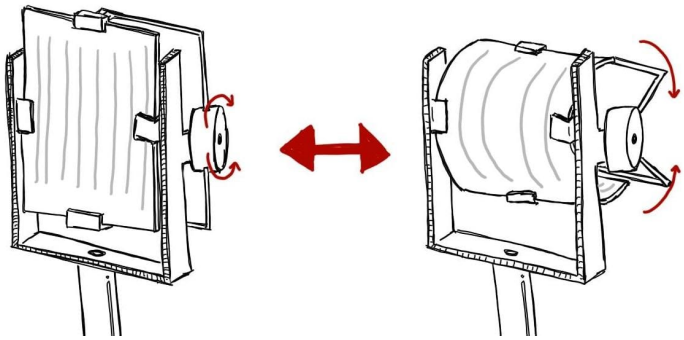

Figure 8.1: Simple sketch for automated sample holder. A stepper motor with two arms is attached to the side of the holder to open and close with moves similar to the ones of a scissor.

some correlation for slight changes in shape, similar to the memory effect when changing other properties. Thus, we call this the free-form memory effect.

We need an automated sample holder capable of continuously curving the sample to achieve this goal. A possible design for the holder is shown in Fig. 8.1. We can measure the speckle pattern and perform wavefront shaping experiments with the same samples and experimental setup as in our previous experiments. The experimental setup can be even more straightforward if only speckle correlation is needed. Additionally, new materials can be explored to induce more significant changes than just curvature. Shape-shifting smart materials are one example, which can morph in a controlled manner using stimuli like heat, voltage, or even light [174–176]. Another approach to studying speckle correlation is to change the porosity of an object by applying tension.

8.4 Physical limit of secrecy in scattering-based communication link

8.4.1 Parallel channels in scattering-based communication link

In Chapter 7, we propose a visible light communication (VLC) scheme that employs two scattering layers for encryption as physical unclonable functions (PUF). The proposed scheme uses two regions of interest (ROI), namely spot A and spot B, to send a single bit per wavefront. Specifically, a binary 0 is sent when spot A has high intensity and spot B has low intensity. In contrast, binary 1 is sent when spot A has low intensity and spot B has high intensity. Apart from the scramble of information caused by scattering, the secrecy of the system relies on the capability to modulate a large number of different wavefronts to transmit the same message, thereby making it incredibly challenging for an adversary to decipher the actual message.

The main limitation of the proposed scheme is the bit rate, as we can only

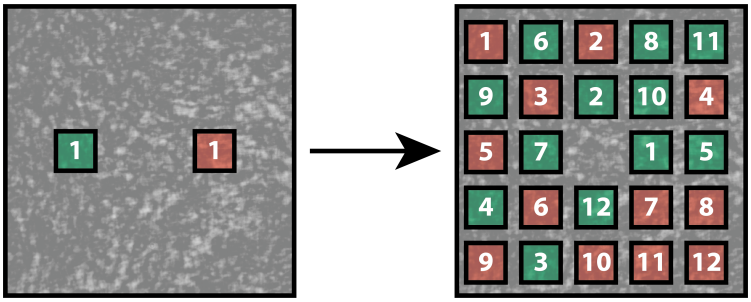

Figure 8.2: Current design (left) and new design (right) for the receiver. Instead of sending 1 bit, we are sending multiple bits exploiting the 2D nature of the speckle pattern.

send a single bit per wavefront with a refresh rate of < 10kHz. As a follow-up, we aim to improve the communication scheme by not only using two regions of interest for the receiver but using the whole speckle pattern measured by a camera. This would allow us to send multiple messages in parallel. In such a project, we must investigate its feasibility, such as determining the maximum number of ROI we can activate simultaneously to maintain a sufficiently large set of wavefronts for secure communication. Importantly, using multiple ROI already increases the secrecy of the system, as the attacker now faces a broader range of message combinations rather than just two possibilities per message.

An illustration of the proposed new receiver design is given in Fig. 8.2. The number of bits we can send depends on various factors, such as the resolution of the camera, the speckle size, and the amount of available wavefronts. In the diagram of Fig. 8.2, we placed the multiple bits of the new design in random positions. With this, we aim to avoid any spatial correlation the sample may have.

8.4.2 Secrecy limit in scattering-based communication link

In Chapter 7, we study the correlations of a multi-layer system. We claim that if the emitter sends binary messages alternating the wavefront from a pool of many (thousands) of wavefronts, there is no way to intercept the message if we only measure the speckle generated in the middle between the two layers. A future step of this project is to test this idea to the limit.

We define a target vector[1] A_{ref}, B_{ref}. Suppose a scattering object is represented by its transmission matrix $T \in \mathbb{C}^{n \times n}$. We define $\mathbb{A}$ as the set of incoming wavefronts that, after being multiplied by the transmission matrix T, have a high correlation with the target vector $\mathbb{A}$:

$$\mathbb{A} = \{x \in \mathbb{C}^n \mid \text{corr}\,(Tx, A_{\text{ref}}) > c\}\,, \tag{8.1}$$

$$\tag{8.2}$$

[1]This target vector can be, for instance, the ROI used in Chapter 7.

with corr(·) the correlation function, and c the target correlation value. We want c to be close to one, but it can have any value between -1 and 1. Considering this, and considering the physical properties of the transmission matrix (*e.g.*, C_1, C_2, and C_3 correlations [128, 177]), we wonder if we can answer the following questions:

1. Knowing the target matrix A_{ref} and all the wavefronts belonging to the set $\mathbb{A}$. Is it possible to recover the transmission matrix T?

2. Can we obtain the transmission matrix T from a sub-set of $\mathbb{A}$? If so, How small this sub-class can be?

3. Let's say we have a second target vector B_{ref}, such that it is completely uncorrelated with the first target vector, $\text{corr}\left(A_{\text{ref}}, B_{\text{ref}}\right) = 0$. Similar to $\mathbb{A}$, we define the set of incoming wavefronts that, after being multiplied by the transmission matrix T, have a high correlation with the target vector $\mathbb{B}$:

$$\mathbb{B} = \{x \in \mathbb{C}^{\text{n}} \mid \text{corr}\left(Tx, B_{\text{ref}}\right) > c, \}\,, \tag{8.3}$$

   Knowing the target vectors A_{ref}, B_{ref} and knowing all the wavefronts from the joint set $\mathbb{D} = \mathbb{A} \cup \mathbb{B}$, is it possible to differentiate if a wavefront $x \in \mathbb{D}$ belongs to either $\mathbb{A}$ or $\mathbb{B}$?

Furthermore, it is interesting to study the relation between the number of ROI at the receiver and the number of available wavefronts to send a bit, and thus study the limiting number of parallel bits we can send to maintain the secrecy of the channel.

Bibliography

[1] J. van Zuylen. "The microscopes of Antoni van Leeuwenhoek". In: *Journal of Microscopy* 121.3 (1981), pp. 309–328. DOI: https://doi.org/10.1111/j.1365-2818.1981.tb01227.x. eprint: https://onlinelibrary.wiley.com/doi/pdf/10.1111/j.1365-2818.1981.tb01227.x. URL: https://onlinelibrary.wiley.com/doi/abs/10.1111/j.1365-2818.1981.tb01227.x (cit. on p. 12).

[2] G. Andersen. *The telescope: Its history, technology, and future*. Princeton University Press, 2007 (cit. on p. 12).

[3] K. Kikuchi. "Fundamentals of Coherent Optical Fiber Communications". In: *Journal of Lightwave Technology* 34.1 (2016), pp. 157–179. DOI: 10.1109/JLT.2015.2463719 (cit. on p. 12).

[4] A. Ishimaru. "Part II: Applications". In: *Electromagnetic Wave Propagation, Radiation, and Scattering*. John Wiley & Sons, Ltd, 2017. ISBN: 9781119079699. DOI: https://doi.org/10.1002/9781119079699.fmatter. URL: https://onlinelibrary.wiley.com/doi/abs/10.1002/9781119079699.fmatter (cit. on p. 12).

[5] P. W. Anderson. "More Is Different". In: *Science* 177.4047 (1972), pp. 393–396. DOI: 10.1126/science.177.4047.393. URL: https://www.science.org/doi/abs/10.1126/science.177.4047.393 (cit. on p. 12).

[6] L. Wang, T. Tschudi, T. Halldórsson, and P. R. Pétursson. "Speckle reduction in laser projection systems by diffractive optical elements". In: *Appl. Opt.* 37.10 (1998), pp. 1770–1775. DOI: 10.1364/AO.37.001770. URL: http://opg.optica.org/ao/abstract.cfm?URI=ao-37-10-1770 (cit. on p. 14).

[7] J. I. Trisnadi. "Hadamard speckle contrast reduction". In: *Opt. Lett.* 29.1 (2004), pp. 11–13. DOI: 10.1364/OL.29.000011. URL: http://opg.optica.org/ol/abstract.cfm?URI=ol-29-1-11 (cit. on p. 14).

[8] M. B. van der Mark, M. P. van Albada, and A. Lagendijk. "Light scattering in strongly scattering media: Multiple scattering and weak localization". In: *Phys. Rev. B* 37.7 (1988), pp. 3575–3592. DOI: 10.1103/PhysRevB.37.3575. URL: https://link.aps.org/doi/10.1103/PhysRevB.37.3575 (cit. on p. 14).

[9] D. S. Wiersma. "Disordered photonics". In: *Nat. Photonics* 7.3 (2013), pp. 188–196. DOI: 10.1038/nphoton.2013.29. URL: https://doi.org/10.1038/nphoton.2013.29 (cit. on pp. 14, 48, 62).

[10] COPS Chair. *Complex Photonic Systems (COPS)*. https://nano-cops.com/. (Visited on 07/21/2023) (cit. on p. 15).

[11] M. B. van der Mark. “Propagation of light in disordered media: A search for Anderson localization”. PhD thesis. Netherlands: Universiteit van Amsterdam, 1990 (cit. on p. 15).

[12] J. Gómez Rivas. “Light in strongly scattering semiconductors: diffuse transport and Anderson localization”. PhD thesis. Netherlands: Universiteit van Amsterdam, 2002. ISBN: 90-5776-082-7. URL: https://hdl.handle.net/11245/1.201630 (cit. on p. 15).

[13] B. Bret. “Multiple light scattering in porous gallium phosphide”. PhD thesis. Netherlands: University of Twente, 2005. ISBN: 90-365-2196-3. DOI: 10.3990/1.9789036521963. URL: https://doi.org/10.3990/1.9789036521963 (cit. on p. 15).

[14] Vellekoop and I. M. “Controlling the propagation of light in disordered scattering media”. PhD thesis. Netherlands: University of Twente, 2008. ISBN: 978-90-365-2663-0. DOI: 10.3990/1.9789036526630. URL: https://doi.org/10.3990/1.9789036526630 (cit. on pp. 15, 16, 17).

[15] D. Akbulut. “Measurements of strong correlations in the transport of light through strongly scattering materials”. PhD thesis. Netherlands: University of Twente, 2013. ISBN: 978-94-6108-491-0. DOI: 10.3990/1.9789461084910. URL: https://doi.org/10.3990/1.9789461084910 (cit. on pp. 15, 16).

[16] O. S. Ojambati. “Stirring of the propagation and the absorption of light in complex nanophotonic systems”. PhD thesis. Netherlands: University of Twente, 2016. ISBN: 978-90-365-4202-9. DOI: 10.3990/1.9789036542029. URL: https://doi.org/10.3990/1.9789036542029 (cit. on p. 15).

[17] M. Adhikary. “Controlled light propagation in random, periodic, and superperiodic silicon nanophotonic materials”. English. PhD thesis. Netherlands: University of Twente, 2021. ISBN: 978-90-365-5236-3. DOI: 10.3990/1.9789036552363 (cit. on pp. 15, 98, 122).

[18] O. Akdemir. “Light transport in anisotropically scattering and absorbing media”. PhD thesis. Netherlands: University of Twente, 2023. ISBN: 978-90-365-5780-1. DOI: 10.3990/1.9789036557801. URL: https://doi.org/10.3990/1.9789036557801 (cit. on pp. 15, 19).

[19] A. Lagendijk and B. A. van Tiggelen. “Resonant multiple scattering of light”. In: *Physics Reports* 270.3 (1996), pp. 143–215. ISSN: 0370-1573. DOI: https://doi.org/10.1016/0370-1573(95)00065-8. URL: https://www.sciencedirect.com/science/article/pii/0370157395000658 (cit. on pp. 16, 20, 22, 63, 71).

[20] M. C. W. van Rossum and T. M. Nieuwenhuizen. “Multiple scattering of classical waves: microscopy, mesoscopy, and diffusion”. In: *Rev. Mod. Phys.* 71.1 (1999), pp. 313–371. DOI: 10.1103/RevModPhys.71.313. URL: https://link.aps.org/doi/10.1103/RevModPhys.71.313 (cit. on pp. 16, 17, 19, 20, 48, 51, 62, 96, 98, 104, 106, 122).

[21] R. H. J. Kop, P. de Vries, R. Sprik, and A. Lagendijk. “Observation of Anomalous Transport of Strongly Multiple Scattered Light in Thin Disordered Slabs”. In: *Phys. Rev. Lett.* 79.22 (1997), pp. 4369–4372. DOI: 10.1103/PhysRevLett.79.4369. URL: https://link.aps.org/doi/10.1103/PhysRevLett.79.4369 (cit. on p. 16).

[22] O. L. Muskens and A. Lagendijk. “Method for broadband spectroscopy of light transport through opaque scattering media”. In: *Opt. Lett.* 34.4 (2009), pp. 395–397. DOI: 10.1364/OL.34.000395. URL: https://opg.optica.org/ol/abstract.cfm?URI=ol-34-4-395 (cit. on p. 16).

[23] T. van der Beek, P. Barthelemy, P. M. Johnson, D. Wiersma, and A. Lagendijk. “Light transport through disordered layers of dense gallium arsenide submicron particles”. In: *Phys. Rev. B* 85.11 (2012). DOI: 10.1103/PhysRevB.85.115401 (cit. on p. 16).

[24] W. L. Vos, T. W. Tukker, A. P. Mosk, A. Lagendijk, and W. L. IJzerman. “Broadband mean free path of diffuse light in polydisperse ensembles of scatterers for white light-emitting diode lighting”. In: *Appl. Opt.* 52.12 (2013), pp. 2602–2609. DOI: 10.1364/AO.52.002602. URL: https://opg.optica.org/ao/abstract.cfm?URI=ao-52-12-2602 (cit. on p. 16).

[25] J. P. Rolland, M. A. Davies, T. J. Suleski, C. Evans, A. Bauer, J. C. Lambropoulos, and K. Falaggis. “Freeform optics for imaging”. In: *Optica* 8 (2021), pp. 161–176. DOI: 10.1364/OPTICA.413762. URL: https://opg.optica.org/optica/abstract.cfm?URI=optica-8-2-161 (cit. on p. 16).

[26] J. C. M. Roland Winston and P. Benítez. *Nonimaging Optics*. English. Burlington: Academic Press, 2005. ISBN: 978-0-12-759751-5. DOI: https://doi.org/10.1016/B978-0-12-759751-5.X5000-3 (cit. on pp. 16, 20, 92).

[27] F. Fang, X. Zhang, A. Weckenmann, G. Zhang, and C. Evans. “Manufacturing and measurement of freeform optics”. In: *CIRP Annals* 62.2 (2013), pp. 823–846. DOI: https://doi.org/10.1016/j.cirp.2013.05.003. URL: https://www.sciencedirect.com/science/article/pii/S0007850613001935 (cit. on pp. 16, 92).

[28] C. W. J. Beenakker. “Random-matrix theory of quantum transport”. In: *Rev. Mod. Phys.* 69.3 (1997), pp. 731–808. DOI: 10.1103/RevModPhys.69.731. URL: https://link.aps.org/doi/10.1103/RevModPhys.69.731 (cit. on pp. 16, 21, 45, 62, 104, 106).

[29] T. Kohlgraf-Owens and A. Dogariu. “Finding the field transfer matrix of scattering media”. In: *Opt. Express* 16.17 (2008), pp. 13225–13232. DOI: 10.1364/OE.16.013225. URL: http://opg.optica.org/oe/abstract.cfm?URI=oe-16-17-13225 (cit. on pp. 16, 45, 62, 104).

[30] D. A. B. Miller. “Waves, modes, communications, and optics: a tutorial”. In: *Adv. Opt. Photon.* 11.3 (2019), pp. 679–825. DOI: 10.1364/AOP.11.000679. URL: https://opg.optica.org/aop/abstract.cfm?URI=aop-11-3-679 (cit. on pp. 16, 106).

[31] E. P. Wigner. “On the statistical distribution of the widths and spacings of nuclear resonance levels”. In: *Mathematical Proceedings of the Cambridge Philosophical Society* 47.4 (1951), pp. 790–798. DOI: 10.1017/S0305004100027237 (cit. on pp. 16, 20, 98).

[32] T. Guhr, A. Müller–Groeling, and H. A. Weidenmüller. “Random-matrix theories in quantum physics: common concepts”. In: *Physics Reports* 299.4 (1998), pp. 189–425. DOI: https://doi.org/10.1016/S0370-1573(97)00088-4. URL: https://www.sciencedirect.com/science/article/pii/S0370157397000884 (cit. on pp. 16, 20, 98).

[33] K. L. van der Molen, R. W. Tjerkstra, A. P. Mosk, and A. Lagendijk. "Spatial Extent of Random Laser Modes". In: *Phys. Rev. Lett.* 98 (14 2007), p. 143901. DOI: 10.1103/PhysRevLett.98.143901. URL: https://link.aps.org/doi/10.1103/PhysRevLett.98.143901 (cit. on pp. 16, 20, 98).

[34] O. Dorokhov. "On the coexistence of localized and extended electronic states in the metallic phase". In: *Solid State Communications* 51.6 (1984), pp. 381–384. DOI: https://doi.org/10.1016/0038-1098(84)90117-0. URL: https://www.sciencedirect.com/science/article/pii/0038109884901170 (cit. on pp. 17, 104).

[35] P. Mello, P. Pereyra, and N. Kumar. "Macroscopic approach to multichannel disordered conductors". In: *Annals of Physics* 181.2 (1988), pp. 290–317. ISSN: 0003-4916. DOI: https://doi.org/10.1016/0003-4916(88)90169-8. URL: https://www.sciencedirect.com/science/article/pii/0003491688901698 (cit. on pp. 17, 104).

[36] Y. Imry. "Active Transmission Channels and Universal Conductance Fluctuations". In: *Europhysics Letters* 1.5 (1986), p. 249. DOI: 10.1209/0295-5075/1/5/008. URL: https://dx.doi.org/10.1209/0295-5075/1/5/008 (cit. on pp. 17, 104).

[37] J. B. Pendry, A. MacKinnon, and A. B. Prêtre. "Maximal fluctuations — A new phenomenon in disordered systems". In: *Physica A: Statistical Mechanics and its Applications* 168.1 (1990), pp. 400–407. ISSN: 0378-4371. DOI: https://doi.org/10.1016/0378-4371(90)90391-5. URL: https://www.sciencedirect.com/science/article/pii/0378437190903915 (cit. on pp. 17, 104).

[38] B. Shapiro. "Large Intensity Fluctuations for Wave Propagation in Random Media". In: *Phys. Rev. Lett.* 57.17 (1986), pp. 2168–2171. DOI: 10.1103/PhysRevLett.57.2168. URL: https://link.aps.org/doi/10.1103/PhysRevLett.57.2168 (cit. on pp. 17, 104).

[39] I. Freund, M. Rosenbluh, and S. Feng. "Memory Effects in Propagation of Optical Waves through Disordered Media". In: *Phys. Rev. Lett.* 61.20 (1988), pp. 2328–2331. DOI: 10.1103/PhysRevLett.61.2328. URL: https://link.aps.org/doi/10.1103/PhysRevLett.61.2328 (cit. on pp. 17, 93, 98, 104, 122).

[40] S. Feng, C. Kane, P. A. Lee, and A. D. Stone. "Correlations and Fluctuations of Coherent Wave Transmission through Disordered Media". In: *Phys. Rev. Lett.* 61.7 (1988), pp. 834–837. DOI: 10.1103/PhysRevLett.61.834. URL: https://link.aps.org/doi/10.1103/PhysRevLett.61.834 (cit. on pp. 17, 93, 122).

[41] B. Judkewitz, R. Horstmeyer, I. M. Vellekoop, I. N. Papadopoulos, and C. Yang. "Translation correlations in anisotropically scattering media". In: *Nature Physics* 11.8 (2015), pp. 684–689. DOI: 10.1038/nphys3373. URL: https://doi.org/10.1038/nphys3373 (cit. on pp. 17, 93, 98, 122).

[42] F. van Beijnum, E. G. van Putten, A. Lagendijk, and A. P. Mosk. "Frequency bandwidth of light focused through turbid media". In: *Opt. Lett.* 36.3 (2011), pp. 373–375. DOI: 10.1364/OL.36.000373. URL: https://opg.optica.org/ol/abstract.cfm?URI=ol-36-3-373 (cit. on pp. 17, 93, 122).

[43] I. M. Vellekoop and A. P. Mosk. "Focusing coherent light through opaque strongly scattering media". In: *Opt. Lett.* 32.16 (2007), pp. 2309–2311. DOI: 10.1364/OL.32.002309. URL: http://ol.osa.org/abstract.cfm?URI=ol-32-16-2309 (cit. on pp. 17, 18, 21, 48, 62, 79, 82, 87, 93, 95, 104).

[44] I. M. Vellekoop and A. P. Mosk. “Universal Optimal Transmission of Light Through Disordered Materials”. In: *Phys. Rev. Lett.* 101.12 (2008), p. 120601. DOI: 10.1103/PhysRevLett.101.120601. URL: https://link.aps.org/doi/10.1103/PhysRevLett.101.120601 (cit. on pp. 17, 48, 62, 79, 95, 104).

[45] W. Choi, A. P. Mosk, Q.-H. Park, and W. Choi. “Transmission eigenchannels in a disordered medium”. In: *Phys. Rev. B* 83 (13 2011), p. 134207. DOI: 10.1103/PhysRevB.83.134207. URL: https://link.aps.org/doi/10.1103/PhysRevB.83.134207 (cit. on p. 18).

[46] J. Aulbach, B. Gjonaj, P. Johnson, and A. Lagendijk. “Spatiotemporal focusing in opaque scattering media by wave front shaping with nonlinear feedback”. In: *Opt. Express* 20.28 (2012), pp. 29237–29251. DOI: 10.1364/OE.20.029237. URL: https://opg.optica.org/oe/abstract.cfm?URI=oe-20-28-29237 (cit. on pp. 18, 96).

[47] D. B. Conkey, A. N. Brown, A. M. Caravaca-Aguirre, and R. Piestun. “Genetic algorithm optimization for focusing through turbid media in noisy environments”. In: *Opt. Express* 20.5 (2012), pp. 4840–4849. DOI: 10.1364/OE.20.004840. URL: http://www.opticsexpress.org/abstract.cfm?URI=oe-20-5-4840 (cit. on p. 19).

[48] X. Zhang and P. Kner. “Binary wavefront optimization using a genetic algorithm”. In: *Journal of Optics* 16.12 (2014), p. 125704. DOI: 10.1088/2040-8978/16/12/125704. URL: https://doi.org/10.1088/2040-8978/16/12/125704 (cit. on p. 19).

[49] K. Johnstonbaugh, S. Agrawal, D. A. Durairaj, C. Fadden, A. Dangi, S. P. K. Karri, and S. Kothapalli. “A Deep Learning approach to Photoacoustic Wavefront Localization in Deep-Tissue Medium”. In: *IEEE Transactions on Ultrasonics, Ferroelectrics, and Frequency Control* (2020), pp. 1–1. DOI: 10.1109/TUFFC.2020.2964698 (cit. on p. 19).

[50] Y. Luo, S. Yan, H. Li, P. Lai, and Y. Zheng. “Focusing light through scattering media by reinforced hybrid algorithms”. In: *APL Photonics* 5.1 (2020), p. 016109. DOI: 10.1063/1.5131181. URL: https://doi.org/10.1063/1.5131181 (cit. on p. 19).

[51] J. Jannson, T. Jannson, and E. Wolf. “Spatial coherence discrimination in scattering”. In: *Opt. Lett.* 13 (1988), pp. 1060–1062. DOI: 10.1364/OL.13.001060. URL: https://opg.optica.org/ol/abstract.cfm?URI=ol-13-12-1060 (cit. on p. 19).

[52] Z. Tong and O. Korotkova. “Theory of weak scattering of stochastic electromagnetic fields from deterministic and random media”. In: *Phys. Rev. A* 82 (2010), p. 033836. DOI: 10.1103/PhysRevA.82.033836. URL: https://link.aps.org/doi/10.1103/PhysRevA.82.033836 (cit. on p. 19).

[53] A. Ishimaru. *Wave propagation and scattering in random media*. English. NewYork, NY: Academic Press, 1978 (cit. on pp. 19, 48, 49, 62, 104).

[54] J. D. Jackson. *Classical electrodynamics*. English. New York: Wiley, 1998 (cit. on pp. 20, 49, 62, 121).

[55] J. Chaves. *Introduction to Nonimaging Optics*. English. Boca Raton, USA: CRC Press, 2008. ISBN: 978-1-4200-5429-3. DOI: https://doi.org/10.1201/9781420054323 (cit. on p. 20).

[56] Free-form scattering optics consortium. *Free-form scattering optics*. https://www.freeformscatteringoptics.com/about-us/. (Visited on 07/17/2023) (cit. on p. 20).

[57] S. Ping. *Introduction to Wave Scattering, Localization and Mesoscopic Phenomena*. English. Springer-Verlag Berlin Heidelberg: Academic Press, 2006. ISBN: 978-3-540-29155-8. DOI: https://doi.org/10.1007/3-540-29156-3 (cit. on p. 20).

[58] R. Berkovits and S. Feng. "Correlations in coherent multiple scattering". In: *Physics Reports* 238 (1994), pp. 135–172. DOI: https://doi.org/10.1016/0370-1573(94)90079-5. URL: https://www.sciencedirect.com/science/article/pii/0370157394900795 (cit. on p. 20).

[59] S. E. Skipetrov and R. Maynard. "Nonuniversal correlations in multiple scattering". In: *Phys. Rev. B* 62 (2000), pp. 886–891. DOI: 10.1103/PhysRevB.62.886. URL: https://link.aps.org/doi/10.1103/PhysRevB.62.886 (cit. on p. 20).

[60] J. W. Goodman. "Statistical Properties of Laser Speckle Patterns". In: *Laser Speckle and Related Phenomena*. Ed. by J. C. Dainty. Berlin, Heidelberg: Springer, 1975, pp. 9–75. ISBN: 978-3-662-43205-1. DOI: 10.1007/978-3-662-43205-1_2. URL: https://doi.org/10.1007/978-3-662-43205-1_2 (cit. on p. 20).

[61] S. Gigan, O. Katz, H. B. de Aguiar, E. R. Andresen, A. Aubry, J. Bertolotti, E. Bossy, D. Bouchet, J. Brake, S. Brasselet, Y. Bromberg, H. Cao, T. Chaigne, Z. Cheng, W. Choi, T. Čižmár, M. Cui, V. R. Curtis, H. Defienne, M. Hofer, R. Horisaki, R. Horstmeyer, N. Ji, A. K. LaViolette, J. Mertz, C. Moser, A. P. Mosk, N. C. Pégard, R. Piestun, S. Popoff, D. B. Phillips, D. Psaltis, B. Rahmani, H. Rigneault, S. Rotter, L. Tian, I. M. Vellekoop, L. Waller, L. Wang, T. Weber, S. Xiao, C. Xu, A. Yamilov, C. Yang, and H. Yılmaz. "Roadmap on wavefront shaping and deep imaging in complex media". In: *Journal of Physics: Photonics* 4.4 (2022), p. 042501. DOI: 10.1088/2515-7647/ac76f9. URL: https://dx.doi.org/10.1088/2515-7647/ac76f9 (cit. on pp. 21, 93).

[62] H. Cao, A. P. Mosk, and S. Rotter. "Shaping the propagation of light in complex media". In: *Nature Physics* 18.9 (2022), pp. 994–1007. DOI: 10.1038/s41567-022-01677-x. URL: https://doi.org/10.1038/s41567-022-01677-x (cit. on p. 21).

[63] A. P. Mosk, A. Lagendijk, G. Lerosey, and M. Fink. "Controlling waves in space and time for imaging and focusing in complex media". In: *Nat. Photonics* 6.5 (2012), pp. 283–292. DOI: 10.1038/nphoton.2012.88. URL: https://doi.org/10.1038/nphoton.2012.88 (cit. on pp. 21, 48, 62, 82, 87, 93).

[64] J. Kubby, S. Gigan, and M. Cui. *Wavefront shaping for biomedical imaging*. English. Cambridge, UK: Cambridge University Press, 2019 (cit. on pp. 21, 48).

[65] A. Badon, V. Barolle, K. Irsch, C. A. Boccara, M. Fink, and A. Aubry. "Distortion matrix concept for deep optical imaging in scattering media". In: *Science Advances* 6.30 (2020), eaay7170. DOI: 10.1126/sciadv.aay7170. URL: https://www.science.org/doi/abs/10.1126/sciadv.aay7170 (cit. on pp. 21, 117).

[66] S. Popoff, G. Lerosey, M. Fink, A. C. Boccara, and S. Gigan. "Image transmission through an opaque material". In: *Nature Communications* 1.1 (2010), p. 81. DOI: 10.1038/ncomms1078. URL: https://doi.org/10.1038/ncomms1078 (cit. on pp. 21, 104).

[67] S. M. Popoff, G. Lerosey, R. Carminati, M. Fink, A. C. Boccara, and S. Gigan. "Measuring the Transmission Matrix in Optics: An Approach to the Study and Control of Light Propagation in Disordered Media". In: *Phys. Rev. Lett.* 104.10 (2010), p. 100601. DOI: 10.1103/PhysRevLett.104.100601. URL: https://link.aps.org/doi/10.1103/PhysRevLett.104.100601 (cit. on pp. 21, 45, 48, 62, 104).

[68] I. Freund. "Looking through walls and around corners". In: *Physica A* 168 (1990), pp. 49–65. URL: https://doi.org/10.1016/0378-4371(90)90357-X (cit. on pp. 21, 96, 98).

[69] A. Lagendijk, A. P. Mosk, and W. L. Vos. "Mutual extinction and transparency of multiple incident light waves". In: *EPL* 130.3 (2020), p. 34002. DOI: 10.1209/0295-5075/130/34002. URL: https://doi.org/10.1209/0295-5075/130/34002 (cit. on pp. 21, 48, 53, 54, 57, 58, 62, 82, 104).

[70] A. Rates, A. Lagendijk, O. Akdemir, A. P. Mosk, and W. L. Vos. "Observation of mutual extinction and transparency in light scattering". In: *Phys. Rev. A* 104.4 (2021), p. 043515. DOI: 10.1103/PhysRevA.104.043515. URL: https://link.aps.org/doi/10.1103/PhysRevA.104.043515 (cit. on pp. 21, 47, 62, 63, 64, 75, 82, 104).

[71] M. D. Truong, A. Lagendijk, and W. L. Vos. "Sensing the position of a single scatterer in an opaque medium by mutual scattering". In: *Opt. Express* 31.9 (2023), pp. 15058–15074. DOI: 10.1364/OE.482472. URL: https://opg.optica.org/oe/abstract.cfm?URI=oe-31-9-15058 (cit. on pp. 22, 57, 71, 82, 122).

[72] S. Rotter and S. Gigan. "Light fields in complex media: Mesoscopic scattering meets wave control". In: *Rev. Mod. Phys.* 89.1 (2017), p. 015005. DOI: 10.1103/RevModPhys.89.015005. URL: https://link.aps.org/doi/10.1103/RevModPhys.89.015005 (cit. on pp. 22, 48, 62, 82, 87, 93).

[73] R. Carminati and J. C. Schotland. *Principles of Scattering and Transport of Light*. Cambridge University Press, 2021. DOI: 10.1017/9781316544693 (cit. on pp. 22, 62, 63, 104).

[74] A. de Mots. "High precision phase measurement setup for mutual extinction". PhD thesis. Netherlands: University of Twente, 2021 (cit. on p. 30).

[75] Z. Zhang, Z. You, and D. Chu. "Fundamentals of phase-only liquid crystal on silicon (LCOS) devices". In: *Light: Science & Applications* 3.10 (2014), e213–e213. DOI: 10.1038/lsa.2014.94. URL: https://doi.org/10.1038/lsa.2014.94 (cit. on p. 32).

[76] N. Collings, T. Davey, J. Christmas, D. Chu, and B. Crossland. "The Applications and Technology of Phase-Only Liquid Crystal on Silicon Devices". In: *Journal of Display Technology* 7.3 (2011), pp. 112–119. DOI: 10.1109/JDT.2010.2049337 (cit. on p. 32).

[77] A. B. Ayoub and D. Psaltis. "High speed, complex wavefront shaping using the digital micro-mirror device". In: *Scientific Reports* 11.1 (2021), p. 18837. DOI: 10.1038/s41598-021-98430-w. URL: https://doi.org/10.1038/s41598-021-98430-w (cit. on p. 32).

[78] M.-C. Park, B.-R. Lee, J.-Y. Son, and O. Chernyshov. "Properties of DMDs for holographic displays". In: *Journal of Modern Optics* 62.19 (2015), pp. 1600–1607. DOI: 10.1080/09500340.2015.1054445. URL: https://doi.org/10.1080/09500340.2015.1054445 (cit. on p. 32).

[79] W.-H. Lee. “III Computer-Generated Holograms: Techniques and Applications”. In: *Progress in Optics*. Ed. by E. Wolf. Vol. 16. Elsevier, 1978, pp. 119–232. DOI: https://doi.org/10.1016/S0079-6638(08)70072-6. URL: https://www.sciencedirect.com/science/article/pii/S0079663808700726 (cit. on pp. 33, 64, 82, 93, 107).

[80] D. B. Conkey, A. M. Caravaca-Aguirre, and R. Piestun. “High-speed scattering medium characterization with application to focusing light through turbid media”. In: *Opt. Express* 20.2 (2012), pp. 1733–1740. DOI: 10.1364/OE.20.001733. URL: http://www.opticsexpress.org/abstract.cfm?URI=oe-20-2-1733 (cit. on pp. 33, 64, 82, 93, 107).

[81] S. A. Goorden, J. Bertolotti, and A. P. Mosk. “Superpixel-based spatial amplitude and phase modulation using a digital micromirror device”. In: *Opt. Express* 22.15 (2014), pp. 17999–18009. DOI: 10.1364/OE.22.017999. URL: https://opg.optica.org/oe/abstract.cfm?URI=oe-22-15-17999 (cit. on p. 33).

[82] W. H. Lee. “Sampled Fourier Transform Hologram Generated by Computer”. In: *Appl. Opt.* 9.3 (1970), pp. 639–643. DOI: 10.1364/AO.9.000639. URL: https://opg.optica.org/ao/abstract.cfm?URI=ao-9-3-639 (cit. on p. 33).

[83] K. Campbell, G. W. Wecksung, and C. R. Mansfield. “Spatial Filtering By Digital Holography”. In: *Optical Engineering* 13.3 (1974), p. 133175. DOI: 10.1117/12.7971694. URL: https://doi.org/10.1117/12.7971694 (cit. on p. 33).

[84] S. M. Popoff. *Setting up a DMD/SLM: Aberration effects*. https://www.wavefrontshaping.net/post/id/23. Accessed: 2023-04-18. 2019 (cit. on pp. 34, 35, 66).

[85] M. Born and E. Wolf. *Principles of optics*. English. Oxford, New York: Pergamon Press, 1970 (cit. on pp. 35, 57, 66, 121).

[86] P. A. Khorin and S. A. Degtyarev. *Wavefront aberration analysis with a multi-order diffractive optical element*. 2017. DOI: 10.18287/1613-0073-2017-1900-28-33. URL: http://dx.doi.org/10.18287/1613-0073-2017-1900-28-33 (cit. on p. 35).

[87] V. Lakshminarayanan and A. Fleck. “Zernike polynomials: a guide”. In: *Journal of Modern Optics* 58.7 (2011), pp. 545–561. DOI: 10.1080/09500340.2011.554896. URL: https://doi.org/10.1080/09500340.2011.554896 (cit. on p. 35).

[88] F. Zernike. “Beugungstheorie des schneidenver-fahrens und seiner verbesserten form, der phasenkontrastmethode”. In: *Physica* 1.7 (1934), pp. 689–704. DOI: https://doi.org/10.1016/S0031-8914(34)80259-5. URL: https://www.sciencedirect.com/science/article/pii/S0031891434802595 (cit. on p. 35).

[89] Y. Xu. *Orthogonal polynomials of several variables*. 2021. eprint: 1701.02709 (math.CA) (cit. on p. 35).

[90] J. Lodewyck. *GaussianBeam: Simulate Gaussian optics*. Sourceforge C++ software. 2013. URL: https://gaussianbeam.sourceforge.net/ (cit. on p. 42).

[91] Z. Wang and A. C. Bovik. “Mean squared error: Love it or leave it? A new look at Signal Fidelity Measures”. In: *IEEE Signal Processing Magazine* 26.1 (2009), pp. 98–117. DOI: 10.1109/MSP.2008.930649 (cit. on p. 43).

[92] Z. Wang, A. Bovik, H. Sheikh, and E. Simoncelli. "Image quality assessment: from error visibility to structural similarity". In: *IEEE Transactions on Image Processing* 13.4 (2004), pp. 600–612. DOI: 10.1109/TIP.2003.819861 (cit. on p. 43).

[93] M. Mounaix, H. Defienne, and S. Gigan. "Deterministic light focusing in space and time through multiple scattering media with a time-resolved transmission matrix approach". In: *Phys. Rev. A* 94.4 (2016), 041802(R). DOI: 10.1103/PhysRevA.94.041802. URL: https://link.aps.org/doi/10.1103/PhysRevA.94.041802 (cit. on pp. 45, 48).

[94] D. Akbulut, T. Strudley, J. Bertolotti, E. P. A. M. Bakkers, A. Lagendijk, O. L. Muskens, W. L. Vos, and A. P. Mosk. "Optical transmission matrix as a probe of the photonic strength". In: *Phys. Rev. A* 94.4 (2016), p. 043817. DOI: 10.1103/PhysRevA.94.043817. URL: https://link.aps.org/doi/10.1103/PhysRevA.94.043817 (cit. on pp. 45, 62, 104).

[95] E. F. Schubert. *Light-emitting diodes*. English. Cambridge: Cambridge University Press, 2006 (cit. on pp. 48, 92).

[96] M. L. Meretska, G. Vissenberg, A. Lagendijk, W. L. IJzerman, and W. L. Vos. "Systematic Design of the Color Point of a White LED". In: *ACS Photonics* 6.12 (2019), pp. 3070–3075. DOI: 10.1021/acsphotonics.9b00173. URL: https://doi.org/10.1021/acsphotonics.9b00173 (cit. on p. 48).

[97] J. W. Goodman. *Introduction to Fourier optics*. English. New York: McGraw-Hill, 1968 (cit. on pp. 48, 62, 121).

[98] J. Aulbach, B. Gjonaj, P. M. Johnson, A. P. Mosk, and A. Lagendijk. "Control of Light Transmission through Opaque Scattering Media in Space and Time". In: *Phys. Rev. Lett.* 106.10 (2011), p. 103901. DOI: 10.1103/PhysRevLett.106.103901. URL: https://link.aps.org/doi/10.1103/PhysRevLett.106.103901 (cit. on p. 48).

[99] H. Yılmaz, C. W. Hsu, A. Goetschy, S. Bittner, S. Rotter, A. Yamilov, and H. Cao. "Angular Memory Effect of Transmission Eigenchannels". In: *Phys. Rev. Lett.* 123.20 (2019), p. 203901. DOI: 10.1103/PhysRevLett.123.203901. URL: https://link.aps.org/doi/10.1103/PhysRevLett.123.203901 (cit. on p. 48).

[100] D. Li, S. Sun, and Y. Yao. "Excess-noise suppression for a squeezed state propagating through random amplifying media via wave-front shaping". In: *Phys. Rev. A* 103.2 (2021), p. 023712. DOI: 10.1103/PhysRevA.103.023712. URL: https://link.aps.org/doi/10.1103/PhysRevA.103.023712 (cit. on p. 48).

[101] O. Katz, E. Small, Y. Bromberg, and Y. Silberberg. "Focusing and compression of ultrashort pulses through scattering media". In: *Nat. Photonics* 5.6 (2011), pp. 372–377. DOI: 10.1038/nphoton.2011.72. URL: https://doi.org/10.1038/nphoton.2011.72 (cit. on p. 48).

[102] D. J. McCabe, A. Tajalli, D. R. Austin, P. Bondareff, I. A. Walmsley, S. Gigan, and B. Chatel. "Spatio-temporal focusing of an ultrafast pulse through a multiply scattering medium". In: *Nat. Commun.* 2.1 (2011), p. 447. DOI: 10.1038/ncomms1434. URL: https://doi.org/10.1038/ncomms1434 (cit. on p. 48).

[103] I. M. Vellekoop. "Feedback-based wavefront shaping". In: *Opt. Express* 23.9 (2015), pp. 12189–12206. DOI: 10.1364/OE.23.012189. URL: http://www.opticsexpress.org/abstract.cfm?URI=oe-23-9-12189 (cit. on pp. 48, 82, 87, 93).

[104] R. Horstmeyer, H. Ruan, and C. Yang. "Guidestar-assisted wavefront-shaping methods for focusing light into biological tnumber". In: *Nat. Photonics* 9.9 (2015), pp. 563–571. DOI: 10.1038/nphoton.2015.140. URL: https://doi.org/10.1038/nphoton.2015.140 (cit. on pp. 48, 93).

[105] W. Wan, Y. Chong, L. Ge, H. Noh, A. D. Stone, and H. Cao. "Time-Reversed Lasing and Interferometric Control of Absorption". In: *Science* 331.6019 (2011), pp. 889–892. DOI: 10.1126/science.1200735. URL: https://science.sciencemag.org/content/331/6019/889 (cit. on p. 48).

[106] R. Sarma, A. G. Yamilov, S. Petrenko, Y. Bromberg, and H. Cao. "Control of Energy Density inside a Disordered Medium by Coupling to Open or Closed Channels". In: *Phys. Rev. Lett.* 117.8 (2016), p. 086803. DOI: 10.1103/PhysRevLett.117.086803. URL: https://link.aps.org/doi/10.1103/PhysRevLett.117.086803 (cit. on pp. 48, 57).

[107] O. S. Ojambati, J. T. Hosmer-Quint, K.-J. Gorter, A. P. Mosk, and W. L. Vos. "Controlling the intensity of light in large areas at the interfaces of a scattering medium". In: *Phys. Rev. A* 94.4 (2016), p. 043834. DOI: 10.1103/PhysRevA.94.043834. URL: https://link.aps.org/doi/10.1103/PhysRevA.94.043834 (cit. on pp. 48, 100).

[108] Z. Yaqoob, D. Psaltis, M. S. Feld, and C. Yang. "Optical phase conjugation for turbidity suppression in biological samples". In: *Nat. Photonics* 2.2 (2008), pp. 110–115. DOI: 10.1038/nphoton.2007.297. URL: https://doi.org/10.1038/nphoton.2007.297 (cit. on p. 48).

[109] Y. Sung, W. Choi, C. Fang-Yen, K. Badizadegan, R. R. Dasari, and M. S. Feld. "Optical diffraction tomography for high resolution live cell imaging". In: *Opt. Express* 17.1 (2009), pp. 266–277. DOI: 10.1364/OE.17.000266. URL: http://www.opticsexpress.org/abstract.cfm?URI=oe-17-1-266 (cit. on p. 48).

[110] H. Yılmaz, E. G. van Putten, J. Bertolotti, A. Lagendijk, W. L. Vos, and A. P. Mosk. "Speckle correlation resolution enhancement of wide-field fluorescence imaging". In: *Optica* 2.5 (2015), pp. 424–429. DOI: 10.1364/OPTICA.2.000424. URL: http://www.osapublishing.org/optica/abstract.cfm?URI=optica-2-5-424 (cit. on pp. 48, 104).

[111] R. G. Newton. "Optical theorem and beyond". In: *Am. J. Phys.* 44.7 (1976), pp. 639–642. DOI: 10.1119/1.10324. URL: https://doi.org/10.1119/1.10324 (cit. on p. 48).

[112] R. G. Newton. *Scattering theory of waves and particles*. 2nd. Berlin, Heidelberg: Springer-Verlag, 1982 (cit. on pp. 48, 62, 63).

[113] A. A. Kharin, B. Varghese, R. Verhagen, and N. Uzunbajakava. "Optical properties of the medulla and the cortex of human scalp hair". In: *Journal of Biomedical Optics* 14.2 (2009), pp. 1–7. DOI: 10.1117/1.3116712. URL: https://doi.org/10.1117/1.3116712 (cit. on pp. 48, 76).

[114] M. D. Prasad, M. G. Krishna, and S. K. Batabyal. "Facet-Engineered Surfaces of Two-Dimensional Layered BiOI and Au–BiOI Substrates for Tuning the Surface-Enhanced Raman Scattering and Visible Light Photodetector Response". In: *ACS Appl. Nano Mater.* 2.6 (2019), pp. 3906–3915. DOI: 10.1021/acsanm.9b00771. URL: https://doi.org/10.1021/acsanm.9b00771 (cit. on p. 48).

[115] D. A. Grishina, C. A. M. Harteveld, A. Pacureanu, D. Devashish, A. Lagendijk, P. Cloetens, and W. L. Vos. "X-ray Imaging of Functional Three-Dimensional Nanostructures on Massive Substrates". In: *ACS Nano* 13.12 (2019), pp. 13932–13939. DOI: 10.1021/acsnano.9b05519. URL: https://doi.org/10.1021/acsnano.9b05519 (cit. on p. 48).

[116] S. R. Marschner, H. W. Jensen, M. Cammarano, S. Worley, and P. Hanrahan. "Light Scattering from Human Hair Fibers". In: *ACM Trans. Graph.* 22.3 (2003), pp. 780–791. DOI: 10.1145/882262.882345. URL: https://doi-org.ezproxy2.utwente.nl/10.1145/882262.882345 (cit. on pp. 53, 75, 76).

[117] R. Messer. "Single slit interference made easy with a strand of hair and a laser". In: *Phys. Teach.* 56.1 (2018), pp. 58–59. DOI: 10.1119/1.5018699. URL: https://doi.org/10.1119/1.5018699 (cit. on p. 53).

[118] T. Čižmár and K. Dholakia. "Tunable Bessel light modes: engineering the axial propagation". In: *Opt. Express* 17.18 (2009), pp. 15558–15570. DOI: 10.1364/OE.17.015558. URL: http://www.opticsexpress.org/abstract.cfm?URI=oe-17-18-15558 (cit. on p. 57).

[119] L. Gong, Y.-X. Ren, G.-S. Xue, Q.-C. Wang, J.-H. Zhou, M.-C. Zhong, Z.-Q. Wang, and Y.-M. Li. "Generation of nondiffracting Bessel beam using digital micromirror device". In: *Appl. Opt.* 52.19 (2013), pp. 4566–4575. DOI: 10.1364/AO.52.004566. URL: http://ao.osa.org/abstract.cfm?URI=ao-52-19-4566 (cit. on p. 57).

[120] N. Raptis, E. Pikasis, and D. Syvridis. "Performance evaluation of modulation and multiple access schemes in ultraviolet optical wireless connections for two atmosphere thickness cases". In: *J. Opt. Soc. Am. A* 33.8 (2016), pp. 1628–1640. DOI: 10.1364/JOSAA.33.001628. URL: http://josaa.osa.org/abstract.cfm?URI=josaa-33-8-1628 (cit. on p. 57).

[121] J. Haberko, N. Muller, and F. Scheffold. "Direct laser writing of three-dimensional network structures as templates for disordered photonic materials". In: *Phys. Rev. A* 88.4 (2013), p. 043822. DOI: 10.1103/PhysRevA.88.043822. URL: https://link.aps.org/doi/10.1103/PhysRevA.88.043822 (cit. on p. 57).

[122] G. Maret and P. E. Wolf. "Multiple light scattering from disordered media. The effect of brownian motion of scatterers". In: *Z. Phys. B* 65.4 (1987), pp. 409–413. DOI: 10.1007/BF01303762. URL: https://doi.org/10.1007/BF01303762 (cit. on p. 57).

[123] D. J. Pine, D. A. Weitz, P. M. Chaikin, and E. Herbolzheimer. "Diffusing wave spectroscopy". In: *Phys. Rev. Lett.* 60.12 (1988), pp. 1134–1137. DOI: 10.1103/PhysRevLett.60.1134. URL: https://link.aps.org/doi/10.1103/PhysRevLett.60.1134 (cit. on p. 57).

[124] J. Stetefeld, S. A. McKenna, and T. R. Patel. "Dynamic light scattering: a practical guide and applications in biomedical sciences". In: *Biophys. Rev.* 8.4 (2016), pp. 409–427. DOI: 10.1007/s12551-016-0218-6. URL: https://doi.org/10.1007/s12551-016-0218-6 (cit. on pp. 57, 62).

[125] B. J. Berne and R. Pecora. *Dynamic Light Scattering : With Applications to Chemistry, Biology, and Physics.* English. Mineola, NY: Dover, 2013 (cit. on p. 57).

[126] A. Rates. *Observation of mutual extinction and transparency in light scattering*. 2021. DOI: 10.5281/zenodo.5221092. URL: https://doi.org/10.5281/zenodo.5221092 (cit. on p. 58).

[127] T. A. Nieminen, A. B. Stilgoe, N. R. Heckenberg, and H. Rubinsztein-Dunlop. "Angular momentum of a strongly focused Gaussian beam". In: *J. Opt. A: Pure Appl. Opt.* 10.11 (2008), p. 115005. DOI: 10.1088/1464-4258/10/11/115005. URL: https://doi.org/10.1088/1464-4258/10/11/115005 (cit. on p. 59).

[128] E. Akkermans and G. Montambaux. *Mesoscopic Physics of Electrons and Photons*. Cambridge University Press, 2007. DOI: 10.1017/CBO9780511618833 (cit. on pp. 62, 104, 125).

[129] R. Pecora, ed. *Dynamic light scattering*. English. 1985th ed. New York, NY: Springer, 1985 (cit. on p. 62).

[130] D. Huang, E. A. Swanson, C. P. Lin, J. S. Schuman, W. G. Stinson, W. Chang, M. R. Hee, T. Flotte, K. Gregory, C. A. Puliafito, and J. G. Fujimoto. "Optical Coherence Tomography". In: *Science* 254.5035 (1991), pp. 1178–1181. DOI: 10.1126/science.1957169. URL: https://www.science.org/doi/abs/10.1126/science.1957169 (cit. on p. 62).

[131] A. G. Podoleanu. "Optical coherence tomography". In: *Journal of Microscopy* 247.3 (2012), pp. 209–219. DOI: https://doi.org/10.1111/j.1365-2818.2012.03619.x. URL: https://onlinelibrary.wiley.com/doi/abs/10.1111/j.1365-2818.2012.03619.x (cit. on p. 62).

[132] W. Drexler and J. G. Fujimoto. *Optical Coherence Tomography*. English. Switzerland: Springer Cham, 2015. DOI: 10.1007/978-3-319-06419-2 (cit. on p. 62).

[133] A. Yodh and B. Chance. "Spectroscopy and Imaging with Diffusing Light". In: *Physics Today* 48.3 (1995), pp. 34–40. DOI: 10.1063/1.881445. URL: https://doi.org/10.1063/1.881445 (cit. on p. 62).

[134] A. Messiah. *Quantum Mechanics, Volume 1*. Amsterdam: North Holland, 1967 (cit. on pp. 63, 121).

[135] *Datasheet for ICX445ALA CCD sensor*. ICX445ALA. Sony Corporation. 2009. URL: https://www.digchip.com/datasheets/parts/datasheet/142/ICX445ALA-pdf.php (cit. on p. 70).

[136] M. Megens, C. M. van Kats, P. Bösecke, and W. L. Vos. "In Situ Characterization of Colloidal Spheres by Synchrotron Small-Angle X-ray Scattering". In: *Langmuir* 13.23 (1997), pp. 6120–6129. DOI: 10.1021/la970422v. URL: https://doi.org/10.1021/la970422v (cit. on p. 75).

[137] G. E. Rogers. "Known and Unknown Features of Hair Cuticle Structure: A Brief Review". In: *Cosmetics* 6.2 (2019), p. 32. ISSN: 2079-9284. DOI: 10.3390/cosmetics6020032. URL: https://www.mdpi.com/2079-9284/6/2/32 (cit. on p. 76).

[138] F.-C. Yang, Y. Zhang, and M. C. Rheinstädter. "The structure of people's hair". In: *PeerJ* 2 (2014), e619. DOI: 10.7717/peerj.619. URL: https://peerj.com/articles/619/ (cit. on p. 76).

[139] S. M. Popoff, A. Goetschy, S. F. Liew, A. D. Stone, and H. Cao. “Coherent Control of Total Transmission of Light through Disordered Media”. In: *Phys. Rev. Lett.* 112.13 (2014), p. 133903. DOI: 10.1103/PhysRevLett.112.133903. URL: https://link.aps.org/doi/10.1103/PhysRevLett.112.133903 (cit. on pp. 82, 87, 93).

[140] S. Nakamura. “Background story of the invention of efficient blue InGaN light emitting diodes (Nobel Lecture)”. In: *Annalen der Physik* 527.5-6 (2015), pp. 335–349. DOI: https://doi.org/10.1002/andp.201500801. URL: https://onlinelibrary.wiley.com/doi/abs/10.1002/andp.201500801 (cit. on p. 92).

[141] M. R. Krames, O. B. Shchekin, R. Mueller-Mach, G. O. Mueller, L. Zhou, G. Harbers, and M. G. Craford. “Status and Future of High-Power Light-Emitting Diodes for Solid-State Lighting”. In: *Journal of Display Technology* 3.2 (2007), pp. 160–175. DOI: 10.1109/JDT.2007.895339 (cit. on p. 92).

[142] M. Nixon, O. Katz, E. Small, Y. Bromberg, A. A. Friesem, Y. Silberberg, and N. Davidson. “Real-time wavefront shaping through scattering media by all-optical feedback”. In: *Nature Photonics* 7.11 (2013), pp. 919–924. DOI: 10.1038/nphoton.2013.248. URL: https://doi.org/10.1038/nphoton.2013.248 (cit. on p. 93).

[143] R. Sarma, A. Yamilov, and H. Cao. “Enhancing light transmission through a disordered waveguide with inhomogeneous scattering and loss”. In: *Applied Physics Letters* 110.2 (2017), p. 021103. DOI: 10.1063/1.4973459. URL: https://doi.org/10.1063/1.4973459 (cit. on p. 93).

[144] R. Uppu, M. Adhikary, C. A. M. Harteveld, and W. L. Vos. “Spatially Shaping Waves to Penetrate Deep inside a Forbidden Gap”. In: *Phys. Rev. Lett.* 126.17 (2021), p. 177402. DOI: 10.1103/PhysRevLett.126.177402. URL: https://link.aps.org/doi/10.1103/PhysRevLett.126.177402 (cit. on p. 93).

[145] F. Pedregosa, G. Varoquaux, A. Gramfort, V. Michel, B. Thirion, O. Grisel, M. Blondel, P. Prettenhofer, R. Weiss, V. Dubourg, J. Vanderplas, A. Passos, D. Cournapeau, M. Brucher, M. Perrot, and E. Duchesnay. “Scikit-learn: Machine Learning in Python”. In: *Journal of Machine Learning Research* 12 (2011), pp. 2825–2830 (cit. on pp. 96, 109).

[146] E. Fujiwara, J. A. Fracarolli, and C. M. B. Cordeiro. “Didactic laser speckle experiments with a lensless camera”. In: *European Journal of Physics* 42.6 (2021), p. 065303. DOI: 10.1088/1361-6404/ac2b04. URL: https://dx.doi.org/10.1088/1361-6404/ac2b04 (cit. on p. 99).

[147] A. Rates, J. Vrehen, B. Mulder, W. L. Ijzerman, and W. L. Vos. “Enhanced secrecy in optical communication using speckle from multiple scattering layers”. In: *Opt. Express* 31 (2023), pp. 23897–23909. DOI: 10.1364/OE.493479. URL: https://opg.optica.org/oe/abstract.cfm?URI=oe-31-15-23897 (cit. on p. 103).

[148] J. W. Goodman. *Speckle phenomena in optics : theory and applications*. English. Englewood CO: Roberts & Co., 2007. ISBN: 9781510631489. URL: https://spie.org/Publications/Book/2548482?SSO=1 (cit. on p. 104).

[149] R. Pappu, B. Recht, J. Taylor, and N. Gershenfeld. "Physical One-Way Functions". In: *Science* 297.5589 (2002), pp. 2026–2030. DOI: 10.1126/science.1074376. URL: https://www.science.org/doi/abs/10.1126/science.1074376 (cit. on pp. 104, 115).

[150] U. Rührmair, H. Busch, and S. Katzenbeisser. "Strong PUFs: Models, Constructions, and Security Proofs". In: *Towards Hardware-Intrinsic Security: Foundations and Practice*. Berlin, Heidelberg: Springer Berlin Heidelberg, 2010, pp. 79–96. ISBN: 978-3-642-14452-3. DOI: 10.1007/978-3-642-14452-3_4. URL: https://doi.org/10.1007/978-3-642-14452-3_4 (cit. on p. 104).

[151] S. A. Goorden, M. Horstmann, A. P. Mosk, B. Škorić, and P. W. H. Pinkse. "Quantum-secure authentication of a physical unclonable key". In: *Optica* 1.6 (2014), pp. 421–424. DOI: 10.1364/OPTICA.1.000421. URL: http://www.osapublishing.org/optica/abstract.cfm?URI=optica-1-6-421 (cit. on p. 104).

[152] S. Dolev, Ł. Krzywiecki, N. Panwar, and M. Segal. "Optical PUF for Non-Forwardable Vehicle Authentication". In: *Computer Communications* 93 (2016), pp. 52–67. ISSN: 0140-3664. DOI: https://doi.org/10.1016/j.comcom.2016.05.016. URL: https://www.sciencedirect.com/science/article/pii/S014036641630233X (cit. on p. 104).

[153] M. Tehranipoor, N. Pundir, N. Vashistha, and F. Farahmandi. "Optical PUF". In: *Hardware Security Primitives*. Springer International Publishing, 2023, pp. 97–118. ISBN: 978-3-031-19185-5. DOI: 10.1007/978-3-031-19185-5_7. URL: https://doi.org/10.1007/978-3-031-19185-5_7 (cit. on p. 104).

[154] J. Bertolotti, E. G. van Putten, C. Blum, A. Lagendijk, W. L. Vos, and A. P. Mosk. "Non-invasive imaging through opaque scattering layers". In: *Nature* 491.7423 (2012), pp. 232–234. DOI: 10.1038/nature11578. URL: https://doi.org/10.1038/nature11578 (cit. on pp. 104, 107).

[155] Y. Cao, Y. Xiao, Z. Pan, L. Zhou, and W. Chen. "Direct generation of 2D arrays of random numbers for high-fidelity optical ghost diffraction and information transmission through scattering media". In: *Optics and Lasers in Engineering* 158 (2022), p. 107141. DOI: https://doi.org/10.1016/j.optlaseng.2022.107141. URL: https://www.sciencedirect.com/science/article/pii/S0143816622001932 (cit. on p. 104).

[156] D. Akbulut, T. J. Huisman, E. G. van Putten, W. L. Vos, and A. P. Mosk. "Focusing light through random photonic media by binary amplitude modulation". In: *Opt. Express* 19.5 (2011), pp. 4017–4029. DOI: 10.1364/OE.19.004017. URL: http://opg.optica.org/oe/abstract.cfm?URI=oe-19-5-4017 (cit. on p. 107).

[157] E. Edrei and G. Scarcelli. "Memory-effect based deconvolution microscopy for super-resolution imaging through scattering media". In: *Scientific Reports* 6.1 (2016), p. 33558. DOI: 10.1038/srep33558. URL: https://doi.org/10.1038/srep33558 (cit. on p. 107).

[158] *Longitudinal spectrum measurements of various lasers*. URL: http://hololaser.kwaoo.me/laser/spectra.html (cit. on p. 107).

[159] G. K. Kanji. *100 statistical tests*. English. London; Thousand Oaks: SAGE Publications, 2006. ISBN: 9781412923767. URL: https://dx.doi.org/10.4135/9781849208499 (cit. on p. 111).

[160] K. H. Brodersen, C. S. Ong, K. E. Stephan, and J. M. Buhmann. “The Balanced Accuracy and Its Posterior Distribution”. In: *2010 20th International Conference on Pattern Recognition*. 2010, pp. 3121–3124. DOI: 10.1109/ICPR.2010.764 (cit. on p. 114).

[161] P. Flajolet, D. Gardy, and L. Thimonier. “Birthday paradox, coupon collectors, caching algorithms and self-organizing search”. In: *Discrete Applied Mathematics* 39.3 (1992), pp. 207–229. ISSN: 0166-218X. DOI: https://doi.org/10.1016/0166-218X(92)90177-C. URL: https://www.sciencedirect.com/science/article/pii/0166218X9290177C (cit. on p. 115).

[162] U. Rührmair, F. Sehnke, J. Sölter, G. Dror, S. Devadas, and J. Schmidhuber. “Modeling Attacks on Physical Unclonable Functions”. In: *Proceedings of the 17th ACM Conference on Computer and Communications Security*. CCS ’10. New York, NY, USA: Association for Computing Machinery, 2010, pp. 237–249. ISBN: 9781450302456. DOI: 10.1145/1866307.1866335. URL: https://doi.org/10.1145/1866307.1866335 (cit. on p. 115).

[163] Y. Gao, S. F. Al-Sarawi, and D. Abbott. “Physical unclonable functions”. In: *Nature Electronics* 3.2 (2020), pp. 81–91. DOI: 10.1038/s41928-020-0372-5. URL: https://doi.org/10.1038/s41928-020-0372-5 (cit. on p. 115).

[164] Thorlabs inc. *Free-space electro-optic modulators*. https://www.thorlabs.com/newgrouppage9.cfm?objectgroup_id=2729. (Visited on 02/19/2023) (cit. on p. 117).

[165] X. Shao, W. Dai, T. Wu, H. Li, and L. Wang. “Speckle-correlation imaging through highly scattering turbid media with LED illumination”. In: *Smart Biomedical and Physiological Sensor Technology XII*. Ed. by B. M. Cullum and E. S. McLamore. Vol. 9487. SPIE, 2015, p. 948710. DOI: 10.1117/12.2176175. URL: https://doi.org/10.1117/12.2176175 (cit. on p. 117).

[166] A. Zhai, Q. Han, T. Zhang, W. Zhao, and D. Wang. “Optical encryption using structural uncorrelated characteristics of biological scattering media”. In: *Journal of Modern Optics* 0.0 (2023), pp. 1–8. DOI: 10.1080/09500340.2023.2183055. URL: https://doi.org/10.1080/09500340.2023.2183055 (cit. on p. 117).

[167] W. Lambert, L. A. Cobus, M. Couade, M. Fink, and A. Aubry. “Reflection Matrix Approach for Quantitative Imaging of Scattering Media”. In: *Phys. Rev. X* 10 (2 2020), p. 021048. DOI: 10.1103/PhysRevX.10.021048. URL: https://link.aps.org/doi/10.1103/PhysRevX.10.021048 (cit. on p. 117).

[168] W. Lambert, L. A. Cobus, T. Frappart, M. Fink, and A. Aubry. “Distortion matrix approach for ultrasound imaging of random scattering media”. In: *Proceedings of the National Academy of Sciences* 117.26 (2020), pp. 14645–14656. DOI: 10.1073/pnas.1921533117. URL: https://www.pnas.org/doi/abs/10.1073/pnas.1921533117 (cit. on p. 117).

[169] S. Shahjahan, A. Aubry, F. Rupin, B. Chassignole, and A. Derode. “A random matrix approach to detect defects in a strongly scattering polycrystal: How the memory effect can help overcome multiple scattering”. In: *Applied Physics Letters* 104.23 (2014). DOI: 10.1063/1.4882421. URL: https://doi.org/10.1063/1.4882421 (cit. on p. 117).

[170] A. Rates. *From Noise to Signal: Multi-layer Speckle Correlation with Applications in Visible Light Communication*. DOI: 10.5281/zenodo.6397330. URL: https://doi.org/10.5281/zenodo.6397330 (cit. on p. 118).

[171] E. Hecht. *Optics*. London: Pearson Education, 2017. ISBN: 9780133977226 (cit. on p. 121).

[172] C. J. Bouwkamp. "Diffraction Theory". In: *Reports on Progress in Physics* 17.1 (1954), pp. 35–100. DOI: 10.1088/0034-4885/17/1/302. URL: https://doi.org/10.1088/0034-4885/17/1/302 (cit. on p. 121).

[173] E. D. Palik. *Handbook of Optical Constants of Solids*. Boston: Academic Press, 1997. ISBN: 978-0-12-544415-6. URL: https://www.sciencedirect.com/book/9780125444156/handbook-of-optical-constants-of-solids (cit. on p. 121).

[174] M. K. McBride, A. M. Martinez, L. Cox, M. Alim, K. Childress, M. Beiswinger, M. Podgorski, B. T. Worrell, J. Killgore, and C. N. Bowman. "A readily programmable, fully reversible shape-switching material". In: *Science Advances* 4.8 (2018), eaat4634. DOI: 10.1126/sciadv.aat4634. URL: https://www.science.org/doi/abs/10.1126/sciadv.aat4634 (cit. on p. 123).

[175] X. Huang, L. Qin, J. Wang, X. Zhang, B. Peng, and Y. Yu. "Multiple Shape Manipulation of Liquid Crystal Polymers Containing Diels-Alder Network". In: *Advanced Functional Materials* 32.51 (2022), p. 2208312. DOI: https://doi.org/10.1002/adfm.202208312. URL: https://onlinelibrary.wiley.com/doi/abs/10.1002/adfm.202208312 (cit. on p. 123).

[176] F. Pujol-Vila, P. Güell-Grau, J. Nogués, M. Alvarez, and B. Sepúlveda. "Soft Optomechanical Systems for Sensing, Modulation, and Actuation". In: *Advanced Functional Materials* 33.14 (2023), p. 2213109. DOI: https://doi.org/10.1002/adfm.202213109. URL: https://onlinelibrary.wiley.com/doi/abs/10.1002/adfm.202213109 (cit. on p. 123).

[177] R. Berkovits and S. Feng. "Correlations in coherent multiple scattering". In: *Physics Reports* 238.3 (1994), pp. 135–172. DOI: https://doi.org/10.1016/0370-1573(94)90079-5. URL: https://www.sciencedirect.com/science/article/pii/0370157394900795 (cit. on p. 125).

Nederlandse Samenvatting

In dit proefschrift bestuderen wij verschillende golffrontmodulaties van licht voor diverse wetenschappelijke en toegepaste doeleinden en scenario's. Samengevat kan de scriptie worden onderverdeeld in drie projecten, waarbij wij golffrontmodulatie toepassen om 1) de eigenschappen van de nieuwe "*mutual scattering*" grondig te bestuderen, 2) de prestaties van de golffrontvormingstechniek (WFS, in het Engels afgekort) te testen, en 3) speckle-correlaties te bestuderen voor toepassingen in zichtbare lichtcommunicatie (VLC, in het Engels afgekort). Het moduleren van het golffront van het inkomende licht in een complex medium is een krachtig instrument om lichtvoortplanting binnen het medium beter te begrijpen en controleren. Deze techniek is van toepassing op sterk verstrooiende materialen zoals papier, wolken of biologisch weefsel, en gestructureerde materialen zoals fotonische kristallen of geïntegreerde schakelingen en zelfs voor kwantum toepassingen. Verschillende technieken en actieve apparaten kunnen worden gebruikt om het golffront te moduleren, zoals ruimtelijke lichtmodulatoren (SLM, in het Engels afgekort), digitale microspiegelapparaten (DMD, in het Engels afgekort), metaoppervlakte, vervormbare spiegels, elektro-optische modulatoren en nog veel meer.

Het hoofdproject van dit proefschrift is gewijd aan *mutual scattering*, dat wordt behandeld in Hoofdstukken 2 tot 5. Dit proefschrift presenteert de eerste experimentele waarneming van *mutual scattering* en de eerste toepassing ervan in karakterisering van lichtverstrooiing in complexe media. *Mutual scattering* treedt op wanneer twee of meer binnenkomende lichtstralen elkaar kruisen in een eindig object, en het is de kruisinterferentie tussen de coherente invallende golf van de ene lichtstraal en de verstrooide golf die wordt gegenereerd door de andere lichtstraal. In onze experimenten moduleren wij de binnenkomende lichtstralen waarbij wij onderlinge hoek en fase te veranderen, waardoor wij de verstrooiingseigenschappen van het object kunnen controleren en karakteriseren.

Naast het meten van *mutual scattering* passen wij voor het eerst WFS toe op specimen of apparaten met vrije vormen (Hoofdstuk 6). In dit project treden wij buiten de standaardbenadering van lichtverstrooiing in complexe media, waarbij de geometrie van het te bestuderen object de vorm van vlakke plaat heeft. Hoewel wordt verondersteld dat WFS van toepassing is op elk verstrooiend medium, moeten andere geometrieën verrassend genoeg nog worden verkend. In dit project laten wij zien dat WFS even effectief is in een vrije-vorm object als in een plaatgeometrie, waarmee onze hypothese wordt bevestigd. Vrije-vorm objecten zijn

van groot praktiek belang door hum brede cerspreiding in industrie toepassingen.

Ten slotte onderzoeken wij golffrontmodulatie in een VLC-systeem (Hoofdstuk 7), waarbij wij de eigenschappen van complexe verstrooiende media benutten voor versleutelingsdoeleinden. Hiervoor gebruiken wij een verstrooilaag als fysieke niet-kopieerbare functie (PUF, in het Engels afgekort), die dient als een extra beveiligingslaag in een communicatie systeem met en zender en een ontvanger. Wij gaan verder dan eerder bestudeerde situaties door *twee* verstrooilaagjes op te nemen, één bij de zender en de andere bij de ontvanger. Deze aanpak heeft tot doel een aanval van een persoon-in-het-midden te voorkomen, waarbij de aanvaller de communicatie tussen de zender en de ontvanger onderschept. De verstrooilaag bij de verzender voorkomt dat de aanvaller de boodschap precies hun kopiëren, en de verstrooilaag bij de ontvanger voorkomt dat de aanvaller de boodschap begrijpt en voorkomt *jamming*-aanvallen. Bovendien geeft de complexiteit van het systeem een enorme redundantie en tegelijk veiligheid, doordat duizenden verschillende golffronten beschikbaar zijn om dezelfde boodschap te verzenden. De zender kan zonder extra moeite afwisselen tussen de vele beschikbare golffronten, waardoor het buitengewoon moeilijk wordt voor een aanvaller om de boodschap te ontcijferen.

Acknowledgements

A Ph.D. is not a process in isolation and by no means should ever be. Throughout my research career, I have met amazing people from all over the world and it is, I dare to say, the most enriching part of science. I am proud of having as an acquaintance many smart and wise people and even prouder to call many of them my friends. In this last section, I want to thank (hopefully) most of the people who helped me on the way.

First of all, I want to thank my supervisor **Willem Vos**. **Willem**, I deeply appreciate your supervision throughout my Ph.D. You have strong ethics and are an excellent scientist. You know your way in the scientific process and have an amazing ability to give away reprints at conferences. I learned many, many things from you and I strongly believe they will help me to become a better scientist myself. I want to particularly thank you for your support and understanding during the pandemic and during my personal struggles. You gave me flexibility which some may consider luxurious, but it was invaluable to continuing my research. You showed me that science and supervising are, after all, human interactions and that we need to treat each other like humans. All things considered, I am happy to be part of COPS history.

I would like to continue by thanking my co-supervisor **Ad Lagendijk**. **Ad**, your vast knowledge and your passion are both inspiring and enlightening. I was lucky to work on the experiments directly related to your theory, which attracted a lot of your attention. It has been amazing to work with you and to learn directly from you. Thank you for your support, your explanations, your input, and your critics.

I would like to thank the committee members, **Mathias Fink**, **Allard Mosk**, **Ferry Zijp**, **Wilfred van der Wiel**, and **Ivo Vellekoop** for taking their valuable time to read my thesis, provide feedback, and participate in the defence.

My project was part of the NWO-TTW "Free-Form Scattering Optics (FFSO)" program. During the program, I had the opportunity to meet (both live and online) amazing people from other universities and companies. I would like to thank all members of the FFSO program, namely the group of **Wilbert IJzerman** from TU/e and the group of **Paul Urbach** and **Aurèle Adam** from TUD, and the industrial partners from ASML, Signify, Demcon, Lumileds, Schott, and TNO. I would like to give a special thanks to **Wilbert IJzerman**, **Aurèle Adam**, **Joris Vrehen**, and **Léon Woldering** for insightful discussions and feedback. It was a pleasure to meet my colleagues from other universities who

are going (or already went) through the same process as me, namely **Alex Heemels**, **Lotte Romijn**, **Thomas Kotte**, **Ví Kronberg**, **Robert van Gestel**, and **Maikel Bertens**.

I would like to thank my paranymphs **Ozan Akdemir** and **Timon Vreman**. **Ozan**, I deeply appreciate your help and support both in and outside of work. We had many experiences together and I thank you for all of them. Thank you for integrating me into the COPS group and welcoming me at your place so many times. I wish you the best and I am sure you will succeed in your new path, whichever you choose. And for the sake of *Tom*, we must keep in touch! **Timon**, thank you for all the insights about the Dutch culture, especially music, and thank you for practicing Dutch with me. We had a lot of fun at the coffee table, meetings, and conferences. I wish you the best in what is left of your Ph.D., you are smart and capable and I hope you are as confident as I am of your success.

I would like to thank the backbone of COPS, **Nicole Meinster-Engbers**, **Cock Harteveld**, **Melissa Goodwin**, and **Geert Kamphuis**. **Nicole**, thank you for suffering all the UT bureaucracy so we do not have to. It is always pleasant to talk to you. **Cock**, your presence in the lab showcases how crucial permanent staff is for science. Thanks for all the help with building setups and experiments. **Melissa**, your arrival at COPS was really a pivotal point for the group. You are smart, quick thinking, funny, and you know about chemistry; a combination that can be very dangerous! Thanks for all the help with the experiments. **Geert**, even in our short overlap I enjoyed our conversations in meetings and at the coffee table. I wish you the best at COPS!

I want to take this opportunity to thank **Willem** and **Cock** for their help during the coronavirus pandemic when I was just starting my experiments and the labs were suddenly not accessible. As a nugget of COPS history, the first set-up of mutual scattering started at Willem's attic and then moved to my apartment, where I was able to do experiments during the lockdown with a big thick black curtain splitting my living room.

I would like to thank all the current and past members of COPS. Special thanks to **Lars Corbijn van Willenswaard**, **Marek Kozoň**, **Manashee Adhikary**, **Duy Truong**, **Femi Ojambati**, **Niels Alferink**, **Bert Mulder**, **André de Mots**, **Andreas Schulz**, **Linda Bitenc**, and **Bill Barnes**. **Lars**, I appreciate all your help and input to my research. You always pay attention to others talks and presentations and you ask the correct questions. Thank you for joining the climbing group and I am impressed with all your progress. I wish you the best in finishing your thesis and in your future endeavors. **Marek**, thank you for your input and insights on my research, I learned something new at every meeting. Thank you for hanging out with me even if I do not drink, which I know is a disgrace. You are very smart and funny and I am sure we will cross paths again. And for *Ilde*'s sake, we must keep in touch! **Manashee**, it is always fun to hang out with you. You definitely left a mark at COPS and I have fond memories from when you were still at the UT. I am genuinely happy for all the big steps you are taking in your life and I am looking forward to meeting you again at conferences. **Duy**, I monopolized your help for a long time during your postdoc at COPS. Thanks a lot for all the discussions and meetings we had where we were

figuring out together what we were doing. I wish you the best with your new job and I hope we keep in touch. **Femi**, I am glad I met you when you came back to the UT. Every discussion we had in conferences or meetings was enriching and I appreciate that. **Niels**, I wish you the best with your master project and what comes afterward. Thank you for working with me at the Nanophotonics experiments and I am glad you came back to COPS. I know you are going through tough times, it is now when we need to cherish the good moments. **Bert**, thank you for doing your bachelor's project with me and still coming back to COPS. You are very smart and good at programming. Thank you for working with me and for your input during meetings. I wish you the best in the next steps! **André**, thank you for doing your bachelor's thesis with me. I am sorry that the original plan for your project failed, but I really appreciate your work on it because it was the foundation for the new directions afterward. I wish you the best in your career.

I am senior enough to say that *back in my days*, Adaptive Quantum Optics (AQO) was part of COPS. Undoubtedly, the bond between the students of these groups remains. Therefore, I would like to thank **Chris Toebes**, **Charlie Mattschas**, **Malaquias Correa Anguita**, **Innes Maxwell**, **Stefan van den Hoven**, **Daan de Ruiter**, **Violetta Sharoglazova**, **Marius Puplauskis**, **Frank Somhorst**, and **Sara Marzban**. **Chris**, thank you for all the extensive and graphical descriptions of the Achterhoek culture. You are a brilliant person and the most senior member around, so you know about any experiment happening around here. Thank you for fruitful discussions about research even if we are not from the same group. And of course, thank you for making any single coffee break and lunch a remarkable experience with funny and, let's say *interesting* topics. We must keep in touch for *Lutin*! **Charlie**, thank you for joining the climbing group, but at the same time I am sorry for the constant injuries that it involves. I had a lot of fun climbing, playing DnD, and just hanging out. Thank you for teaching me about "real" bread, which I hope works. We must keep in touch! **Malaquias**, what a surprise to have a second "weón" around here. Thank you for joining the climbing group and I am sorry that it led to an addiction. It was very fun to have inside Chilean jokes around here and I enjoyed all the lunches and coffee breaks. Keep it up! 11. **Innes**, thank you for joining climbing and DnD. Thank you for helping me improve my English and for your feedback on Nanophotonics. You are super funny, eloquent, and smart. I am happy to meet you and we must keep in touch! **Daan**, thank you for joining the climbing group, definitely not as a newbie. I enjoyed a lot climbing with you, and discussing betas and techniques. Thank you for joining the outdoor trips and I hope we continue doing it. **Stefan**, thank you for being part of the climbing group and for cycling back to Hengelo with me afterward. I enjoyed talking with you, either biking, climbing, or at the coffee table. I hope you continue climbing because you are very good at it. I would like to also thank **Violetta** and **Marius**, my recent office mates, **Frank**, who is in contact with the Messiah himself, and **Sara** ~~with her endless search for a place to live in Twente~~ congrats with your new place!.

There are many people I would like to thank outside the inner circles of COPS, AQO, and the UT. I would like to thank **Matthijs Velsink**, **Shweta Pal**,

Mario Vretenar, **Reinier van der Meer**, **Sevgi Ericek**, **Jacqueline Labra Muñoz**, and **Matías Lasern** for making my life at the UT, and the Netherlands in general, fun and enjoyable.

I would like to thank current and previous members of the OPTICA student chapter: **Kees Franken**, **Carlos Osornio**, **Anzal Memon**, and **Bjorn Jongebloed**. The chapter was an amazing experience, and one of the main reasons was that I was able to meet you all. I wish you the best for the future, and let's keep the chapter alive!

I would like to thank the Applied Nanophotonics (ANP) cluster in the MESA+ institute, formed by the groups of **Klaus Boller**, **David Marpaung**, **Pepijn Pinkse**, **Herman Offerhaus**, **Sonia García Blanco**, **Ivo Vellekoop**, **Christian Blum**, **Jaap van der Vegt**, and **Matthias Schlottbom**. Including the groups of **Rebecca Saive**, **Jan Klärs**, and **Jelmer Renema**. I believe such an organization as ANP is crucial for collaboration and connection within the same university and I enjoyed the regular meetings and retreats.

I would like to thank my former supervisors, **Herre van der Zant**, **Diana Dulić**, and **Ernest Michael** for leading me in the path of research.

I could not have started my Ph.D. at the University of Twente without the support of *The Gang*: **Maria El Abbasi**, **Davide Stefano**, **Luca Ornago**, and **Chunwei Hsu**. **Maria**, you are one of the most talented and motivated people I know. I am happy that our friendship persisted, even after so many moves. I thank you for all the times you received me at your place, which is not few. I wish you the best in your current position and I hope we keep in touch! **Davide**, you may not remember but you were one of my first contacts with Europe. I appreciate the time we spent in Delft, and I blame you for two of my big addictions: climbing and Switch. **Luca**, you are so kind and friendly, and our sense of humor matches, which is not something easy to find! Thank you for the good times in the past and thank you in advance for the good times to come. **Chunwei**, you are a very smart and wise person. I learned a lot working with you and enjoyed all the SSBU sessions we had. I wish you the best in your career and I hope we continue meeting in the future.

I would like to thank my family for their support during these years. I would like to thank my sister **Mariangela Rates**, my brother **Miguel Rates**, and my sister **Isabella Fucaraccio**. Thank you for all the calls, games, inside jokes, and the mutual support we received during difficult times. I wish our relationship stays well with the passing of the years. I could fill pages with all the hilarious and lovely anecdotes we have. I would also like to thank my father **Alfredo Rates**, my aunt **Marcela Soriano**, and my brother **Diego Rates** for all their help and support, especially at the beginning of my journey. I would like to thank **Alejandra Miranda** and **Carolina Cuevas** for their support, and **Paula García** for designing the cover of this thesis. I would also like to thank my mother **Pamela Soriano**. You taught me much, and I always admired your energy and strength. I dedicate this thesis to your memory.

I would like to thank my friends from Chile **Felipe Manen**, **Juan Pablo Cuevas**, and **Camila Briones**. It is amazing that our bond survives to this day, and I hope it survives even longer. I wish each of you the best and I hope we

see each other soon. I would also like to thank **Mariana Torres**, whose support was essential to overcoming every struggle these last years.

Last but certainly not least, I would like to thank **Catalina García**. You helped me in any possible way and the words to make it justice are impossible to fit in this book. Thank you for every day we have been together, but above all, thank you for accepting me as I am.

I would like to finish by thanking you, the reader, for reading my whole thesis up to this point (because you did... right?).